NTNU
Norwegian University of Science and Technology
Faculty of Natural Sciences
Department of Physics

Eskil Johan Nilsen Einmo

Characterization of Laser-Induced Surface and Subsurface Modifications in ZnS

Master's thesis in Physics
Supervisor: Irina T. Sorokina
June 2022

NTNU
Norwegian University of
Science and Technology

Eskil Johan Nilsen Einmo

Characterization of Laser-Induced Surface and Subsurface Modifications in ZnS

NTNU

Norwegian University of
Science and Technology

Abstract

This thesis reports for the first time subsurface structures in ZnS induced by a 2.1 µm ultrashort pulsed laser. Although earlier studies have led to the development of in-bulk defects and waveguides in ZnS crystals using shorter irradiation wavelengths, processing in this mid infrared (MIR) wavelength region is yet to be reported in the literature. The structures were inscribed by varying parameters, such as average power, writing speed, and depth. Highly symmetric waveguides with an circular core and cladding were realized and characterized. A wide range of characterization methods, such as optical microscopy, infrared transmission microscopy, micro-Raman spectroscopy, scanning electron microscopy, and laser coupling experiments, are used for studying these laser-induced structures. Waveguides with a 30 µm core diameter exhibit single-mode confinement and propagation losses ranging from 0.32 to 1.18 dB/cm. This work also investigates for the first time an active gain medium, which encompasses waveguides integrated with anti-reflection coatings, with all structures being developed with femtosecond laser processing.

Sammendrag

Denne avhandlingen rapporterer induserte strukturer under overflaten av ZnS, laget med ultrakorte laserpulser av bølgelengde 2.1 µm. Slike strukturer laget med denne bølgelengden utforskes for første gang i løpet av dette arbeidet. Publisert forskning i dette feltet har frem til nå bare omhandlet liknende strukturer laget med kortere bølgelengder. Defekter er laget med varierende parametre som effekt, skannehastighet og dybde. Strukturer med høy grad av symmetri, hvor både kjernen og kledningen er nær sirkulær demonstreres og karakteriseres. Bølgeledere med kjerne av diameter 30 µm viser optisk singel modus operasjon med forplantningstap på omtrent 0.32-1.18 dB/cm.

Et aktivt laserforsterkningsmedium med bølgeledere og antireflekterende strukturer på tverrsnittet er for første gang demonstrert, hvor alt er prosessert med fs laserpulser.

Preface

This Master's Thesis in Physics is delivered to the Department of Physics as a completion of a Master's degree in Natural Science with Teacher Education at the Norwegian University of Science and Technology (NTNU). The Scientific method of acquiring knowledge and lab experience gained during this thesis will provide excellent qualities in educational work. The thesis is a continuation of a specialization project carried out in the fall of 2021[1], and is part of a larger study by the Laser Physics Group at NTNU. The experimental work that is presented is performed in laboratories at the Department of Physics as well as at the NanoLab NTNU.

Some of the results obtained during this work were presented in the following publications:

- E. Sorokin, A. A. Bushunov, N. Tolstik, A. A. Teslenko, E. Einmo, M. K. Tarabrin, V. A. Lazarev, and I. T. Sorokina, "All-Laser-microprocessed waveguide Cr:ZnS Laser." *Opt. Mater. Express* 12, 414-420 (2022).

- A. A. Bushunov, A. A. Teslenko, V. A. Lazarev, E. Sorokin, N. Tolstik, A. A. Teslenko, E. Einmo, I. T. Sorokina, M. K. Tarabrin, "Cr^{2+}:ZnS laser crystal antireflection treatment by ultrashort laser pulses" in Proceedings of Conference on Lasers and Electrooptics (CLEO'2022), paper JW3B.60, 15-20 May 2022, San Jose, USA.

Acknowledgements

Contents

List of Figures

List of Abbreviations

ARC	Anti-Reflection Coating
ARM	Anti-Reflection Microstructure
Cr:ZnS	Chromium doped Zinc Sulfide
DBE	Distance Between Elements
HAZ	Heat Affected Zones
IR	Infrared
LASER	Light Amplification by Stimulated Emission of Radiation
LIPSS	Laser Induced Periodic Surface Structure
MIR	Mid Infrared
NA	Numerical Aperture
NIR	Near Infrared
RIE	Reactive Ion Etching
SEM	Scanning Electron Microscopy
Si	Silicon
SPPC	Self-pumped phase conjugation
ZnS	Zinc Sulfide
3D	Three-dimensional
AI	Avalanche Ionization
MPA	Multi-Photon Absorption
TI	Tunnel Ionization
2PA	Two-Photon Absorption
3PA	Three-Photon Absorption

1   Introduction

1.1   Motivation

Since the technological milestone of realizing the first laser in ruby in 1960[2], lasers have become widely used in applications both in science and industry. Lasers have already been used for material processing since the 1980s, with the invention of chirped pulse amplification in 1985[3]. Also, the realization of the chirped regenerative amplifier in a Ti:Sapphire laser system in 1993[4] has resulted in huge interest in this field in the last decades for structuring different materials. This made it possible to process materials with pulses short enough to neglect heat affected zones(HAZ) in the surrounding media. The laser has since shown itself for being a reliable tool for creating surface and subsurface structures of sub-wavelength resolution. By further advancing this field of study, it is possible to create 3D structures in the bulk of materials that pave the way for in-chip microstructures, integrated optics and high-efficiency photonic devices, all with several functions within one substrate. Also surface processing allows fast and low-loss production of photovoltaic cells for the solar cell industry. By implementing laser processing in this field, light absorption by solar cells can be significantly increased, thereby providing major environmental advantages in the everlasting battle of cost versus efficiency[5,6].

The first subsurface waveguide was achieved in 1996[7], and has since then similar structures have been realized in several types of glasses and crystals, including semiconductors such as ZnS[8]. By using pulsed laser processing methods to write integrated structures, such as waveguides in laser gain media, it is possible to significantly increase laser performance and thereby emulate similar developments in fiber lasers.

The mid infrared(MIR) wavelength region in particularly interesting for laser technology and development. Many organic as well as inorganic molecules have their absorption lines in this wavelength range, including biological tissue, which makes MIR wavelengths attractive for spectroscopy and material processing applications. Since the atmospheric transmission window lies in this spectral region, applications related to scientific, medical, and military applications, as well as environmental and industrial diagnostics, have been partially responsible for the increased interest in research in compact ultrafast high-power MIR laser technology.

High precision material processing is in high demand due to its ability to create highly reproducible nanometer-scale structures with low material loss both on the surface and inside the medium. This thesis presents the novelty of the characterization of laser-induced defects in ZnS for determining optimal parameters for laser writing of waveguides at wavelengths above 2 µm. The possibility of introducing laser-induced anti-reflection coatings on the facets of buried depressed-cladding waveguides to miti-

gate cavity losses due to Fresnel reflections is also investigated, specifically in Cr^{2+}:ZnS.

1.2 Aim of this work

Surface and subsurface modifications induced in semiconductors by ultrashort laser radiation is a novel technology that can provide numerous benefits to several fields of science. These include applications ranging from high performance photovoltaics in environmental physics to compact sensors in space technology. To advance this field of study, a more comprehensive understanding of the processing parameters and underlying mechanisms is needed.

The primary goal of this thesis is to investigate laser-induced surface and subsurface defects in ZnS. The first aim is to study buried modifications for finding optimal parameters of writing waveguides in the same material. The waveguide structure desired is a buried depressed cladding waveguide that consists of a cylinder defined by defect lines inscribed in the crystal. The formation of such defects in ZnS using laser writing wavelengths above 2 µm, is yet to be reported. The ultrafast laser used to induce the modifications investigated in this thesis is a novel laser system developed by the NTNU Laser Physics Group.

Anti-reflection coatings normally consist of a single or multiple layers of dielectric thin films to mitigate surface Fresnel reflections. These coatings are not optimal for high power lasers and, particularly, for ultrashort pulse lasers, where spurious reflections can interfere with the pulse. Anti-reflection coatings made by an alternative femtosecond laser writing technology is another interesting application and will also be investigated during this thesis work.

Reaching both aims - studying surface and sub-surface modifications - will help to gain the knowledge needed for further performance optimization of compact waveguide lasers, in which both the waveguide and the anti-reflection coating are created by an ultrashort pulse laser technology.

1.2.1 Objectives

To investigate and characterize these structures, several methods have to be implemented. The objectives in this thesis regarding characterization are as following:

- Obtaining relevant knowledge about buried modifications in ZnS and other materials as well as surface modifications by literature research.

- Acquire knowledge in techniques regarding investigation of such samples, and learn my way around the lab. These techniques include:

  - Optical microscopy for detecting induced modifications.

  - Infrared transmission microscopy to image and investigate certain characteristics of buried modifications as well as surface structures.

- – Other characterizing methods such as Scanning electron microscopy(SEM) and Micro-Raman spectroscopy.

- Laser output power measurements to estimate laser threshold and slope efficiency of cladding buried waveguides with anti-reflection microstructures in Cr:ZnS.

2   Theoretical overview

2.1   Crystalline Laser Waveguides

A laser is a device that emits light due to stimulated emission of radiation. This usually comprises of an optical resonator (cavity), that contains a gain medium and a pumping scheme. The gain medium is placed inside the cavity, in which light can circulate due to, for example, reflections on mirrors positioned at each end. For the medium to generate emission, the gain must be greater than the losses in the cavity and, thus, it requires an energy source. This is achieved by a process called pumping. Although there exists several different pumping schemes, optical pumping is often preferred, where light is pumped into the medium to create population inversion, which results in emission of light of wavelengths dependent on the gain medium. The output beam usually has very low divergence and a very high level of spatial coherence. A system like this is called a solid-state laser, and it often uses crystals, e.g. zinc sulfide (ZnS), as a gain medium. These crystals are usually doped with a rare-earth element, like neodymium, or transition metal ions, e.g. chromium. As shown in a simple setup of a solid-state laser in Figure 2.1, a dichroic mirror is often used to separate the outgoing light. A dichroic mirror transmits specific wavelengths and reflects other, and its selection depends on the specific requirements of the particular laser system setup.
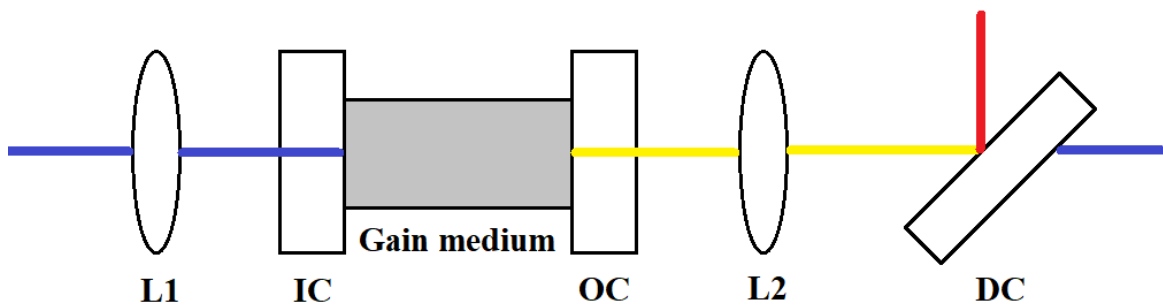
Figure 2.1: Simple setup of a cavity configuration where the optical pump is coming in from the left. Consisting of pump lens (L1), input and output couplers (IC, OC), output collimating lens (L2) and dichroic mirror (DC) separating the residue pump from the laser output.

2.1.1   Laser beam properties

The most important properties of the laser beam are monochromaticity, coherence, directionality and brightness. These four concepts describes how a laser beam behaves in free space.

Monochromaticity

The specific property of electromagnetic waves to consist of a single frequency is called monochromaticity. Since this effectively means that the light must have zero optical linewidth, this condition can be never achieved completely, although the laser beams come close to fulfilling it. This happens because the light is propagating into the resonator formed by the two mirrors (as seen in Figure 2.1), where only one frequency can be amplified.

Coherence

Coherence can be separated into two concepts, spatial and temporal. Spatial coherence refers to the strong correlation between the electric fields at different locations of the laser beam as it travels through free space. A laser beam can achieve a very high degree of spatial coherence because the light emission happens due to (stimulated) intracavity radiation instead of occurring spontaneously. In practice, a beam will only be spatial coherent in a limited area and, therefore, it is often referred to as partial spatial coherent. Temporal coherence refers to the strong correlation between the electric fields in a location at different times. If the electric field propagates in a very predictable fashion and exhibits continuity it is considered high temporal coherence. If the electric field has random phase jumps it is said to have partial temporal coherence.

Directionality

A laser beam is considered to be highly directional, as it exhibits a very small divergence due to the resonator cavity, where only waves traveling along its optical axis can be sustained. For a beam of finite aperture with perfect spatial coherence, there will always be a divergence of some degrees due to diffraction. For a finite beam diameter D, it has a finite divergence θ_d, and we obtain

$$\theta_d = \beta\lambda/D, \tag{1}$$

where λ is the wavelength of the beam. β is a numerical coefficient dependent on the light amplitude distribution. A beam like this is described as diffraction limited. For a partial spatial coherent beam the divergence is given by

$$\theta = \beta\lambda/(S_c)^{1/2}, \tag{2}$$

where S_c is the defined coherence area.

Brightness

The most important parameter of a laser beam, namely the brightness, is defined as the emitted power per unit surface area per unit solid angle from a given source of electromagnetic waves. For a beam area and emission solid angle equal to $\pi D^2/4$ and $\pi\theta^2$, respectively, we have beam brightness[9]

$$B = 4P/(\pi D\theta)^2. \tag{3}$$

If the beam is diffraction limited, we have $\theta = \theta_d$. From eq. (1) and (3) we then obtain the maximum brightness

$$B = \left(\frac{2}{\pi\beta\lambda}\right)^2 P. \tag{4}$$

2.1.2   Gain media

Cr:ZnS

ZnS doped with Cr^{2+}-ions is a relatively new type of gain medium in the world of lasers, and was first introduced in 1996 by DeLoach et al. [10]. Cr^{2+}-doped II-IV compound materials like ZnS is particularly interesting as gain medium due to their ability to offer high-power radiation in the above 2 μm wavelength region, which is desirable for many material processing and gas sensing applications. It also holds the property of being widely tunable in the same wavelength range. In the last decade, Cr:ZnS has, amongst other materials, e.g. Cr:ZnSe experienced a lot of attention due to the spectral region in which they emit radiation. The mid-infrared(MIR) spectral region has been relatively unexplored in laser technology for a long time and the important group of chromium-doped chalcogenides seems promising to fill this gap. The gap of broadly tunable ultrafast high-power laser technologies between 2-2.5 μm has neither been covered by technologies such as hetero-junction semiconductor lasers nor by quantum cascade lasers (QCL)[11]. The emission spectrum for Cr:ZnS is shown in Figure 2.2, where the emission cross-section σ is also seen. Emission cross-section is the probability of an ion to exist in a given cross-sectional area, which is excited and will emit a photon.

These materials also have the property of room temperature operation, which, combined with the advantage of operating in the above 1.4 μm wavelength eye-safe region, significantly reduces the total cost of ownership.

Due to the availability of well-established appropriate pump sources, chromium-doped chalcogenides can produce pulses down in the femtosecond regime. Specifically, Er:fiber
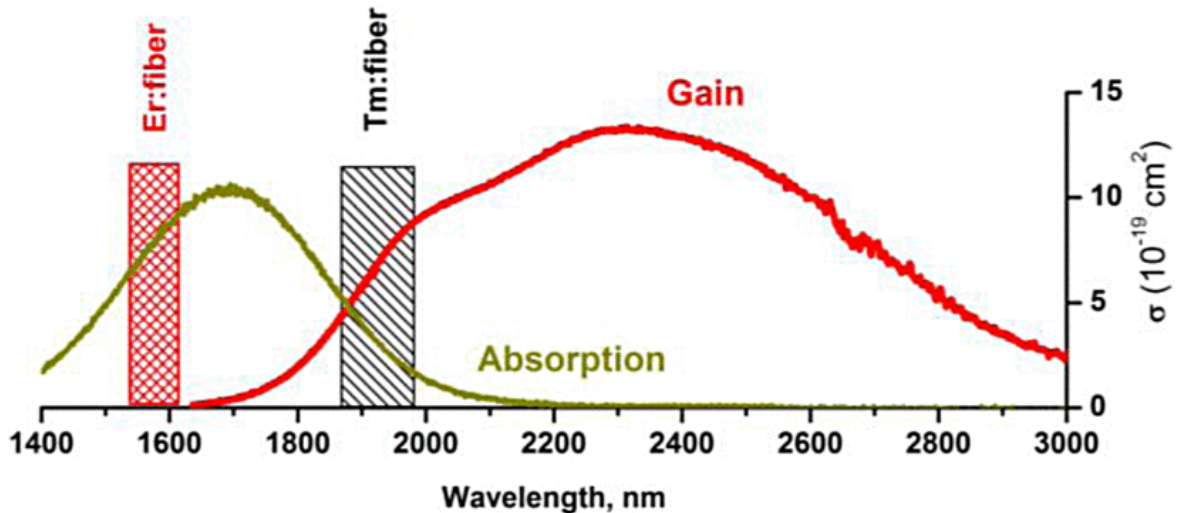
Figure 2.2: Absorption and emission spectrum of Cr:ZnS. Emission of Er:fiber and Tm:fiber is also shown[12].

and Tm:fiber have played a significant role in this last decade's femtosecond laser development. Beam quality and power stability are the key factors in achieving femtosecond pulses, which these fiber lasers have. Er:fiber emission matches the absorption spectrum of Cr:ZnS as shown in Figure 2.2 and is therefore usually used to pump solid-state lasers based on Cr:ZnS as a gain medium.

A principal motivation for the research regarding Cr^{2+}-based femtosecond laser technology has been its resemblance of spectroscopy, material and laser properties to the Ti:sapphire laser, which is a well established femtosecond technology. The Ti:sapphire laser is also a widely tunable, ultrashort pulse high power laser with good beam quality, but it operates in the visible to near-infrared(NIR) region (i.i. 650 nm - 1100 nm)[13]. This is one of the reasons why Cr:ZnS is called the Ti:sapphire of the MIR spectral range between 2.0 and 2.5 +micro m.

2-2.5 µm gap

One of the reasons why the gap between 2-2.5 µm is of interest is due to the overlapping with the atmospheric transmission window, as shown in Figure 2.3. In this window, and up to 4 µm, we also find many organic and inorganic molecular absorption lines (see Figure 2.4) such that technologies like e.g. remote sensing, communications and laser surgery are some of the applications driving the research of these tunable high power sources[14]. A significant advantage for the Cr^{2+}-lasers is their ability to ensure narrow-linewidth tuning and spectral coverage of a wide wavelength range that contains many absorption lines in a single shot or by rapid tuning. This property makes it possible to detect multiple pollutants such as CO and CO_2 as well as other petroleum-related gases in this 2-4 µm wavelength region.
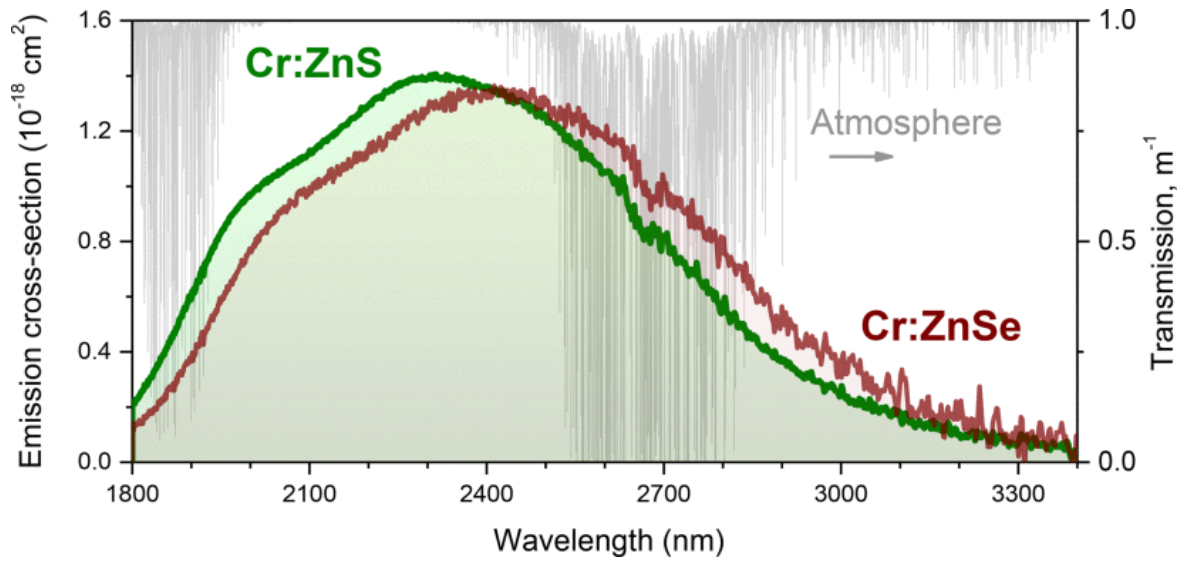
Figure 2.3: Emission cross-section spectra of Cr:ZnS and Cr:ZnSe, as well as atmospheric transmission spectrum (grey)[15].
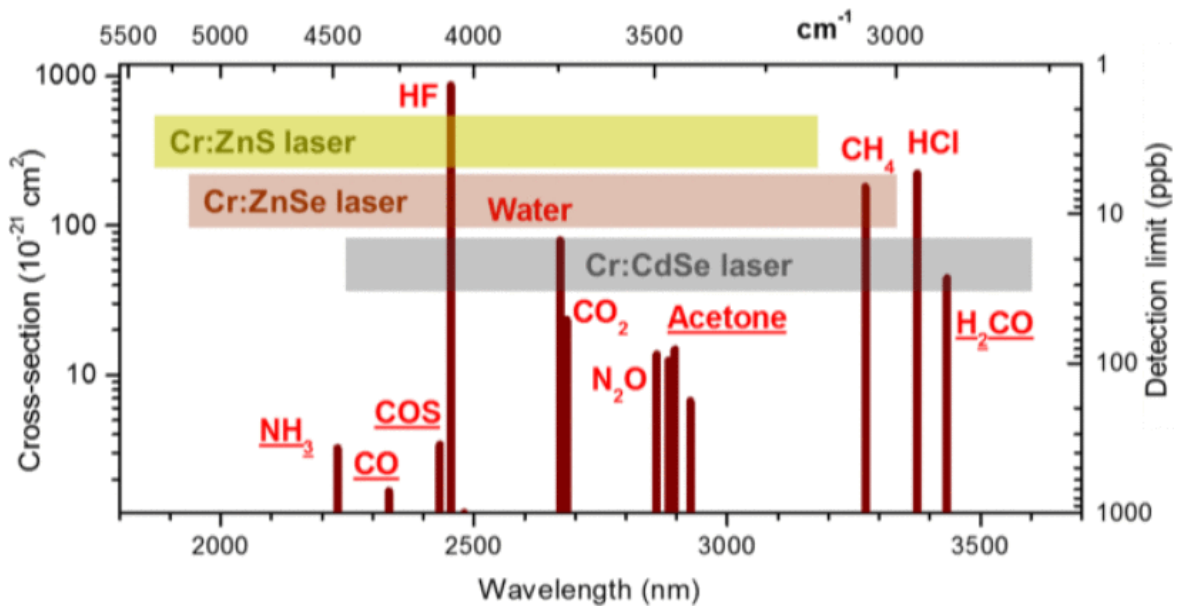
Figure 2.4: Spectral coverage and tunability of the most representative Cr^{2+}-lasers and spectral positions of important gas absorption lines[15].

Currently, laser systems that are used for gas detection are mainly based on single gas detection devices or nonlinear optical conversion techniques. The latter includes optical parametric oscillators (OPO), which has wavelengths that can be varied in wide ranges and therefore can be used for multigas analysis, but is a rather complex and costly system. Compered to the OPO technology, the femtosecond Cr^{2+}-lasers

are significantly less complex and have the robustness of compact fiber laser pumped solid-state lasers[15].

Slope efficiency

For an optically pumped laser, slope efficiency is a rather important property. It is defined by the slope curve obtained by plotting input pump power versus the output power of the laser gain media. This slope is often linear. For pump power and pump power threshold P_p and P_{th}, respectively, we can calculate the output power as[16]

$$P_{out} = \eta_{sl}(P_p - P_{th}), \tag{5}$$

where η_{sl} is the slope efficiency. It is important to note that the pump power in eq. (5) can refer to either the incident pump or the pump absorption.

Gain vs. loss

The condition where the gain equals the losses in a resonator is called a threshold. When the incident power from the pump exceeds this level, the laser emission starts. Propagation losses in the laser cavity are expected to limit the laser efficiency, and, therefore, loss minimization is crucial for laser performance. Losses can also be induced by thermal lensing or Fresnel reflections (see section 2.1.3) amongst other chemical and mechanical properties of the material[17].

2.1.3 Waveguides

Cr^{2+}-laser technology has demonstrated potential for generating high powers and ensuring wide tunability and good chemical and mechanical stability. Cr:ZnS lasers, in particular, have been established as a promising alternative among other broadband solid-state lasers. The only issue for power scaling this material has been a somewhat high thermo-optic coefficient (thermal lensing parameter) $(\delta n/\delta T)$[17].

Thermal lensing

In high power lasers, inhomogeneous heating of the gain material often occurs, causing thermal lensing. Thermal lensing is a phenomenon in which the wavefront curvature is modified, typically by a transverse refractive index gradient. In solid-state lasers, this can set a crucial limit to the performance. Cr:ZnS has a thermo-optic coefficient $(\delta n/\delta T) = 46 \cdot 10^{-6} \mathrm{K}^{-1}$. Compared to sapphire, with a thermo-optic coefficient of $12 \cdot 10^{-6} \mathrm{K}^{-1}$, this is relatively high. Since thermal lensing often happens due to this transverse gradient, a way to minimize it could be to make a geometry where heat flow perpendicular to the laser beam is avoided, e.g. a waveguide.
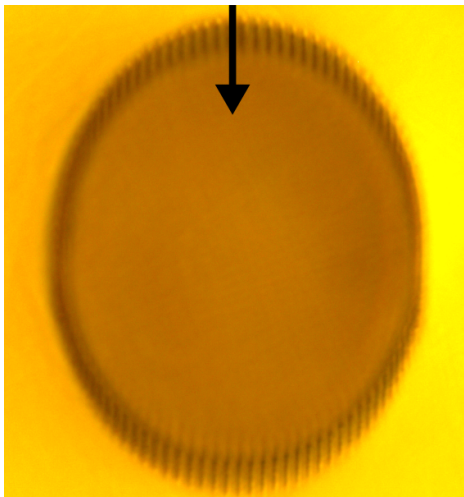
Figure 2.5: Microscopic picture of the cross-section of a laser-induced buried cladding waveguide in ZnS. The arrow indicates writing beam direction.[a]

Waveguide geometry

A waveguide is designed to guide the wave such that losses, due to for example a transverse refractive index gradient, are minimized. Waveguide geometries can be produced for guiding electromagnetic waves inside optical materials. A waveguide can often be considered as a fiber structure inside a material, including gain medium, consisting of a core with a surrounding cladding, as seen in Figure 2.5.

The core in such a waveguides considered in this thesis is an unmodified region where the refractive index initially is the same as rest of the material outside the structure. The cladding around is the modified part of the geometry where the refractive index is lower than inside the core. This makes the light inside the core reflect when it hits the cladding. The smallest angle where all the light is reflected inside the core, the critical angle, can be obtained by Snell's law

$$n_1 \sin \theta_1 = n_2 \sin \theta_2, \tag{6}$$

where θ_1 is the angle of incident and θ_2 is the angle of transmission. Here, n_1 and n_2 are the refractive indices of the core and the cladding, respectively. In eq. (6), it is also obvious that the larger the difference in the refractive indices, the smaller critical angle of total reflection. This also leads to the formation of waveguides with a larger numerical aperture (NA). The NA of a waveguide is its angular acceptance at the facet. It is defined as the product of the refractive index of the medium in which

---

[a]All subsequent figures of cross-sections has the same writing beam direction as fig. 2.5 unless indicated otherwise.

the beam propagates, e.g. air, and the maximum angle between the incident ray and the optical axis of the waveguide at the facet,

$$\text{NA} = n \sin \theta. \tag{7}$$

The numerical aperture can also be derived from the refractive indices of the core and cladding:

$$\text{NA} = \sqrt{n_{core}^2 - n_{clad}^2}. \tag{8}$$

Fresnel reflection

In the transition between free space and optical media, there will be reflections at the surface. They will occur as the beam enter the laser resonator and when the gain media starts to emit, and the generated light circulates inside the cavity. As seen in the example setup, Figure 2.1, the radiation will oscillate between the two mirrors (i.e., output and input coupler) until the gain has become greater then the losses of the cavity. This means that the beam inside the gain medium will impinge on the gain medium facets twice at each cavity round trip, where a portion of the circulating light will be reflected each time.

For the light to be completely transmitted, both media involved in the transition is required to have matching impedance. Since all optical materials essentially have a permeability $\mu = 1$, the impedance is only determined by their refractive index. Therefore the only case with no reflections is if the media have identical refractive indices[18]. These reflections can be described by using the Fresnel equations and are called Fresnel reflections. The reflected electric field for s-polarization is described as

$$E_r = E_i \frac{n_1 \cos \theta_1 - n_2 \cos \theta_2}{n_1 \cos \theta_1 + n_2 \cos \theta_2}, \tag{9}$$

and for p-polarization as

$$E_r = E_i \frac{n_2 \cos \theta_1 - n_1 \cos \theta_2}{n_2 \cos \theta_1 + n_1 \cos \theta_2}. \tag{10}$$

From these equations the reflection coefficient R_{FR} can be derived,

$$R_{FR} = \left| \frac{E_r}{E_i} \right|^2. \tag{11}$$

If we then assume that the angle of incidence is perpendicular to the surface of the entering medium, we can easily estimate the reflection by combining equation (11) and (9)/(10) and get

$$R_{FR} = \left| \frac{n_1 - n_2}{n_1 + n_2} \right|^2.$$

(12)
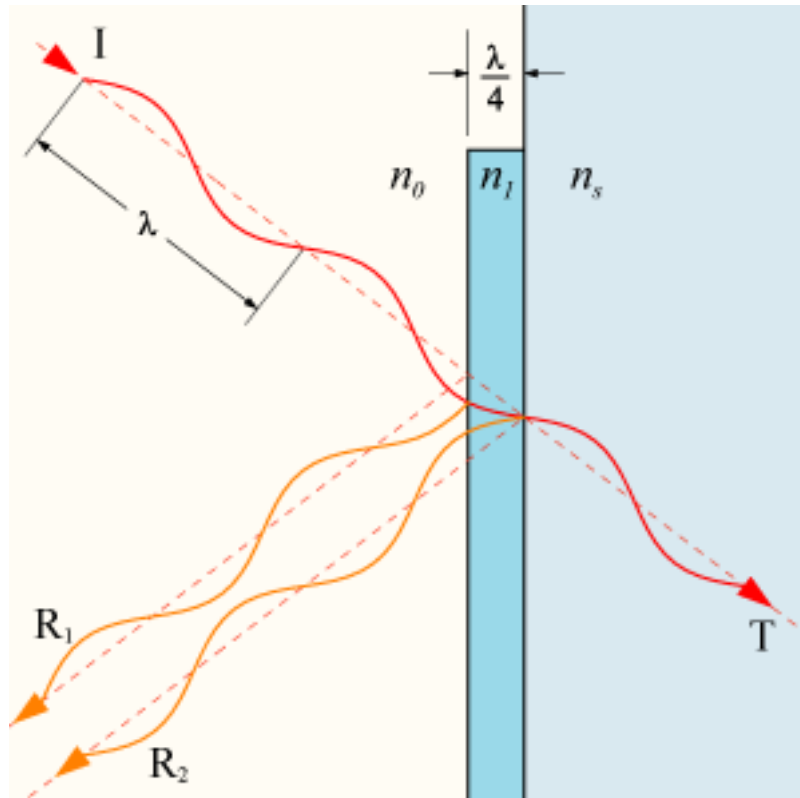
Figure 2.6: Single layer $\lambda/4$ anti-reflection coating. n_0, n_l and n_s is the refractive indices of air, layer and surface of material, respectively[19].

Waveguide loss

As mentioned in section 2.1.2, the propagation losses in a given cavity are important to mitigate. This also applies for waveguides in general and not only for laser cavities. The waveguide loss in decibels per unit length α can then be calculated to[20]

$$\alpha = \frac{1}{L} \cdot \log_{10} \left[\frac{1}{K} \cdot \frac{P_O}{P_I} \right],$$

(13)

where L is the length of the waveguide, P_I and P_O are the incident and output power, respectively. K is the transmission factor and is given by

$$K = T_{O1} \cdot T_{O2} \cdot T_{FR}, \tag{14}$$

where T_{O1} and T_{O2} are the transmission coefficients of the focusing objectives for the input and output of the waveguide, respectively. While T_{FR} are the Fresnel transmission coefficient and is given by

$$T_{FR} = (1 - R_{FR})^2. \tag{15}$$

R_{FR} can be calculated by using eq. 12.

Anti-reflection coating

Fresnel reflections can cause significant loss in optical power due to losses in transmission each time the emitted beam passes through one of the to facets of the gain medium, as well as the possibility of back reflection of the pump source. To mitigate this loss, anti-reflection coatings (ARC) might be used. These coatings usually comprises of a single or multiple layers to add optical interfaces such that the Fresnel reflections cancel out each other by destructive interference. An example, of an incident ray I, transmitted ray T, and reflected ray R, of a single layer coating can be seen in Figure 2.6, where the layer has a refractive index close to the geometric mean of the media indices. A single layer like this has a limited bandwidth and limited angular range. If a broader bandwidth or larger angular range is required, multiple layers need to be added, but the same principle applies. Although ARC works well for optical components like mirrors, lenses and objectives, is not always an optimal solution for high-power laser setups. Problems like film shedding or cracking due to thermal expansion or shrinkage of the material and a low damage threshold are some of the problems these coatings might introduce[21]. A solution to this can be to consider anti-reflection microstructures (ARM). Further details on this subject will be presented in section 2.2.1.

2.2 Material processing

Lasers have in general been developed for half a century and are becoming more and more user-friendly as well as cheaper every year. Lasers in material processing were already used in the 1980s but attracted significant interest in the 1990s after some very promising experiments using ultrafast lasers for material processing without heat affected zones(HAZ). After this, ultrafast lasers has established themselves as being very reliable tools, providing the possibility of fabricating sub-wavelength structures both on the surface and inside the bulk of different materials.

One type of microstructuring relies on the use of ultrafast lasers to make inscriptions or induce structural modifications inside a medium. The process is based on nonlinear absorption by using a high-power laser tightly focused to a point beneath the surface of some material. The irradiances generated in the focus are enough to cause nonlinear effects such as multi-photon absorption(MPA), tunneling ionization(TI) and avalanche ionization(AI). These processes allow energy tranfers to the material lattice[17,22,23,24,25]. By focusing the beam under the surface, the surface itself may stay unmodified. Doing this makes it possible to apply a locally refractive index change Δn in the laser-modified region (focal volume), and by placing the material on a moving stage it is possible to create three-dimensional(3D) structures.

This technique of using laser microstructuring for micro-machining transparent optical materials has proven to be one of the most efficient way to make structures of micronsize. A more detailed discussion of the technique will be presented in section 2.3.

As mentioned, laser processing is not an entirely new technology, but the enhancements in ultrafast lasers, especially the application of chirped pulse amplification by Strickland and Mourou [3], have made it extremely precise and the ability to reproduce periodic structures or ripples on the surface and inside materials, as well as precise cutting and drilling without any melt or cracks around the processed area. Due to the high demand for renewable energy sources and, in particular, silicon-based solar cell technology, considerable research efforts have been expended on increasing the efficiency of these photovoltaics. One of them being surface texturing of silicon wafers by laser ablation[6].

2.2.1 Surface processing of semiconductors

Surface structuring by ultrafast lasers has been extensively studied in the last decades. As mentioned earlier, this method has proven itself to be highly effective for many types of material processing due to minimal damage to the surrounding area. These structures can be as small as in nm scale.

An example of such small structures is shown in Figure 2.7. These structures exhibit a sub-wavelength periodicity compared to the writing laser of 1040 nm. Harzic et al. [26] showed in 2005 that these ripples, known as laser induced periodic surface structures
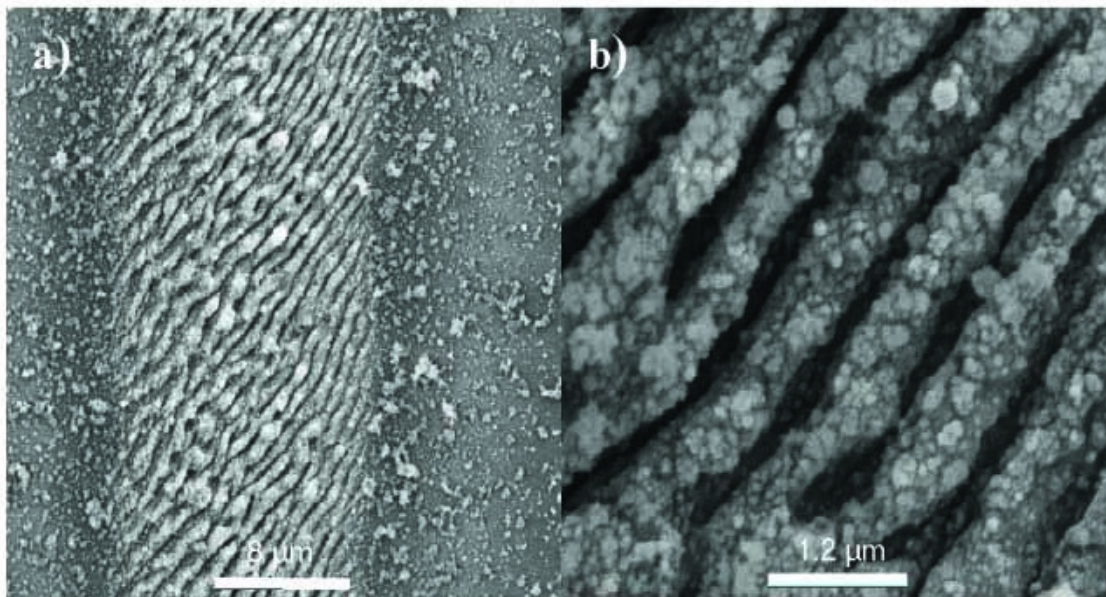
Figure 2.7: SEM images of periodic surface structures in the form of ripples on silicon made from laser irradiation[26].

(LIPSS), appear spontaneously on the surface of silicon when irradiated with ultrashort pulses at low fluence. They also state that these ripples result from the interference between incident, radiated or scattered light that causes periodic variations in the substrate heating and creates these LIPSS.

After further investigations into the phenomena, laser induced anti-reflection structures has been developed. By laser irradiation one can create regular arrays of periodic microstructures, which induces properties such as friction, optical absorption, reflection and hydrophobicity. The transmittance of these structures highly depend on morphological features, such as depth, period, filling factor and steepness[27]. Structures similar to these have been developed earlier by wet or dry etching, and direct imprinting. However, fabrication methods have disadvantages including complexity, cost, fabrication time and process waste, which can be offset by ultrafast laser structuring[28].

Anti-reflection microstructures

Microstructuring is self-evidently not only for modifying tracks inside the material but can be used to create structures at the surface. Due to vulnerability to surface contaminants and the low damage threshold of existing anti-reflection coatings(ARC), anti-reflection microstructures(ARM) may be the answer to eliminating surface reflection in high power laser systems. By using femtosecond laser writing it is possible to make periodic structures at the surface, with different cross-section profiles. These are

few micron structures with period dependency of what wavelengths is to be transmitted. Due to effective medium theory, the anti-reflection performance can be described by using a simple diffraction grating equation[29]

$$\lambda_{diff} = n \cdot p, \tag{16}$$

where n is the refractive index of the material, and p is the period of the microstructures. Hence the ARM will act as a gradient refractive index layer for wavelengths longer than what was calculated in equation (16), and thus diffraction and scattering will affect wavelength shorter than this. The overall transmittance will stay high, but since this structure will serve as a kind of diffraction grating more transmitted light will be of non-zero orders of diffraction or scattered.

Due to the issues related to the ARC, fabrication such microstructures instead of coatings should, in principle, ensure better performance for broad bandwidth high power applications. The transmittance in such a structure is dependent on the smoothness of the refractive index gradient, hence also on morphology parameters of the ARM. An important morphological feature is the aspect ratio, which can be described as structure depth to period relation. The aspect ratio, along with features like period dependency, filling factor and steepness are displayed in Figure 2.8 (adapted from Bushunov, Tarabrin, and Lazarev [27]). Here, it can be seen that the average transmittance increases with depth, filling factor and steepness, as well as reducing the size of the periods. It is also shown that if the aspect ratio is 1.5 or larger, it is possible to obtain transmittance above 98 %.

An issue with microstructuring the ARC is that it is difficult to achieve the parameters mentioned above since both the development of a precise model with required parameters and the fabrication with optimal similarity to the model can be very challenging. However, an adequate microstructuring technique should be able to make structures of aspect ratio larger than or equal to 1.5 as well as relatively high production rate.

Fabrication methods

There are several methods to fabricate these structures, e.g. direct imprinting, etching, lithography and 3D printing. Although these methods allow for the fabrication of high-quality anti-reflection microstructures with high performance, they are either unreliable, difficult to implement, or have severe limitations making them impractical to implement.

Direct imprinting is arguable the simplest approach for microstructuring, which intuitively imprints a pattern directly on the material using a preformed micro-scale mold, in the same way as a stamp. The material is preliminary heated before the stamp is applied by exerting sufficient force. Imprinting can also be completed by rotating a

Constants of calculated ARM

Refractive index 3
Period 1 μm
Filling factor 0.98
Steepness parameter 3

Transmittance dependence on depth (a)
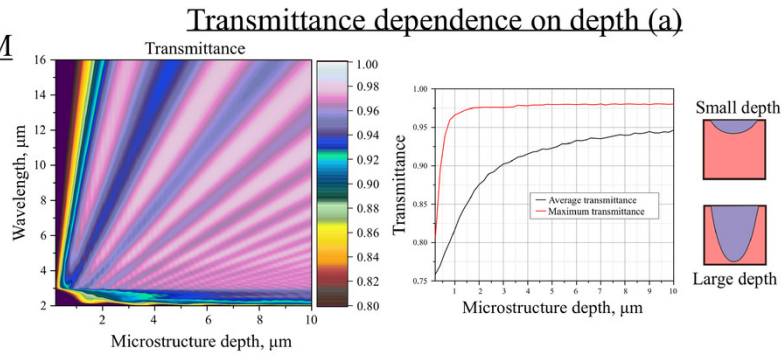
Refractive index 3
Depth 2 μm
Filling factor 0.98
Steepness parameter 3
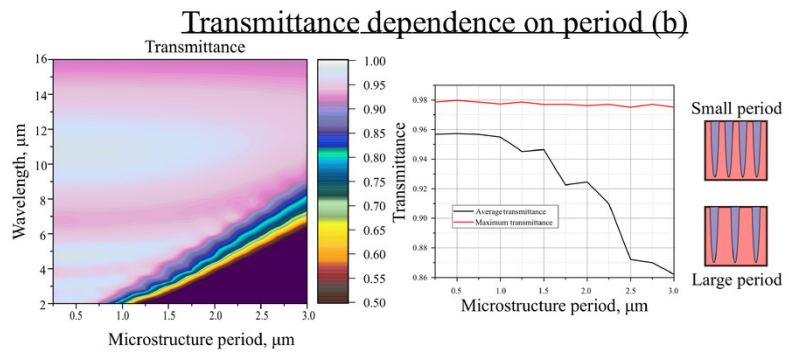
Transmittance dependence on period (b)

Refractive index 3
Period 1 μm
Depth 2 μm
Steepness parameter 3

Transmittance dependence on filling factor (c)

Refractive index 3
Period 1 μm
Depth 2 μm
Filling factor 0.98

Transmittance dependence on profile steepness (d)
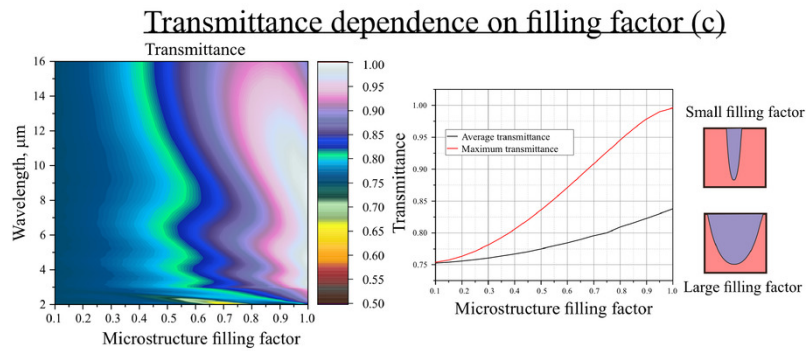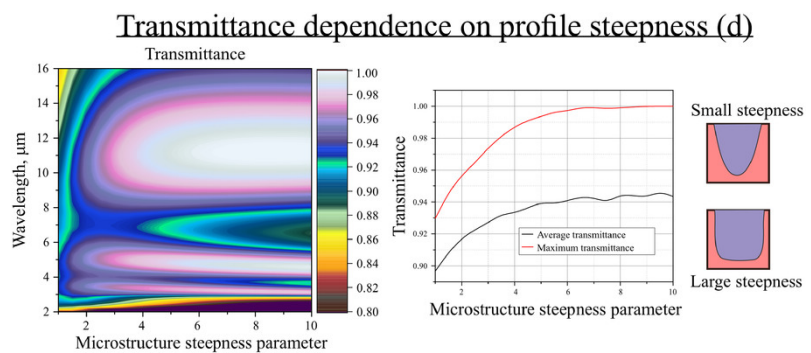
Figure 2.8: ARM dependency on morphological properties, like (a) depth, (b) period, (c) filling factor and (d) steepness[27].

18

wheel-formed mold onto the pre-heated sample. Though this method increases transmittance up to 98 % (for tested material)[27], it has some disadvantages, e.g. the need of different molds for every single type of structure and application.

Dry etching is a process in which a mask of a certain pattern is deposited to the surface before it undergoes reactive ion etching (RIE), where plasma is accelerated towards the surface. There are different ways to apply this mask, but the principle is the same for any of them. An advantage of this process is the high degree of control and precision, as well as the exceptionally high surface quality. An aspect ratio as high as 5-10, and a transmittance of 98-99 %, has been reached in ZnSe in 3.5-11 µm region[27]. However, the RIE method also has some negative aspects, as it is a rather complex and expensive method that requires a long fabrication time.

Wet etching is, such as dry etching, a well known technique. It is based on substrate removal by chemical reaction between the etching solution and the surface of the material. It is similar to dry etching in terms of the masking techniques that can be implemented, however, since wet etching uses a chemical solution instead of plasma, it can also be performed without masking, as well as it is a cheaper method of microstructuring. Although it is less accurate compared to RIE, it can still achieve a transmittance of 99 % (Si), although wet etching is mainly used effectively on silicon.

As mentioned above, femtosecond writing can also be used to produce microstructure ARCs. In a similar way to waveguide writing, this can be done by laser ablation with a pulse duration in the ultrashort regime with the sample positioned on a high precision stage. By processing the sample in this way, it is highly achievable to obtain reproducible periods lower than 1 µm, and it is possible to reach transmittance between 95-99%[27,29]. Ultrashort laser writing for ARM can be performed in different ways based on direct single pulse ablation[29]. Although the principal of these methods is the same, they have different auxiliary techniques to achieve increased depth (with fixed diameter), hence increased transmission, compared to "regular" direct single pulse ablation. The first method is with obstruction of peripheral rays. This is done by blocking part of a Gaussian beam before the objective lens and effectively results in a more narrow beam with lower intensity. A second method is direct single pulse ablation in presence of spherical aberration. By introducing spherical aberration between the objective lens and the sample, the peripheral rays will propagate further than the paraxial rays of the Gaussian beam, effectively defocusing the beam and stretching the point of interaction between the beam and the material. A third method relies on precise in-depth focusing and represents a rather simpler approach than the first two. The only auxiliary technique adopted here is to precisely shift the focal point of the Gaussian beam deeper into the material. All these techniques increased the depth in the material and, in turn, the average transmission of the ARM by approximately 94 % between 3-10 µm[29]. Notably, the third and simplest of these techniques led to an increase of 97 % (These methods were demonstrated on CdSSe).

Another way of increasing the depth of the structures is by transforming the Gaussian beam into a Bessel beam. Following this approach, the depth can be increased, while any adverse thermal effects that may occur by a Gaussian beam are mitigated[21]. This route for making anti-reflection microstructures is fast, simple, more cost-effective than RIE, and more versatile as it is implementable in different structures and materials.

2.2.2 In-bulk subsurface laser processing

Structures can be inscribed inside a substrate by focusing the beam to a spot under its surface. The use of objectives with high sufficiently high NA ensures that the material surface remains unmodified. In this case, it is not necessarily desirable to reach the ablation threshold of the material but to combine a tight focus scheme and direct writing. This will make it possible to create phase and structural changes inside the material, such as refractive index modification[7] (see section 2.3.4). This is possible due to the nonlinear nature of ultrafast laser interaction with transparent materials and keeps the modification within the focal volume of the laser beam[7,30]. Because of this, ultrafast lasers can completely alter physical and chemical properties of transparent materials. This has enabled the fabrication of integrated microdevices for application in photonics, optofluidics and optoelectronics, by creating waveguides inside the material due to refractive index change. These waveguides are building blocks for integrated optics, photonics, optomechanics and micro- and nanostructuring[30,31].

Waveguides

Tightly focused femtosecond lasers irradiation has been used since the 90s for inscribing waveguides in the bulk of various materials with different structural properties. A research team from Japan was the first to report the writing waveguides in glass using femtosecond laser pulses in 1996[7]. The writing approach they have implemented was slightly different from what is proving to be most efficient. They produced waveguides by increasing the refractive index in round-elliptical damage lines in glass, by inducing defects in its bulk perpendicular to the waveguide axis. Also, fabrication of waveguides by helical writing has been realized, by focusing the laser emission parallel to the waveguide axis and moving the stage in a helical manner[32], as shown in Figure 2.9. This way of writing waveguides has obvious limitations when it comes to length of the waveguide to be inscribed.

Tokel et al. [33] introduced in 2017 a way to make subsurface structures with single pulses, in silicon, by the interaction of the incoming beam and the beam reflected from the back surface of the sample. 3D structures can be inscribed, however, the method shows limitations when the processing of thick substrates is required. Another approach of writing waveguides that was adopted in this work, is by introducing a depressed cladding structure (as shown in Figure 2.5). In this way, the refractive index can be altered in the irradiated region by the high intensity beam, which is
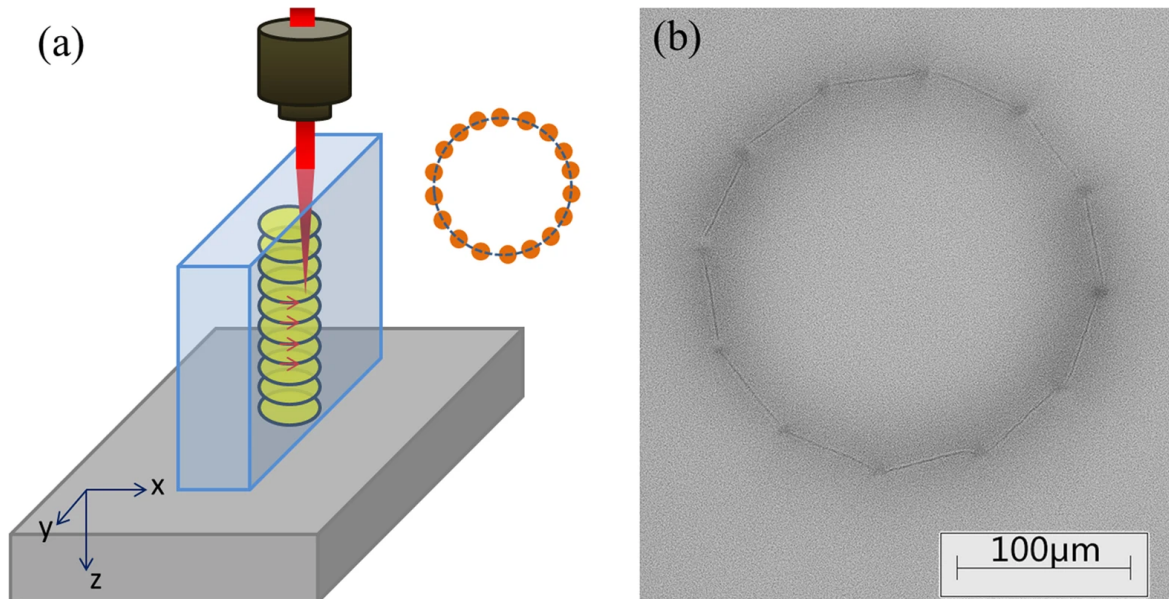
Figure 2.9: (a) Technique for laser writing waveguide by helical movement of the stage. (b) Picture of cross-section after writing[32].

directed perpendicular to the waveguide axis.

Instead of increasing the refractive index in the core, decreasing it in the cladding and maintaining the core area unmodified has proven to be a more efficient approach. In waveguides with an unmodified core area, the cylinder in which the light propagates is obviously more homogeneous than the alternative of having a modified core. This will mitigate loss due to scattering, and prevent any alteration of the spectroscopic properties of the medium[34]. The modified cladding around the waveguide core is formed by directing the beam perpendicular to the waveguide axis such that the core will be "surrounded" by these tracks made by the laser, as shown in Figure 2.10.

Here it is also possible to see the unmodified core in the middle of the cladding. The tracks that make up the cladding can also be seen to appear more or less straight with no interaction or damage between them. By focusing the laser writing beam tightly an using a high precision stage, the parallel tracks will not induce any adverse effects between each other, despite their proximity, being 3 µm or less apart (in Figure 2.10 specifically). The track height, and therefore its core shape, can be controlled by altering the pulse energy of the writing beam[34]. Also parameters such as translation velocity, wavelength, number of modified elements and number of translations per element contribute to both shape and properties of the final waveguide. This can be properties like, e.g. mode confinement that will affect irradiances. By advancing this field of study, it is possible to create 3D structures in bulk material that paves the way for in-chip microstructures, integrated optics and high-efficiency photonic devices, such as beam splitters and couplers[35], waveguide lasers in crystalline materials, as well
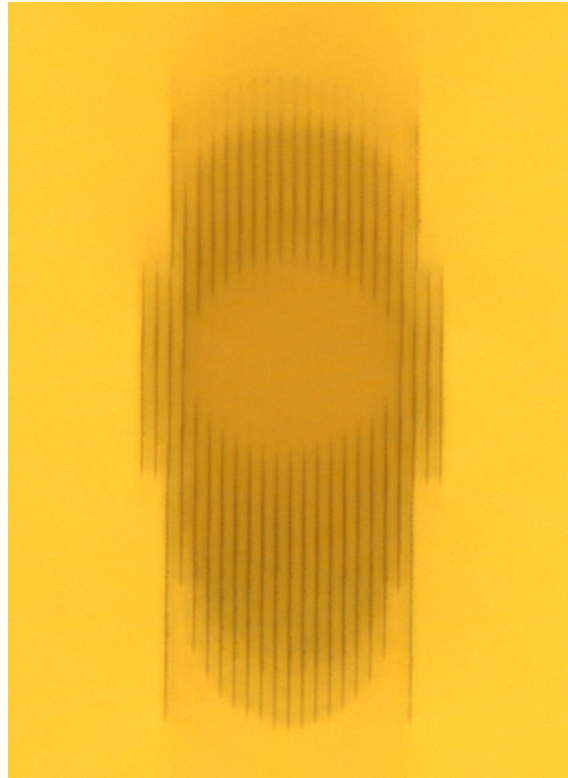
Figure 2.10: Cross-section of a depressed cladding buried waveguide in Cr:ZnS. Distance between tracks is 3 µm, and diameter of the core is equal to 50 µm.

as passive waveguide devices[8,34,36,37].

2.3 Modifications induced by ultrafast pulsed laser

Ultrafast pulsed lasers refers to lasers with pulse width or duration in the region of ps (10^{-12}) or shorter. The development of the chirped pulse amplification in a Ti:Sapphire regenerative amplifier[4] accelerated this field of research. This was to a great extent because of the ability produce high energetic fs (10^{-15}) pulses without inducing damage or undesirable nonlinear effects to the amplification medium. Chirped pulse amplification is achieved by introducing a strongly dispersive element so that the pulse is chirped and stretched before passing through the gain medium. Therefore, it does not cause detrimental nonlinear pulse distortion or destruction to the gain medium. Then the pulse is subsequently compressed back to the input duration by employing a dispersive compressor after the gain medium[38].

Ultrafast lasers can, on one hand, ensure precise control and manipulation of the states of materials and, on the other hand, can significantly reduce heat diffusion to the surrounding area[39]. This is due to the extraordinary high peak intensity of the pulses and their ability to interact with materials on a faster time scale than heat diffusion and lattice disorder do[40,41]. Since the pulse duration is shorter than the electron-phonon coupling relaxation time, the energy is only delivered to the electrons and is not dissipated to the lattice. This happens first after the pulse ends, and is one of the reasons why ultrafast lasers are currently being extensively used for both fundamental research and practical applications[30].

2.3.1 Basic principles

Ideally, the focal spot of an ultrafast laser will have a Gaussian-like spatial profile. This means that the modifications that takes place only occur in a limited area inside the focal volume. By matching the beam intensity in the focal spot to the threshold intensity of the material, extraordinary resolution down to the nanoscale can be achieved. Why a Gaussian profile is preferred is shown in Figure 2.11[30].

If the beam intensity is matched to the horizontal line in Figure 2.11(b), which is the reaction threshold for a given transparent material, in a combination with a high numerical aperture objective, modifications with sub-diffraction-limit resolution can be achieved. This approach has enabled a wide variety of phase and structural changes inside materials, such as waveguides by modifying the refractive index. Also nanofluidic channels have been achieved with the same process by reaching the ablation threshold inside the material[23].

This same method is relevant for most materials as long as the appropriate parameters are being used. First of all, there should be used a wavelength where the material in mind is transparent enough, such that the modifications are limited to the focal volume and not disrupted by linear absorption in the material itself. This means that the surface and the rest of the material structure will stay intact when irradiated at

23
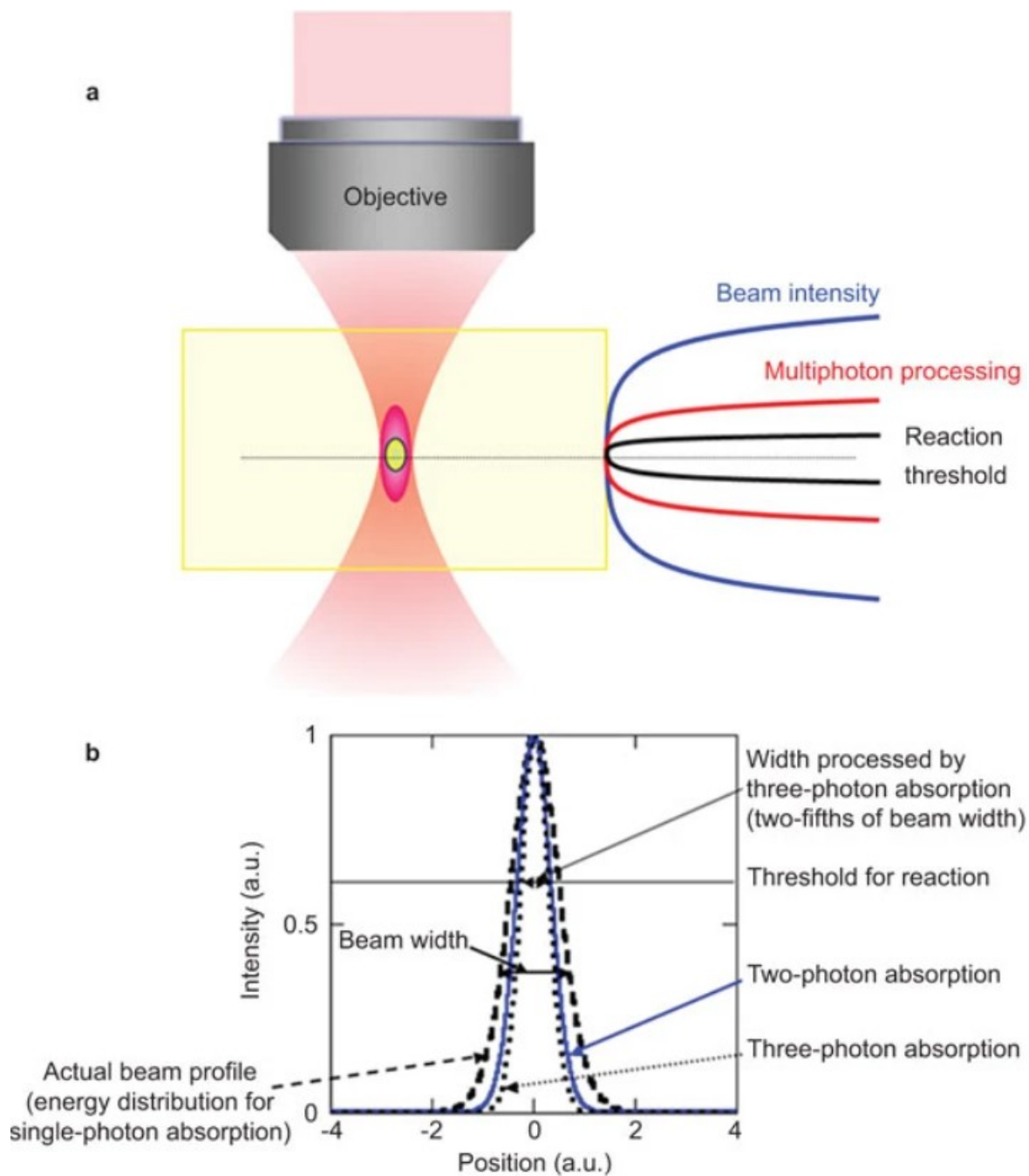
Figure 2.11: (a) Schematic illustration of beam intensity in the focal volume of a Gaussian beam. (b) Beam profile and spatial distributions of laser energy absorbed by transparent materials by two- and three-photon absorption[30] (more on this in section 2.3.2).

low intensities. By achieving high intensities in a small focal volume as described above, nonlinear optical effects such as multi-photon absorption (MPA) and tunnel ionization (TI) can occur.

As shown in Figure 2.2, the ZnS crystals mainly considered in this thesis have low absorption for wavelengths above 2 µm, and are therefore suitable for processing in this wavelength region. Subsurface modifications using ultrashort pulse in this wavelength region were first achieved in 2020 by the NTNU laser research group[42], then in silicon. To the best of my knowledge, subsurface modifications in ZnS using a similar setup at 2.1 µm are achieved for the first time during this theses.

2.3.2   Nonlinear optical phenomena

When transparent materials such as glass and wide-gap dielectrics are irradiated with ultrashort pulses, nonlinear effects appear. These effects result from the high intensities used and, therefore, do not play any significant role in low-intensity conditions. Generation of high intensities was first achieved with the realization of the first laser in 1960[2], and they allowed for the observation of nonlinear phenomena such as MPA and TI[43]. In the 1990s, this also led to the observation that by gradually decreasing pulse width, the damage threshold decreases and also a transition from a thermally dominated regime on the above ns scale to an ablative regime dominated by MPA, TI, avalanche ionization (AI) and plasma formation takes place[24,44].

Multi-photon absorption and other nonlinear effects

Multi photon absorption and other nonlinear effects of MPA occur when two or more photons are absorbed simultaneously by an atom or ion, thereby resulting in a transition of a single electron, as shown in Figure 2.12[45]. MPA, unlike linear absorption, is proportional to the nth power of the optical intensity. This results in a general expression for the attenuation of a light beam traveling through an optical medium[45]:

$$\frac{\mathrm{d}I(z)}{\mathrm{d}z} = -\alpha I(z) - \beta I^2(z) - \gamma I^3(z) - \eta I^4(z)... \tag{17}$$

where $I(z)$ is the incident beam intensity along the z-axis and the α, β, γ and η are the one-, two-, three-, and four-photon absorption coefficients of the transmitting medium.

By the end of the pulse the free electrons produced due to the induced MPA are rapidly heated, resulting in further ionization due to collisions (AI)[24].

For the optical breakdown in dielectric materials in the short-pulse regime, the general process is the generation of seed electrons by either MPA or TI with subsequent AI. AI happens first after electrons have gained energy due to either MPA of TI, and if the intensity if sufficiently high, further electrons are dissociated by electron-ion
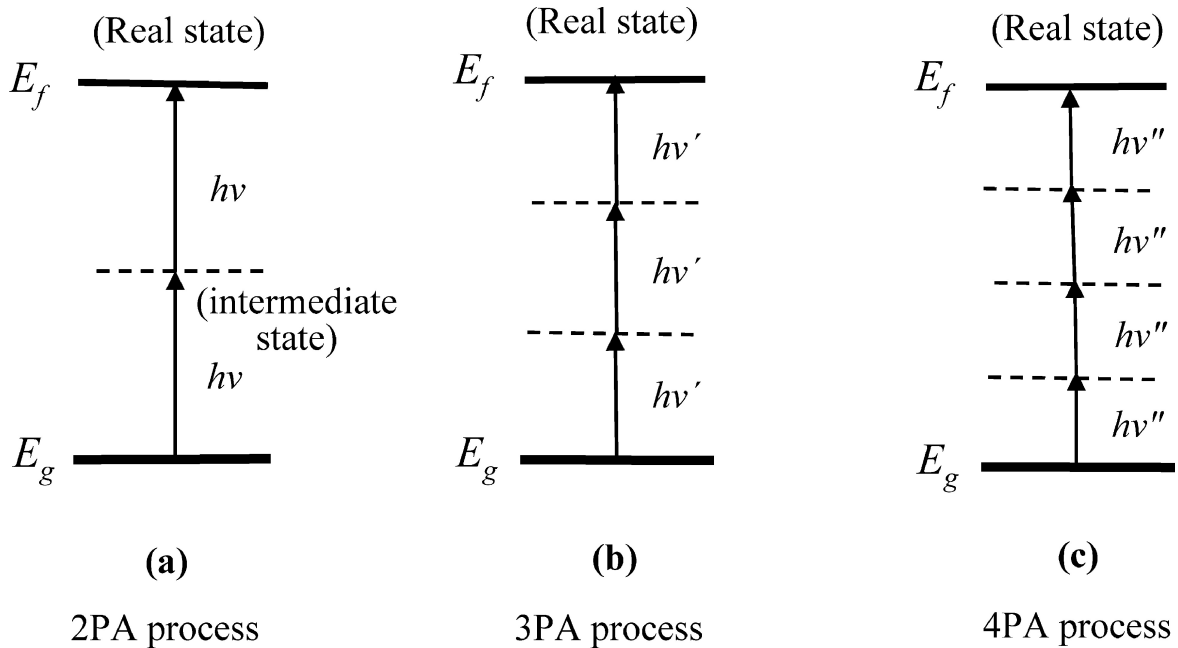
Figure 2.12: Schematic description of an elementary multiphoton-induced molecular transition process. Solid lines represent real eigen states; dashed lines represent intermediate states[45].

collisions[44]. The strength of these nonlinear processes depends on properties of the irradiated material, and the duration and wavelength of the laser pulses[24,41,46,47]. In wide-gap materials, Simanovskii et al. [41] demonstrated by optical breakdown measurements that the breakdown threshold decreases with wavelength in the mid-IR region. They claimed that this is because MPA is drastically reduced in this region due to the excessive increase in photons required to ionize a single electron. To indicate whether ionization happens in the tunneling, or the multi-photon regime, the Keldysh parameter γ was introduced in 1965[46].

$$\gamma = \frac{\omega \cdot \sqrt{m \cdot \Delta E}}{e \cdot E}, \tag{18}$$

where ω is the central laser frequency, ΔE is the band gap of the material, m is the electron-hole reduced mass and E is the laser electric field. This parameter indicates that for $\gamma \ll 1$ photoionization occurs in the tunneling regime and for $\gamma \gg 1$ in the MPA regime. Simanovskii et al. [41] thus concluded, in 2003, that for narrow-gap dielectrics with $\Delta E \sim 3$ eV, such as ZnS, TI is primarily responsible for mid-IR regime laser breakdown. Regarding the behaviour in the near-IR region, which is relevant to the samples studied in this thesis, the underlying mechanisms appears to be different. When irradiated with wavelengths in the near-IR domain, MPA produces a high seed electron density even for wide-gap materials, regardless that the MPA rate is still

orders of magnitude lower than predicted by Keldysh theory[46]. This indicates that for wide-gap materials in this wavelength region, iAI seems to be dominating, with MPA introducing initial seed electrons for pulse durations down to 10 fs. In contrast, for narrow-gap dielectrics, MPA alone dominates the optical breakdown process for pulse durations below 100 fs and up to 10 ps[24,47].

Other nonlinear optical effects might also occur during irradiation by ultrashort pulses, such as, e.g. self-focusing. Self focusing results from the Kerr effect, which can occur when light propagates through crystals[48], and acts effectively as a change in the refractive index due to electric fields. This refractive index gradient thus act as power dependent lens and cause the beam to focus by itself while propagating through the medium[49].

2.3.3 Ultrashort pulses - ns vs. fs regime

As mentioned earlier, modifications induced by laser irradiation are highly dependent on pulse duration. In the duration regime longer than a few tens of ps, this irradiation will cause substantial heating to electrons and dissipate to the lattice. This will result in melting and boiling of the material[24]. As mentioned in section 2.2, this material processing technique can be used for structuring on and below the surface, and for industrial applications, such as drilling and cutting.

Due to their potential to interact with the material faster than heat diffusion, ultrashort pulses are suitable for high-precision processing without any HAZ. However, this is not the case for processing in the ns regime since the generated thermal waves have sufficiently long times to propagate into the material and create layers of melted material that have not been vaporized[39]. These heat-affected zones in the material can also induce shock waves that can result in cracks along the edges of the modified parts[50]. Although material processing in industrial settings is widely being performed in the ns regime, the use of ultrashort pulses can admittedly yield higher resolution, better edge quality and severely reduce peripheral thermal effects.

2.3.4 Permanent modifications - Change in refractive index

Microplasma formation will eventually occur in the focal volume, where the intensity is sufficiently high to induce ionization, as described in section 2.3.2, when creating subsurface structures. This is driven by the free electrons generated by MPA, TI and/or AI, inducing structural alterations in the same region due to changes in the optical density of the material. This results in a refractive index change[51,52,53,54]. In literature, this process is usually a combination of two steps, of which the first step is the ionization process. This step is relatively known for both glasses and crystals since it is mostly dependant on the materials energy gap and nonlinear absorption coefficients of the material[51]. The second step is less straightforward. In glasses, it

is generally accepted that the refractive index change is positive due to melting, and densification of the exposed region[7,51,52], although negative change is also possible. In crystals, however, it seems to be more complex. Okhrimchuk and Duarte [51] reported in 2010 that the refractive index changes in crystals can usually be assumed to be negative in the ultrashort laser-induced region due to amorphization, but that it causes stress and thus positive changes along the edges of the defects. Experiments with a Cr^{4+}:YAG crystal also revealed that it is possible to induce both negative and positive refractive index change in the same crystal. When positive refractive index changes were observed, the repetition rate was adjusted to a relatively high setting at 11 MHz. Using sufficiently high pulse energies and low enough writing speed, a $\Delta n \approx 2.5 \cdot 10^{-4}$ was obtained. With increasing writing speed or decreasing pulse energy, the refractive index changes became negative in the same crystal. However, when the laser system with a repetition rate of 1 kHz was introduced in the setup, all experiments resulted in negative Δn[51].

This indicates that the contribution of each of the possible responsible mechanisms to the refractive index changes in materials, (i.e., stress changes, material densification, amorphization, formation of color centers, melting and resolidification), depends on the material and the processing conditions[7,51,52,53,55,56,57].

Even though waveguides in bulk glasses based on positive refractive index change often yield higher $|\Delta n|$ (up to 10^2)[7], waveguides in crystals have some favorable properties, especially regarding laser optics. Among these are the possibilities of better thermo-conductivity and a higher optical damage threshold. Also, the negative refractive index makes the depressed cladding structure possible, leaving the waveguide core unperturbed. This will mitigate losses due to scattering and, in addition, will provide a large variety of options when it comes to core diameter. A small core that is often formed in bulk glasses with positive Δn core, is often characterized by a very small $V\,number$ which can be calculated as

$$V = \frac{2\pi r}{\lambda}\text{NA}, \tag{19}$$

if we assume that the waveguide in question has a step-index structure, then the $V\,number$ will provide an estimation of the mode confinement and thus the mode radius of the waveguide. The mode radius can be approximated using Marcuse's empirical formula[58],

$$\frac{w}{a} \approx 0.65 + \frac{1.619}{V^{3/2}} + \frac{2.879}{V^6}. \tag{20}$$

Since the $V\,number$ impacts the mode radius of the waveguide, low $V\,numbers$ can ultimately result in weak waveguiding since the mode of the waveguide will extend largely

outside the core[56]. This will also introduce bending losses, which, in turn, renders challenging for the realization of structures such as couplers or bent waveguides.

Wavelength dependency of defect size

In a study that included both numerical simulations and experimental data, Richter et al. [42] concluded in 2020 that the shape of the elongated subsurface defects created by ultrashort lasers is dependent on the laser wavelength. Also, it was demonstrated that with longer wavelengths for laser processing, more localized and confined structures can be produced with higher repeatability.

2.4 State of the art

2.4.1 Laser technology

The operation of lasers based on laser-inscribed waveguide structures has been successfully demonstrated several times in various materials, including Cr:ZnS[17,8]. They have proved the principals that have been motivating the research in Cr^{2+}-doped chalcogenides, such as tunability and compactness. The latter partially due to the inscribed waveguides in the material. A compact buried channel waveguide laser in Cr:ZnS was demonstrated in 2014. It had a cavity length of 6 mm and operated at a wavelength pf 2332.6 nm with a slope efficiency of 20 %, generating outputmpower up to 101 mW[17]. As there was no anti-reflection layer on the end facet of the structures, the calculated Fresnel reflections had to be subtracted to determine the slope efficiency. However, although reflections on the waveguide facet were neglected, they were not physically removed. The pump used in these experiments was a Tm:Fiber emitting at a wavelength of 1928 nm. This experimental demonstration led to enhancement of the laser performance in subsequent reports, paving the way for further optimization of the waveguide structures and geometries and reduction of losses due to, for example, reflections. Since the waveguide gain medium was polycrystalline Cr:ZnS, the possibility of demonstrating similar results in single-crystalline Cr:ZnS was yet to be explored and was finally achieved first in 2019[8]. Here, an average output power of 150 mW was obtained at 2272 nm wavelength with a slope efficiency of 11 % by pumping with an Er: fiber laser. In addition to being inscribed in a single-crystal, the waveguide structure used as a gain medium was single-mode.

As mentioned in section 2.1.2, an erbium fiber laser has an emission wavelength that coincides with the absorption spectra of Cr: ZnS, and thus is more suitable as a source for optical pumping of this gain medium. As for pumping of single-mode waveguides, this laser is desirable due to the modal dispersion occurring in multi-mode geometries, as in the structure used in[17]. A single-mode waveguide supports the propagation of only a single mode per polarization direction and thus limits the distortion of the beam at the output. The experiments on the doped Cr^{2+}:ZnS characterized during this thesis were based on the possibility of further optimizing the single-mode-, single-crystal-based Cr:ZnS waveguide demonstrated in[8].

2.4.2 Buried modifications in active and passive ZnS

Writing waveguides in ZnS has not been extensively studied but has been achieved quite a few times in the last nine years. The first buried depressed cladding waveguides in ZnS were demonstrated by An et al. [59] in 2013, with several being realized the following years. All these experiments were conducted with different parameters, and thus direct comparison of the results obtained is difficult. To provide an overview of the current state-of-the-art research in buried channel waveguides in ZnS and Cr:ZnS,

table 2.4.2 summarizes the results collected from literature during this thesis.

Table 1: Overview of laser-induced waveguides in ZnS/Cr:ZnS crystals.

Ref.	τ (fs)	λ (nm)	Rep. rate (kHz)	E (µJ)	NA[a]	Speed[b] (mm/s)	Modification geometry	Δn^{c} (10^{-3})	Material
			Writing parameters						
[59]	120	800	1	2.5	0.65	0.5	Structures made with different diameter with 3 µm DBE.[d] The 50 µm waveguide showing single-mode confinement in the MIR region of 4 µm. Losses were measured to be ~3.9 dB/cm. The cross-section is somewhat circular but with "flat bottom", and each defect have a small height relative the core diameter.	5.2	ZnS
[60]	800	1028	100	0.5	0.85	5	Buried channel waveguides of diameter 40 µm shows multi-mode confinement at 1030 nm, with a low loss of 0.62 dB/cm. Quite elongated defects is shown.	~ 2.3	ZnS
[17]	400	~1040	100	0.3-1.5	0.6	9-20	First channel waveguide demonstrated in Cr:ZnS. Smallest WG supporting guiding was 50 µm, although best results were obtained in 60 µm with 40 elongated defects of height ~25 µm, written at 20 mm/s.	n/a	Cr:ZnS

Continued on next page

| Ref. | Writing parameters | | | | | | Modification geometry | Δn^{c} (10^{-3}) | Material |
	τ (fs)	λ (nm)	Rep. rate (kHz)	E (µJ)	NA[a]	Speed[b] (mm/s)			
[8]	800	1028	100	0.35	0.85	0.25	First single mode Cr:ZnS buried channel waveguide laser in single-crystal. With 3 µm DBE[d] different core diameters were written around 50 µm by adjusting the number of elements. The waveguide cladding defects are elongated with a length ranging between 30 and 60 µm.	n/a	Cr:ZnS
[32]	130	800	1	120	0.4	n/a	Structures were made of helical writing mentioned in section 2.2.2. Waveguides with diameter of 100-200 µm were made, with the best 200 µm yielding best performance as a laser. The losses were ~0.38 dB/cm at 2.38 µm.	n/a	Cr:ZnS

[a] Numerical aperture of the focusing lens.
[b] Writing speed of the defect lines that makes the waveguide.
[c] Change in refractive index between core and cladding. Not always included in literature on Cr:ZnS.
[d] Distance between each defect element.

As described above, there is only a limited number of reports in the literature containing experimental results on laser-induced buried waveguides in ZnS, and only two of them explicitly reports measurements of the laser-induced refractive index change in the material. All waveguides reported so far have been inscribed using lasers emitting at 800 nm or around 1030 nm and operating with repetition rates of 1 or 100 kHz.

The waveguides listed in the table above were all written using the same concept, involving the writing of lines in a direction perpendicular to the beam, except for one, written in a helical manner. If we consider all these reports, An et al. [59] were the only ones demonstrating defects of few micron sizes as seen from cross-sectional views. However, the best of these waveguides in terms of mode confinement exhibited losses as high as $\sim$ 3.9 dB/cm. As determined by Richter et al. [42], this parameter is dependent on the irradiating laser wavelength, although it seems it also depends on the repetition rate and pulse duration. The waveguides with the smallest size in ZnS capable of supporting light guiding of some wavelength so far reported had a diameter of 40 µm and exhibited multi-mode confinement. To the best of my knowledge, the is no report on buried channel waveguides inscribed using wavelengths longer than 1040 nm. To the best of my knowledge, no laser-induced buried cladding waveguides have been reported using wavelengths longer than 1040 nm.

3   Methodology

The laser used to induce defects, such as lines and waveguides in almost all the samples studied in this thesis, was a fiber-based system with a tunable repetition rate set to 10 kHz or 20 kHz. It generated pulses of duration between 4 and 6 picoseconds at a central wavelength of 2.1 µm. The pulse energy was adjusted between 0.35 µJ and 2.75 µJ when inducing defects to determine optimal parameters for writing waveguides. All the structures investigated were inscribed by this laser, except for those in the Cr:ZnS sample. These waveguides were fabricated in earlier experiments with a femtosecond laser emitting at a central wavelength of 1028 nm at 100 kHz and investigated in[8]. Our collaborators in Moscow have recently manufactured ARMs on the facets of the waveguides and provided us with the sample for further investigations. Figure 3.1 shows the experimental setup used to write structures in all the ZnS samples.
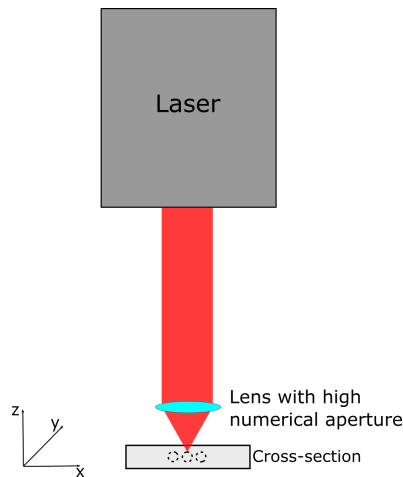
Figure 3.1: Experimental setup for writing in-bulk structures.

By using a high precision 3D stage, appropriate writing speed and depth for different structures can be written. Thus by moving the stage along the y axis as shown in the figure, elongated patterns can be written through the whole sample.

3.1   Samples investigated

In this thesis, a total of five undoped ZnS samples were investigated and one Cr:ZnS sample. In two undoped ZnS samples, line defects were inscribed using different writing parameters to identify the optimal writing characteristics for the waveguides to be subsequently written in the other three samples. As mentioned above, the waveguides in the Cr: ZnS sample, were fabricated earlier using a different laser system. All the structures inscribed with the 2.1 µm laser system were buried modifications in the

bulk of the materials, formed with a 100x magnification objective with NA of 0.85, as described in section 2.3.1. Hence, the surface of all samples remained unmodified.

The Cr:ZnS sample was all-laser micro-processed with waveguides and anti-reflection microstructures on both facets of three of the buried waveguides in its bulk. The ARM was produced using single-pulse laser ablation, with 200 fs pulses, at a 20 kHz repetition rate and a 513 nm wavelength, focused with a 0.5 NA objective lens.

Polishing

To inspect the cross-sections of the fabricated structures, it was necessary to polish the end faces of the samples. The polishing process is essential for samples containing waveguides because an unpolished facet will cause the scattering of an incoming beam. Figure 3.2 shows microscope images of waveguide cross-sections recorded before and after the polishing of their end faces, thereby demonstrating the difference in the surface quality. It can be realized from the images that it is almost impossible to distinguish the laser-induced defects from other surface damages on the unpolished facet.
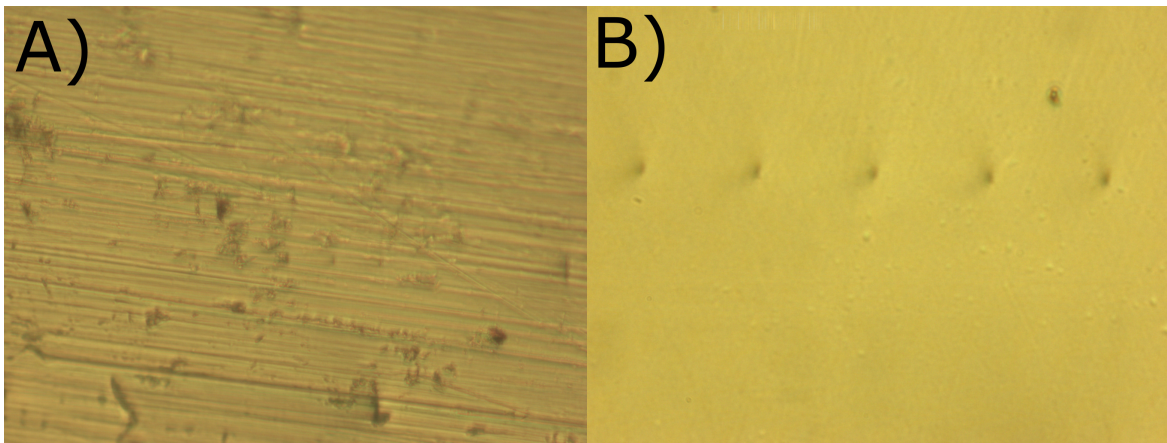
Figure 3.2: Comparison of unpolished cross-section (A) and polished cross-section (B) of line defects in one of the samples investigated.

The polishing process was performed using a slightly modified Fiber Polisher from Krelltech, that comprised a rotating disc with interchangeable polishing papers. The sample was then mounted to the holder with Pelco Quickstick mounting wax and pressed against the rotating grinding disc that had attached polishing sheets made of silicon carbide. Both cross-sections of each sample were polished with decreasing grain size. The grain sizes used were 30, 9, 3 and 0.3 µm, to achieve optical quality from the polishing process. This process limits the roughness of the facets and reduces loss due to scattering when further characterization with a coupled laser beam is performed.

The challenge encountered with this setup was the difficulty in polishing such that the

waveguides were perpendicular to the sample end facets, and the opposing waveguide end facets were perfectly parallel. This was due to the way the ZnS samples were mounted manually on the holder and the manual adjustment of the polishing angle. This polishing process resulted in small-angle deviations from a perfect perpendicularity and, eventually, in higher Fresnel reflections at the interface when a laser beam enters the waveguides.

3.1.1 Parameters of induced defects

Optimal parameters for writing waveguides were established by investigating numerous line defects, specifically by characterizing the size and shape of each defect. The parameters adjusted to inscribe each set of defects were, in principle, the writing speed, inscription depth, and laser pulse energy. Defects were using various pulse energy settings for each depth and writing speed.

The line defects in the two ZnS samples (i.e., before proceeding to waveguide writing) were formed using the following parameters:

- Sample 1: The defects in the first sample were formed with the speeds of 20, 10, 8 and 6 mm/s and energies of 0.38, 0.73, 1.26, 1.93 and 2.75 µJ, at depths of 0.03, 0.045 and 0.06 mm. Five defects of each parameter were inscribed, resulting in 60 zones of lines with a total of 300 lines. The laser repetition rate was set to 10 kHz for all the inscriptions.

- Sample 2: The defects in the second sample was written with the speeds of 20, 16, 12, 8 and 4 mm/s, at depths of 0.03, 0.04, 0.05 and 0.06 mm with the laser pulse energies 0.5, 0.75, 1.0, 1.25, 1.5, 2.0 and 2.5 µJ. A laser repetition rate of 20 kHz was used for inscribing all the defects, resulting in the formation of 140 zones of lines, with each zone containing 3 lines thus creating a total of 420 line defects.

3.2 Characterization

The main task of this thesis has been to investigate single-line defects in passive undoped ZnS media to determine optical parameters for writing waveguides and then estimate parameters of the inscribed structures, such as NA, Δn, mode confinement and loss. The methods used in this thesis for the waveguide investigation are listed in the following paragraphs.

3.2.1 Optical microscopy

Since ZnS is transparent in the visible spectral region, bright-field optical microscopy appeared to be the easiest and fastest way to determine these buried modifications. It also enabled focusing on the material from above to visualize the line defects written in different depths. The potential of this characterization approach is demonstrated in Figures 3.3 and 3.4, showing top-view and cross-sectional images of defects written at various depths in the bulk of a ZnS sample.
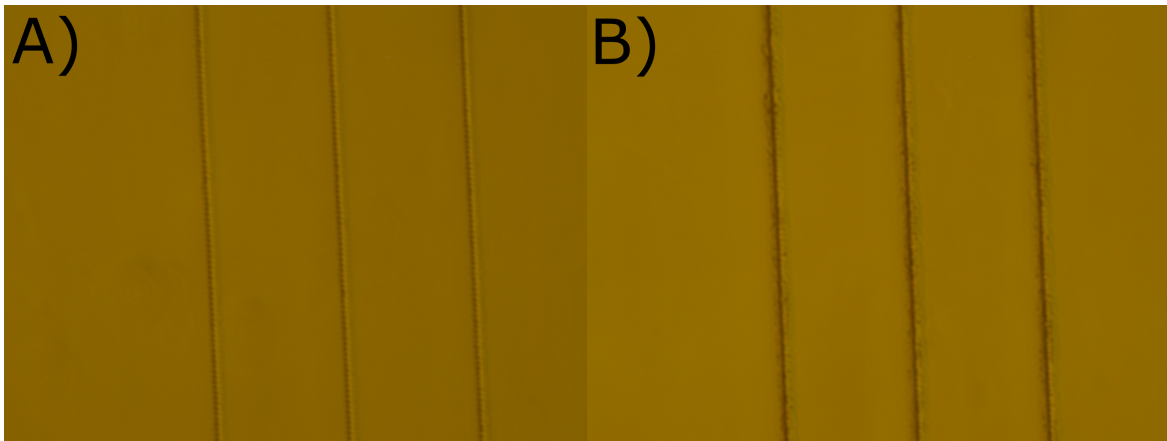
Figure 3.3: Optical microscopy from the top showing two different zones of the same sample. A) Is a zone written with speed 20 mm/s, energy 2.0 µJ at a depth of 0.03 mm, and B) is written with the same speed and energy, but at a depth of 0.06 mm.

Bright-field optical microscopy allowed for the impact of the inscription depth on the size and shape of the structures to be assessed for fixed pulse energy and writing speed settings.

3.2.2 Waveguiding - Infrared transmission microscopy

The guiding properties of the inscribed defects were studied with an infrared (IR) transmission microscopy setup. In Figure 2.2, it is apparent that Cr:ZnS shows high absorption between 1.5 and 1.8 µm, hence using a pump source in this spectral region is ideal for the best performance of a Cr:ZnS-based laser system. To study the
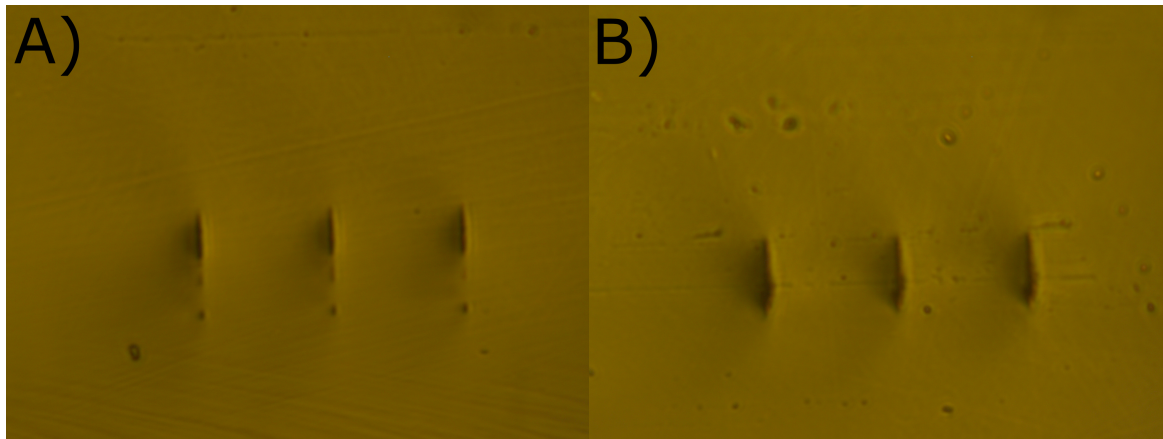
Figure 3.4: Optical microscopy from the cross-section showing two different zones of the same sample. A) Is a zone written with speed 20 mm/s, energy 2.0 µJ at a depth of 0.03 mm, and B) is written with the same speed and energy, but at a depth of 0.06 mm.

waveguiding properties and characterize the waveguides using a wavelength in this spectral region, may introduce losses due to this absorption. Nevertheless, due to the unavailability of 2.4 µm lasers, which is the emitting wavelength of Cr:ZnS, and a limited sensitivity for the available camera, a 1.55 µm laser was used. Thus, the IR microscopy at this wavelength, of 1.55 µm, was implemented to conduct most of the measurements in the laser-written waveguides. A scheme of the setup is displayed in Figure 3.5, indicating that in addition to the fiber laser, a broadband light source was used to illuminate the sample to enable the recording of top-view and cross-sectional images of the waveguide.
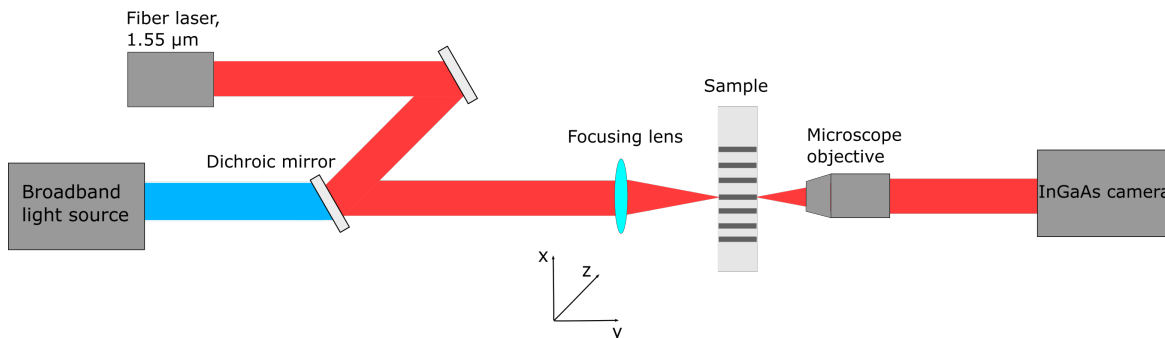
Figure 3.5: Scheme of the IR microscopy setup used for waveguide experiments when looking at the cross-section. For guiding the 1.55 µm laser into the waveguides, a 35 mm plane-convex focusing lens is used. In addition to the guiding laser, a broadband light source is introduced via a dichroic mirror for visualizing the surrounding area of the cross-section. Both the ZnS sample and the microscope objective are placed on 3D stages so that optimal alignment is possible.

Light emitted from the broadband source was directed toward the waveguide using a

dichroic mirror. The incoming beam from the fiber laser and the broadband light were both focused on the waveguides by a plane-convex lens with a 35 mm focal length. In this setup, the position of the sample and microscopic objective can be precisely adjusted, since they were both placed on 3D stages with micrometer resolution. Furthermore, it was possible to focus the objective inside the sample but also on its front facet to facilitate the laser beam coupling into the waveguide. Images recorded with this setup are displayed in Figure 3.6, showing the same waveguide with and without the 1.55 µm laser beam coupled into it.
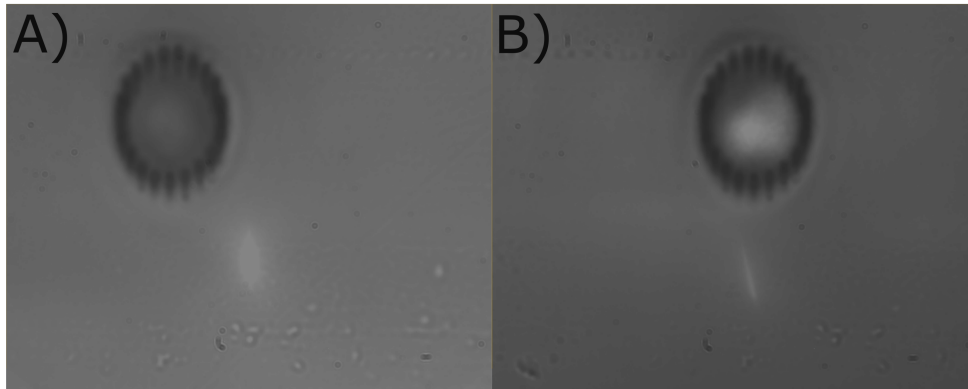

Figure 3.6: IR microscopy from the back facet of ZnS sample with waveguides. A) Shows waveguide only illuminated with broadband source, while B) shows illumination with broadband source and laser coupled into the waveguide.

3.2.3   Determining NA and Δn

To determine the mode confinement of the waveguides, the NA needs to be estimated and, in turn, the refractive index change Δn. For deriving the NA, direct numerical aperture measurements were conducted using the setup in Figure 3.7.

By placing an imaging camera as close as possible to the output of the waveguide and moving it stepwise backward, one can estimate how the beam is spreading as it exits the waveguide. By processing these recorded images, one can obtain an intensity profile and subsequently fit the laser beam to a Gaussian profile, plot the output beam size, and eventually estimate the NA for both the horizontal and the vertical direction. The recording of utilizable images requires that the laser beam intensity is suitably adjusted so that the camera is not saturated. When implementing this method, the camera was successively moved in five steps, each corresponding to a 5-mm distance. The same setup was used by Wortmann, Ramme, and Gottmann [54].

For a known NA value, the refractive index change can be derived from eq. 8. As mentioned in section 2.1.3, ZnS has quite a high thermo-optic coefficient and, therefore,
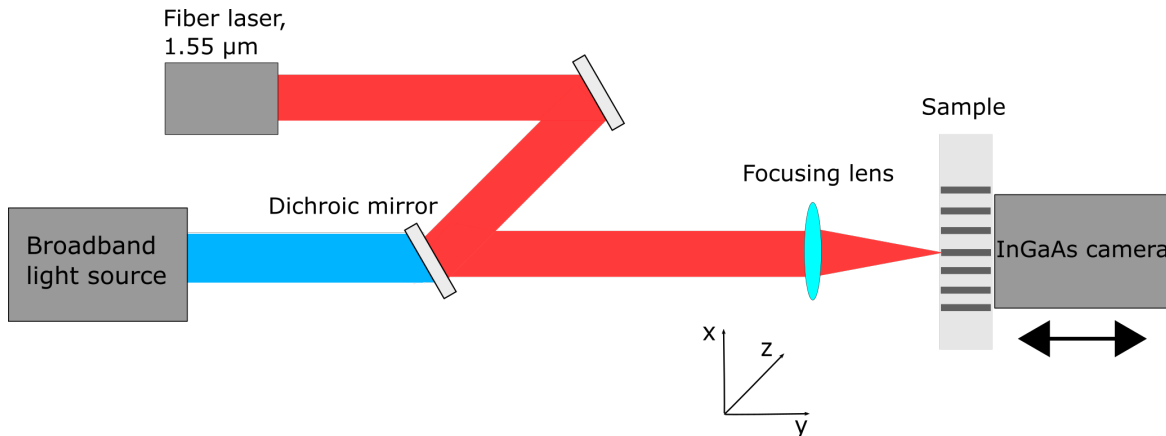
Figure 3.7: Setup for measuring NA. The InGaAs camera is placed as close as possible to begin with on a precise 1D stage so that it is movable by mm precision.

adverse thermal effects such as thermal lensing, are likely to occur. Thermal lensing can be considerably suppressed by adopting waveguide geometries, particularly waveguides exhibiting single-mode guidance[61]. By assuming a step-index waveguide and calculating NA, the $Vnumber$ of the waveguide can be derived from eq. 19. Thus, by estimating NA, one is able to estimate the refractive index change and determine if the waveguide is single-mode or multi-mode. If the $Vnumber$ exceeds the value of 2.405, the waveguide can be considered multi-mode, with the number of modes being approximately $V^2/2$.

3.2.4   Waveguide loss measurements

The setup used for measuring waveguide loss was a simple modification of the method used by Grivas et al. [20] and Brülisauer et al. [62]. Grivas et al. [20] used the self-pumped phase conjugation method (SPPC), but the adaptation of this method used here did not include a BaTiO$_3$ crystal. Therefore, only the physical setup of the measuring system was similar. Figure 3.8 shows the loss measurement layout, in which the irradiation of a 1.55 µm fiber laser was coupled into the waveguide using the IR transmission setup.

In this experimental arrangement, the camera was removed, and the laser power was increased to ensure its detection by the power meter. As seen in Figure 3.8, the first measurement was conducted at position A, before the waveguide, so that loss originating from the focusing lens could be neglected. The two subsequent measurements were performed at the same position, designated as B and C in Figure 3.8(i.e., they spatially coincide), the first with the waveguide in place (B) and the second without the waveguide (C). In this way the transmittance of the microscope objective can be evaluated. The waveguide loss in decibels per unit length α^{20} can then be calculated by using eq. 13.
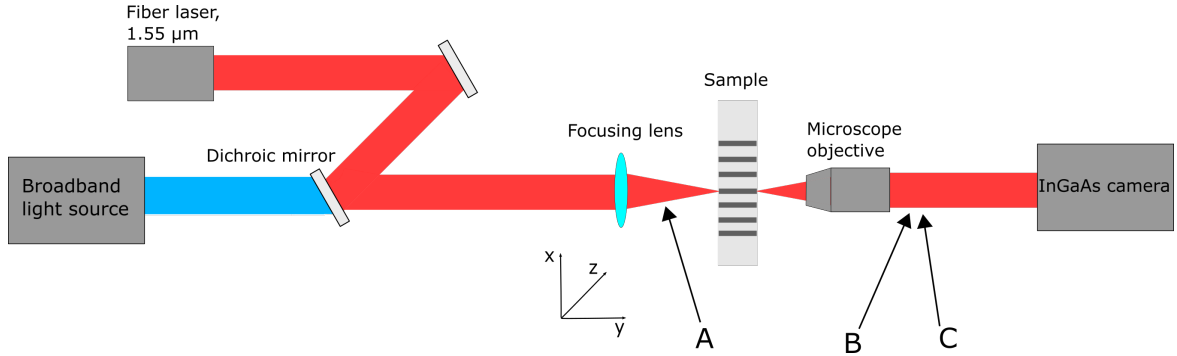
Figure 3.8: Setup for loss measurements in waveguides. A power meter is inserted in position A, B and than C. The difference in B and C is that for the C measurements the sample is removed so that the transmittance through the microscope objective can be measured.

The SPPC crystal used in the original realization of this method by Grivas et al. [20] allowed the elimination of the incurring coupling losses. However, in the simplified experimental layout used here, no SPPC crystal had been introduced. Thus, coupling losses need to be considered and evaluated. To this end, the coupling area of the fiber laser irradiation into the waveguide was considered equivalent to the corresponding area between two spliced fibers. In this case, the coupling efficiency η can be approximated as[63]

$$\eta = \exp\left[-\left(\frac{\pi\Delta\theta w}{\lambda/n}\right)^2\right]. \tag{21}$$

Here $\Delta\theta$ is the angle offset between the crystal facet and the waveguide, w is the mode radius of the incoming beam, λ is the wavelength, and n is the refractive index of the waveguide core. By introducing eq. 21 into eq. 14 a modified expression for the transmission factor is obtained as

$$K = T_o \cdot T_{FR} \cdot \eta. \tag{22}$$

3.2.5 Lasing experiments

An essential part of the characterization of the ARM in the doped Cr:ZnS sample is to obtain lasing of the material in order to determine the ARM transmittance. This step will also allow the measurement of output power as a function of pump power and, thereby, provide an estimate of threshold and slope efficiency. Demonstration of lasing was completed using a simple setup of a plane-parallel cavity similar to that depicted in Figure 2.1, with dichroic mirrors placed at each facet of the 7 mm waveguide. The input couple rwas a mirror highly reflective in the spectral region from 2.1 µm

to 2.5 µm, and transmissive around 1.6 µm. The output coupler exhibited a 10% transmittance in the wavelength domain between 2.1 and 2.5 µm. The waveguide was optically pumped by coupling the 1.61 µm output of an Er:fiber laser into the cavity with an anti-reflection coated plane-convex lens with focal length of 50 mm.

3.2.6 SEM

The morphological characterization of the ARM structures on the Cr:ZnS sample was performed by scanning electron microscopy (FEI SEM APREO). In SEM, an electron beam is directed perpendicular to the surface so that the backscattered ,and scanning electrons can be measured by detectors placed further up in the instrument. In this way, the interactions of the electron beam with the atoms in the sample can generate surface images. The SEM technique allows the recording of images of high resolution and very high magnification.

In this work, images were recorded by applying several different settings, including a few with a magnification of 25000. The latter were obtained with the T2 detector in the instrument using the Optiplan Lens mode by establishing an electrostatic field between the detectors and the sample. Recordings were obtained by applying a voltage of 10 kV, a current of 25 pA, and positioning the samples with a tilt of 40 °.

3.2.7 Micro-Raman spectroscopy

The changes in Raman scattering in the ARM were measured using micro-Raman spectroscopy (Renishaw InVia Reflex Spectrometer System). This characterization technique measures a delayed nonlinear response in the crystal lattice when a laser beam propagates through the medium, the so-called Raman shift. This form of scattering is associated with vibrational optical phonons. Unlike Rayleigh scattering, Raman scattering has components of different frequencies compared to the incident beam.

The measurements were carried out with an unpolarized backscattering geometry in a configuration that comprised a 532 nm laser setup with a tight 0 % focus, an objective with x50 magnification and a 2400 l/mm grating. The laser power was set to 10 % of its maximum output value, and each measurement comprised 10 accumulations, with an exposure time of 1.5 s.

4   Results and discussion

4.1   Overview

The experimental setup for inducing buried, in-bulk modifications is described in section 3. Figure 4.1 displays a representation of the inscriptions in the samples, where A) shows single line defects written as a first step to determining optimal writing parameters and B) shows the geometry of waveguides written using the optimized parameters. As mentioned in section 3.1, the first two samples (i.e., samples 1 and 2) were processed with the configuration to form structures similar to those displayed in Figure 4.1A, and the third one (i.e., sample 3) to inscribe waveguides with the geometry depicted in Figure 4.1B.
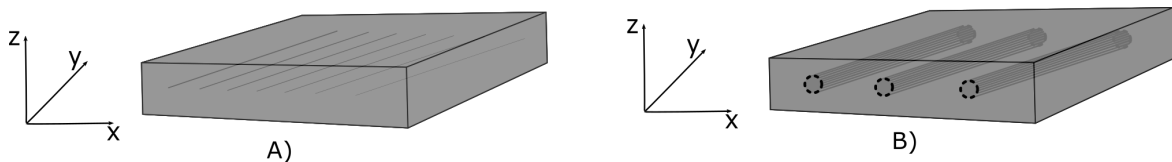

Figure 4.1: Representation of how the structures were written in the samples. A) shows single line defects while B) shows waveguides.

The third sample was a ZnS crystal and was the most investigated among the three samples since it was the one where waveguides were encoded with a 2.1 μm laser. Details on the writing parameters adopted to process this sample in section 4.3.

4.2   Size and shape of line defects

The size and shape of the line defects written in the first two samples was studied to optimize parameters when it comes to writing speed, inscription depth in the bulk of the material, laser power and repetition rate for writing waveguides in the same material. As 200 sets of defects and a total of 720 lines were inscribed in samples 1 and 2, only the results that reveal important information on the dependencies of the defect size and shape are included. Top-view and cross-sectional microscope images of structures inscribed in sample 1, with writing speeds of 20, 10, and 6 mm/s at a repetition rate of 10 kHz, for two different pulse energies and at three different depths, are shown in Figures 4.2, 4.3 and 4.4, respectively. The depths listed in these figures correspond to the scripted inscription depths of the structures in air. These depth values will be affected by the change in refractive index when the laser beam enters the medium from air, and, therefore, they do not correspond to the effective inscription depth of the defects[b].

---

[b]All subsequent inscription depths mentioned correspond to scripted depth in air, as described above. This applies unless stated otherwise.
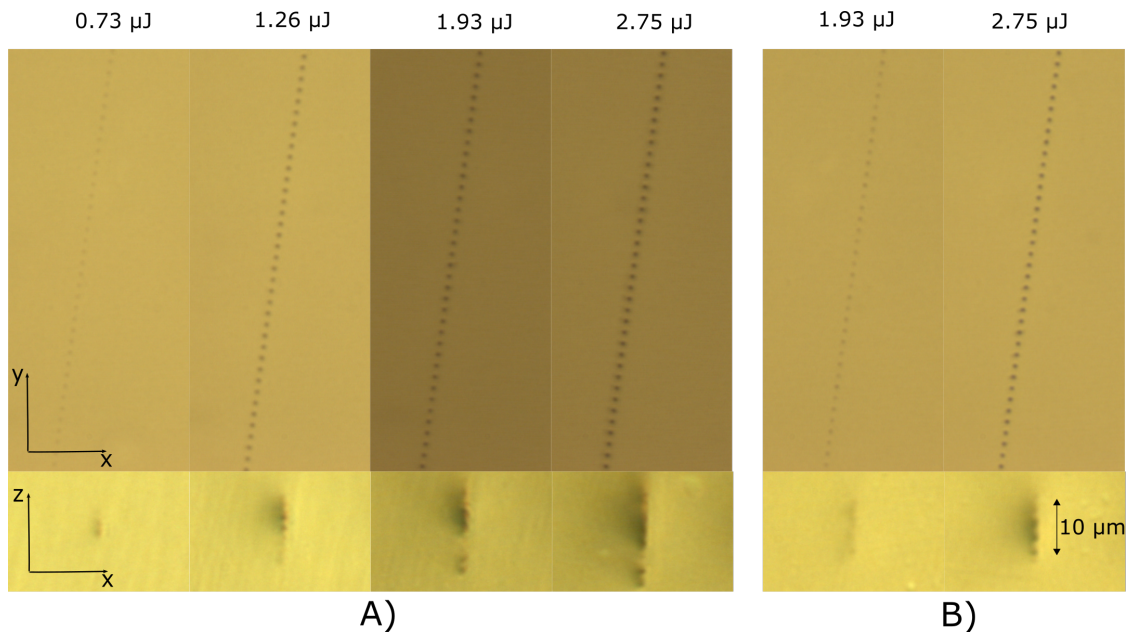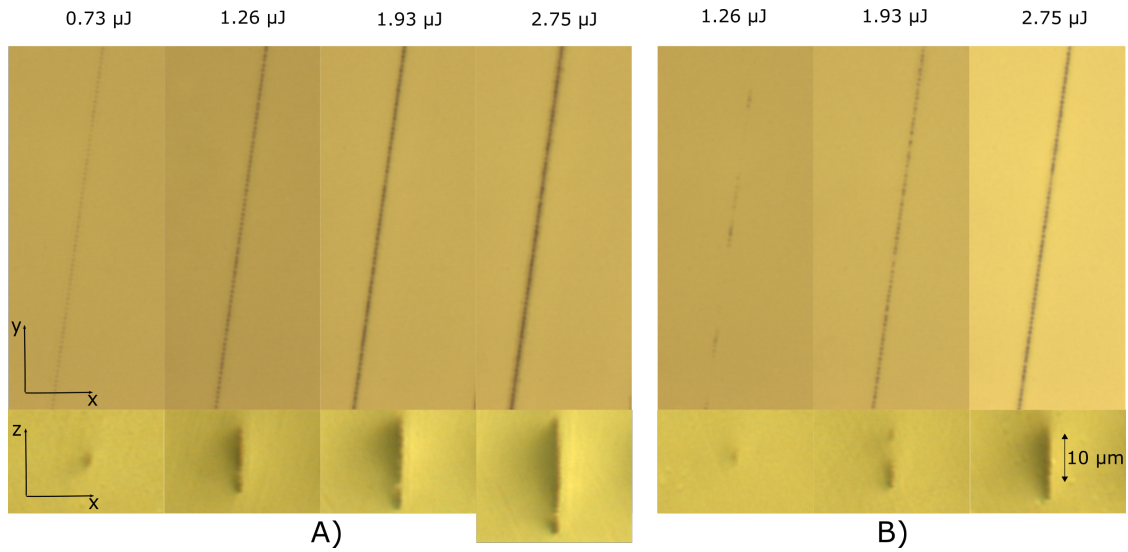
Figure 4.2: Microscopic images of line defects in the first sample as lines along the sample with corresponding writing energy above and cross-section below. A) shows structures made in depth of 30 µm and B) shows structures at 60 µm. All defects made with writing speed 20 mm/s at 10 kHz repetition rate.

Figure 4.2 shows lines of defects, each formed by single-pulse irradiation with the 2.1 µm laser. Defects were also induced with a pulse energy of 0.38 µJ, however, they were not detectable with optical microscopy. Therefore, it was assumed that this specific pulse energy setting was below the modification threshold of the material. The point defects in Figure 4.2 were produced with a repetition rate of 10 kHz and writing speed 20 mm/s thus, the distance between each point is 2.0 µm. Since it is desirable to have continuous lines when writing waveguides, this distance between each pulse is too large. This combined with the used powers and repetition rates represents a clear sign of discontinuous cross-sections with increasing energy. The inscription depths in air of the structures in Figures 4.2A) and 4.2B) were 30 µm and 60 µm, respectively. Although a top view of the lines suggest that they were not significantly affected by the change in depth, the cross-sections make evident the impact of this change. With this writing speed (20 mm/s) no defects were optically detectable for processing energies of 0.38, 0.73 or 1.26 µJ at the depth of 60 µm.

Figure 4.3 shows similar pattern as Figure 4.2, formed with the same writing parameters apart from the writing speed, which was here 10 mm/s.

At this writing speed, the defects form, as expected, lines that are more continuous since the distance between each point defect is 1.0 µm compared to 2.0 in Figure 4.2. However, with sufficiently high lens magnification, it is still possible to see the

Figure 4.3: Microscopic images of line defects in the first sample as lines along the sample with corresponding writing energy above and cross-section below. A) shows structures made in depth of 30 µm and B) shows structures at 60 µm. All defects made with writing speed 10 mm/s at 10 kHz repetition rate.
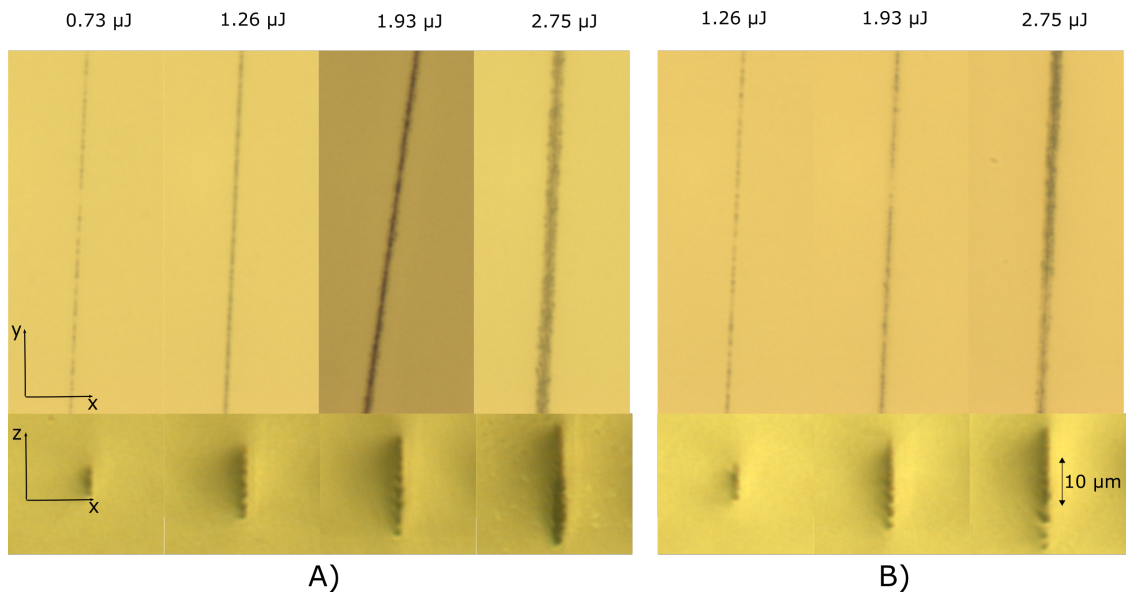
Figure 4.4: Microscopic images of line defects in the first sample as lines along the sample with corresponding writing energy above and cross-section below. A) shows structures made in depth of 30 µm and B) shows structures at 60 µm. All defects made with writing speed 6 mm/s at 10 kHz repetition rate.

separation of each point in the low energies. These writing parameters also results in more symmetric cross-sections, at least at the low energy regime adopted here. The

higher pulse energies, at 2.75 µJ, the lines appear less sharp and more blurred at the edges, both from top view and the cross-sections. At this writing speed setting, is was possible to obtain lines at a depth of 60 µm by using 1.26 µJ pulse energy for writing. This observation is attributed to the lower temporal distance between pulses, which leads to the deposition of more energy to a given volume. Notably, the blurry edges of the defect lines appear to be more pronounced in Figure 4.4, where the writing speed used is even lower.

At a writing speed and repetition rate of 6 mm/s 10 kHz, respectively, the distance of successive pulse defect becomes 0.6 µm. With these writing parameters, the size of the waveguide cross-section increases unpredictably with increasing energy. However, low pulse energies enable the encoding of lines with shapes that seem more symmetric and predictable, both from a top view and a cross-sectional view. It is also demonstrated that writing with low pulse energies results in less pronounced shape variations with inscription depth.

This sample showed indications that low energies at low writing speed gives more predictable defects in terms of shapes as well as continuity of the lines from above. These are desirable features for waveguide writing and was investigated more in sample 2.

Based on these indications that low pulse energies and writing speeds are favorable conditions for writing waveguides in terms of predictability of defect shapes and line continuity, these parameters were further studied in sample 2. Since changing the repetition rate can ensure a more stable laser system than changing other laser operating parameters, it was opted to choose an average power and writing speed of the same order as in sample 1. However, this choice inevitably results in different distances between successive defect points and pulse energies. The parameters used for writing waveguides in sample 2 are provided in section 3.1.

In Figure 4.5, writing speeds are compared for different depths, with the same writing energy, in sample 2. The figure shows the top views of the lines and indicates that the writing speed has a definite impact on the structures, similar to sample 1. At shallow depths, on the order of 30 µm below the surface, adopting low writing speeds results in the formation of slightly unpredictable structures as the lines are not perfectly uniform and have a point-like shape. These points do not correspond to pulses (as in Figure 4.2) since the difference between them is changing, and speeds like 16 mm/s at the same depth and energy show a continuous line. At larger depths, these same lines become more uneven and blurry on the sides. This further confirms the observations in the previous sample that lower speeds make the lines more uneven and give more blurry edges. This gives reason to believe that lines made with low speeds will provide more unpredictable shapes if written close together. As repeatability is a key factor for technical applications like waveguiding, slow writing speeds are ruled out. As mentioned, the line written with a speed of 16 mm/s seems to be the fastest written
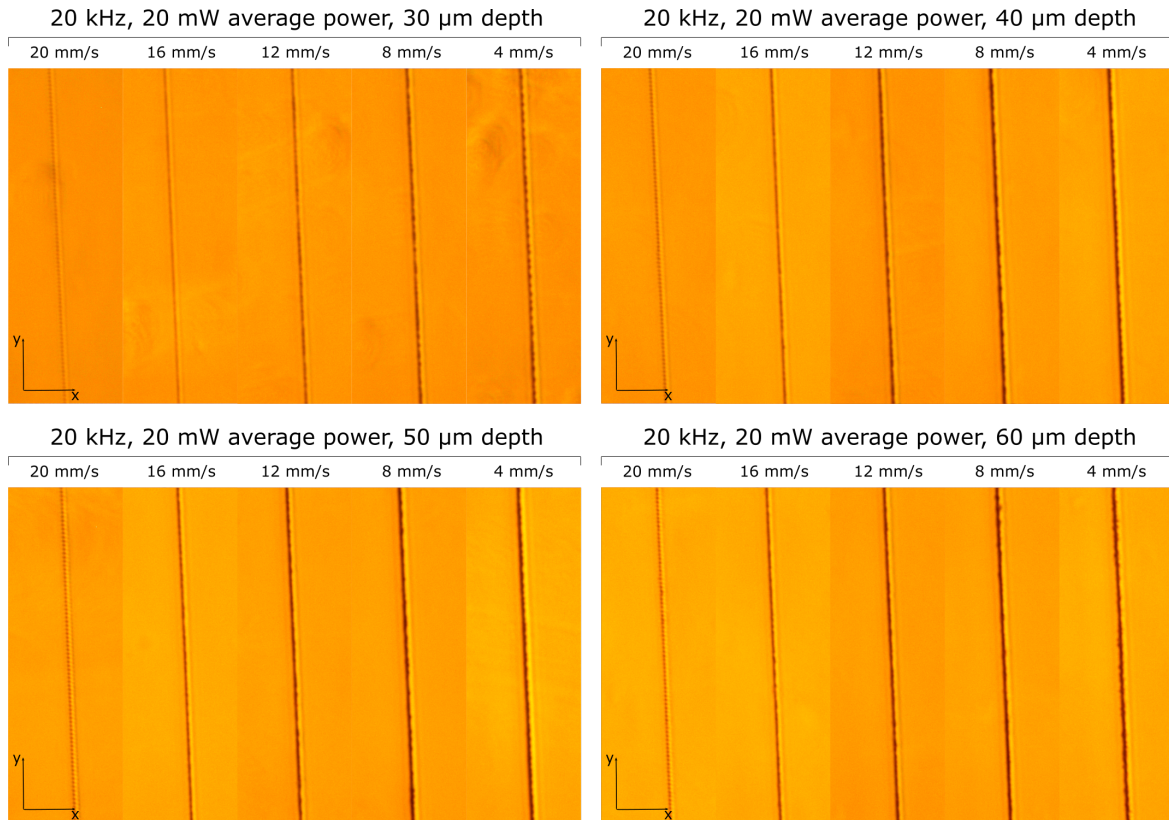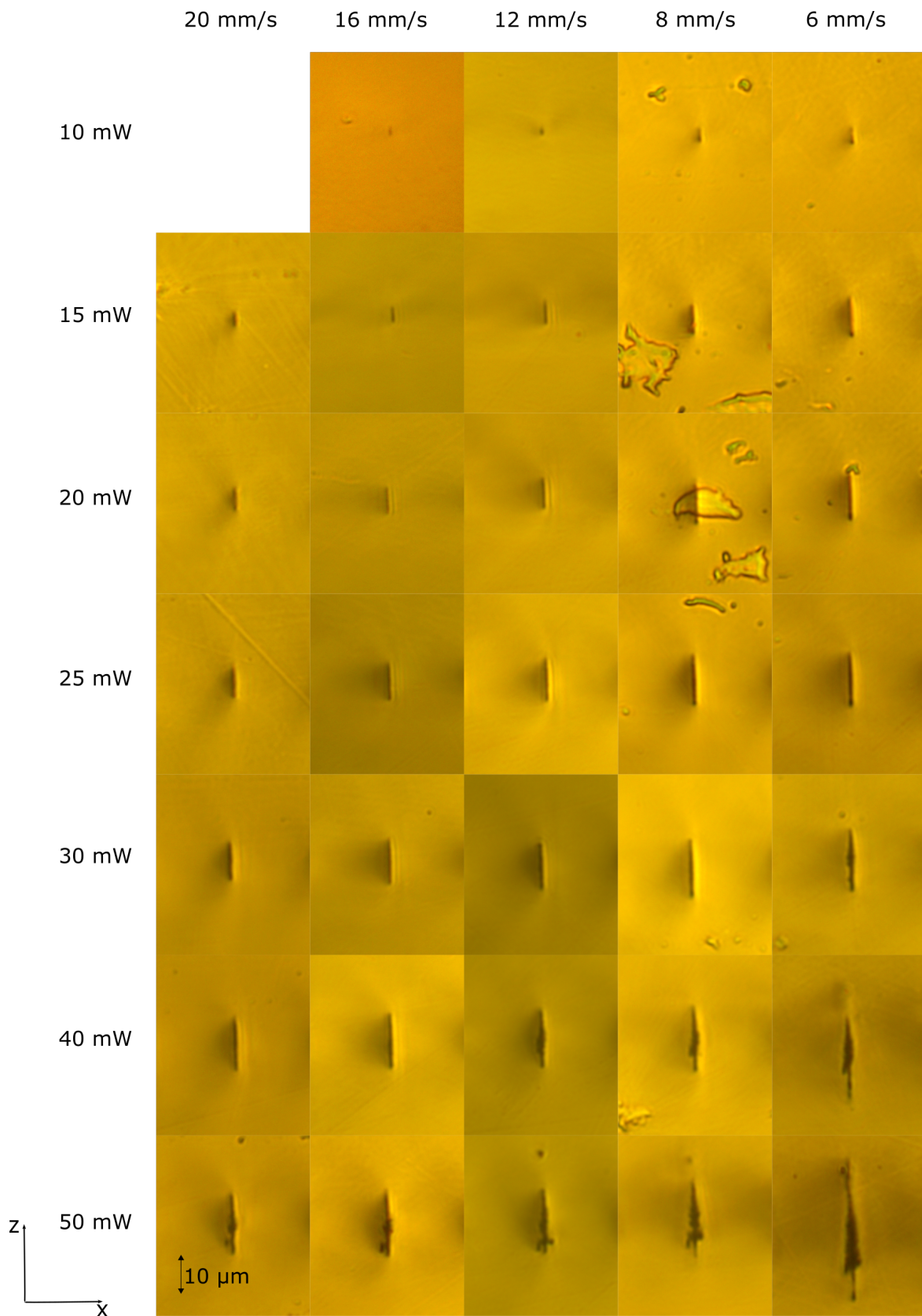
Figure 4.5: Microscopic images of line defects in sample 2, with the corresponding writing speed and depth. The lines are grouped together by depth with the only changing variable is the writing speed. All line defects represented in this figure were made with 20 kHz repetition rate and 20 mW average power.

line that looks continuous and does seem to have a uniform structure as well as not change too much depending on the depth. Compared to sample 1, the images of the cross-sections of several line defects in Figure 4.6reveal sharper and more consistent structures. The corresponding sizes are summarized in table 2. By changing the repetition rate, there is a clear improvement in the cross-sections as they look more uniform in their shape.

All cross-sections shown in Figure 4.6 were written at 40 µm depth in air,using various writing speeds and average powers. The smallest-size defects detected were induced with a 16 mm/s speed and a 10 mW average power, and a clear pattern of increasing structure size with both decreasing writing speed and increasing average power is to be observed and is consistent with sample 1 as well. The approximate dimensions of the cross-sections are summarized in table 2 too.With low writing speeds and high optical powers, the shapes of the defects start to become severely distorted. As for the writing speed, this may be due to the overlapping of pulses in the medium, thus, effectively creating a larger focal volume. The smallest and sharpest structures seem

thus, to be those inscribed with 16 mm/s at average powers below 40 mW (starts to be distorted at 50 mW). To further confirm this observation, images of the cross-sections of the line defects formed at all depths using optical powers of 10, 15, 20, and 25 mW, with a writing speed of 16 mm/s, are summarized in Figure 4.7.

The cross-sections in Figure 4.7 show clear and sharp structures that increase slightly with depth at a considerably low rate, which is regarded as acceptable and thus, assumed not to have a severe impact on the shape of potential waveguides. The size of the structures written with an average laser power of 10 mW is sufficiently small to be considered distinct points, but the ones made with higher optical powers are slightly elongated. For example, the length of structures inscribed with an average laser power of 25 mW at a depth of 60 µm is approximately 10 µm.

Figure 4.6: Microscopic images of line defect cross-sections for each writing speed and average power in sample 2. All defects represented in this figure is at a depth of 40 µm and is written with a repetition rate of 20 kHz.

Table 2: Size (µm) of the defects depicted in Figure 4.6 at the depth of 40 µm. The table is in a matrix form that directly corresponds to the figure.

|	Size (µm)				
	20 mm/s	16 mm/s	12 mm/s	8 mm/s	6 mm/s
10 mW		<2	<2	3.5	4
15 mW	3.5	4	6	7.5	10
20 mW	6	6.5	8	10	12
25 mW	7.5	10	11.5	13	14
30 mW	9.5	11.5	12	15	16.5
40 mW	13.5	14	15	17	22
50 mW	15.5	17.5	17	19.5	37
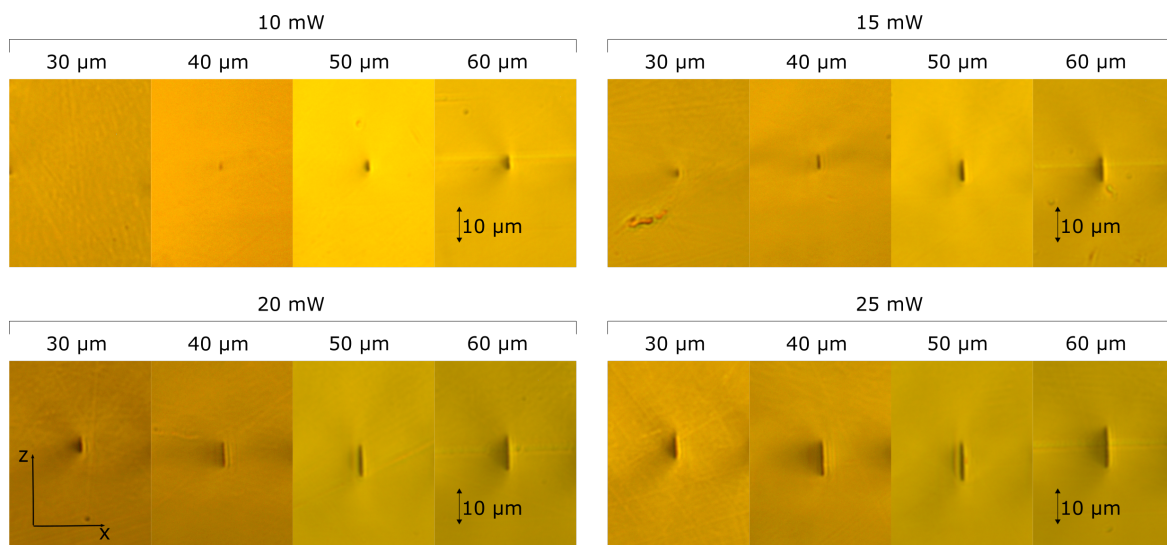
Figure 4.7: Cross-sections of line defects for each depth at writing speed 16 mm/s, repetition rate 20 kHz and for the powers 10, 15, 20 and 25 mW. The four groupings compare power at different depths.

4.3   Waveguides

Based on the observations of the line defects obtained from the first two samples, waveguides were written at a speed of 16 mm/s and a repetition rate of 20 kHz. The writing was performed with different average powers of 7, 10, 15, and 20 mW at a 60 µm depth in the air. As per earlier investigations, the 7 mW optical power[c], (i.e., 0.35 µJ) was expected to be below the power threshold for inducing modifications in the material. Several waveguides were formed, with diameters ranging from 20 to 60 µm, and various distances between each waveguide element (DBE). Figure 4.8 displays images of cross-sections of waveguides formed using the four optical powers aforementioned. Their diameter was 60 µm, and the DBE was 2 µm
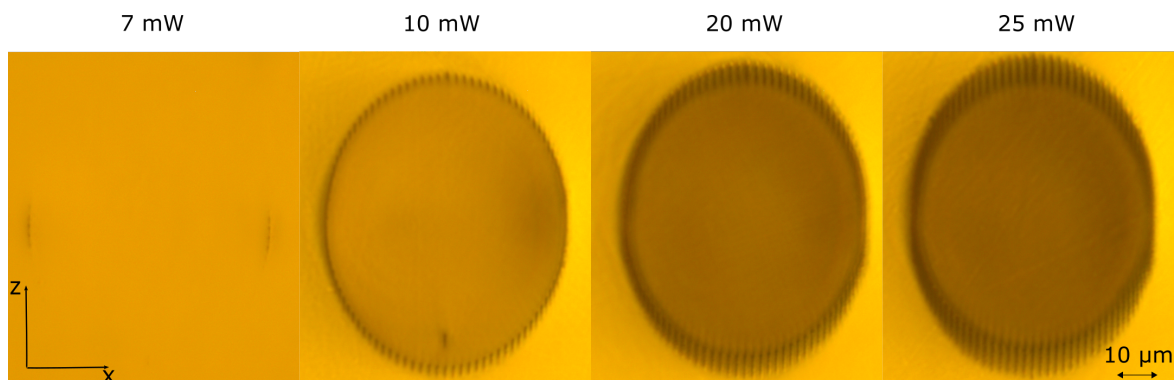

Figure 4.8: Waveguides written with 20 kHz repetition rate with a diameter of 60 µm at average powers 7, 10, 15 and 20 mW. The DBE in the waveguides is 2 µm.

It is also evident that the 7 mW average writing power was below the threshold since defects were encoded only in the horizontal antipodal points of the waveguide cross-section due to the spatial overlapping of the elements in these regions. Some of the first waveguides written in this sample experienced one misplaced defect line due to an error in the writing script. This misplaced element is noticeable inside the waveguide formed with 10 mW optical power displayed in Figure 4.8.

4.3.1   Size and shape

The misplaced defect element is also observable in Figure 4.9, which shows cross-sections of waveguides formed with 10 mW average power with 4, 3 and 2 m DBE. Figure 4.9 displays all the waveguides above the writing threshold with 30 µm diameter and corresponding average writing power and DBE. It is clear that with lower DBE and higher power, the cladding (i.e. the volume of laser-induced modifications) of the structures becomes thicker and more pronounced, as expected.

---

[c]The following sections uses average writing power instead of pulse energy as a processing parameter. This was the varying parameter in the process and, thus, gives more accuracy.
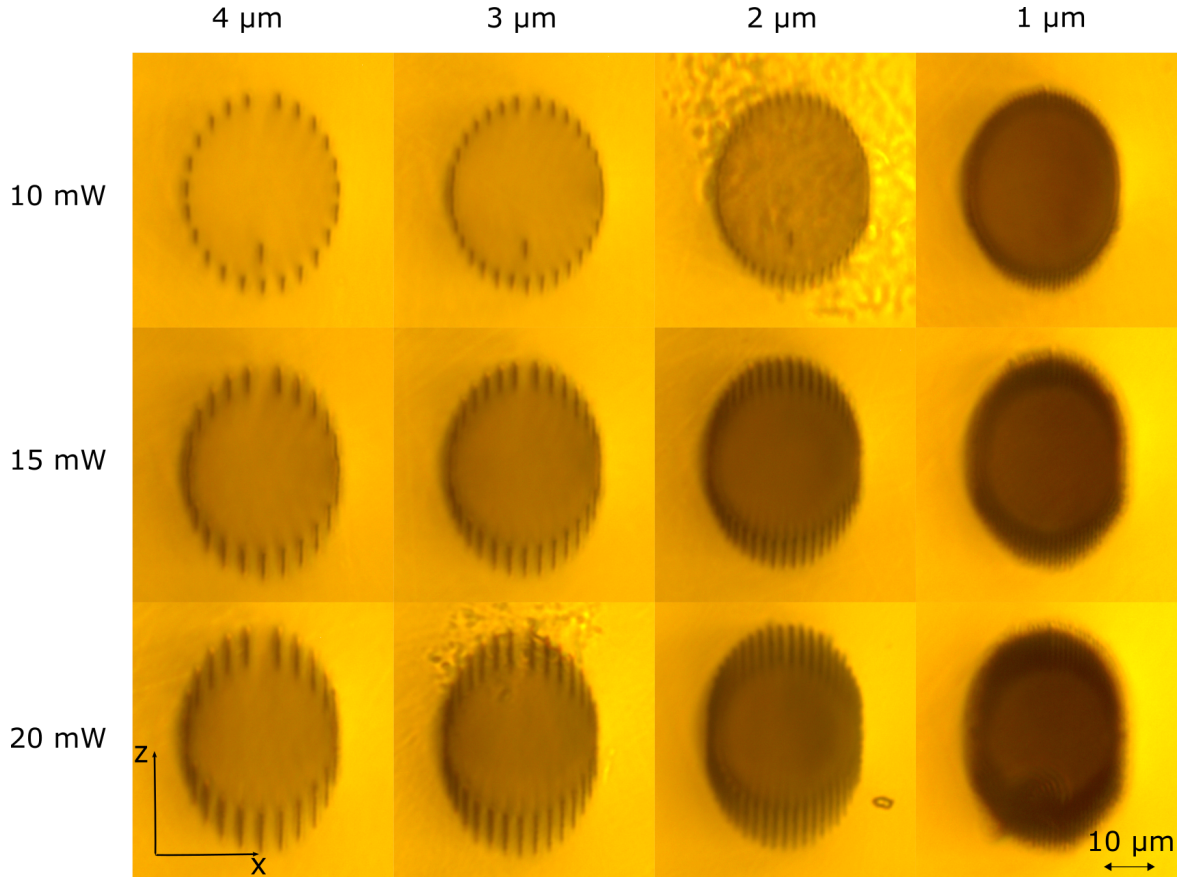
Figure 4.9: All waveguides written above modification threshold with diameter of 30 µm, with their corresponding DBE and average writing power.

The waveguide corresponding to the lowest optical power shows a small core eccentricity. With increasing optical power, hence with increasing defect size, as stated in section 4.2, the core eccentricity decreases. The high eccentricity for the waveguides form with low optical power might be due to the refractive index value assumed for ZnS in the script when writing the structures. This value was 2.2, but in reality, it might be slightly higher. It is also worth noting that DBE is defined as the distance from center to center of two successive defects, not their horizontal separation. Therefore, there is at higher powers an extensive overlapping of neighboring defects in the horizontal antipodal points. Also, one needs to consider that different number of elements that form a waveguide is different for each structure, depending on the waveguide diameter and the DBE chosen. Therefore, the waveguides having 4 µm and 3 µm distances between their constituent elements have a slightly wider gap between two successive defects on their tops.

To visualize the effective waveguide depth, the surface line of the sample is also displayed in the images in Figure 4.10, which shows that the centers of all waveguides
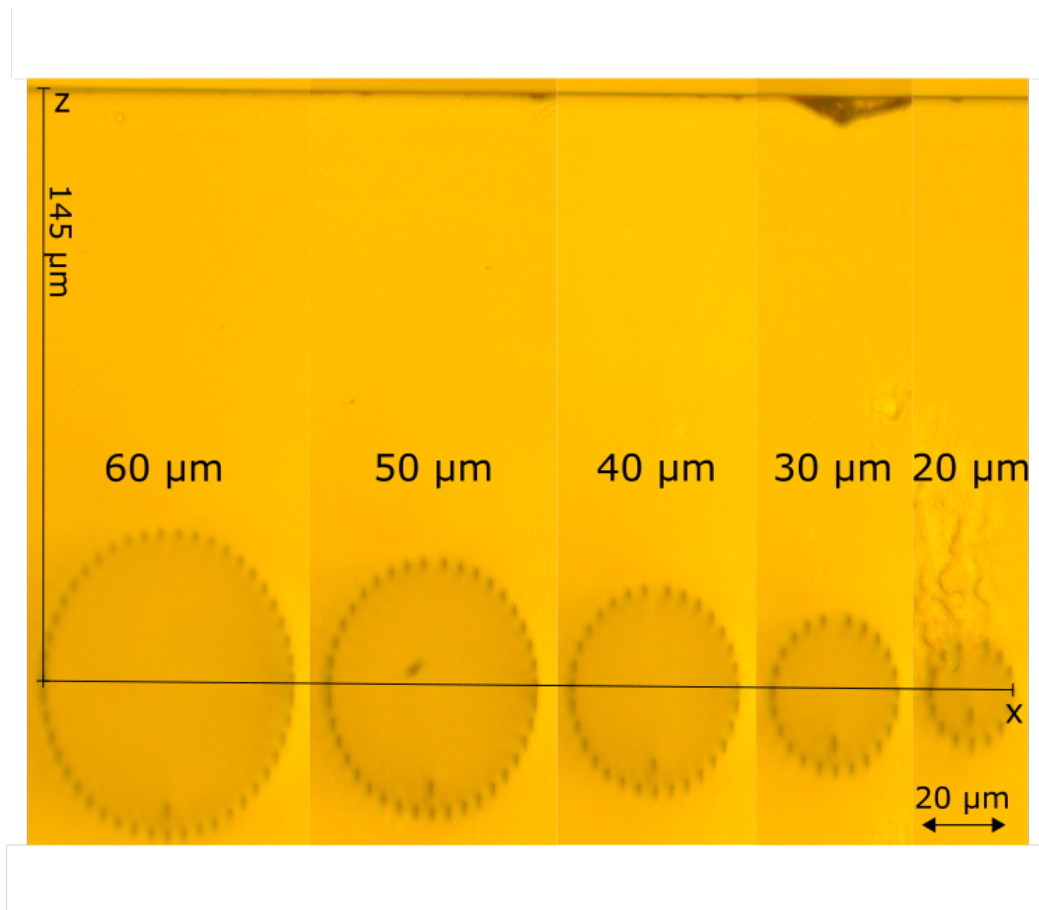
Figure 4.10: Cross-section of waveguides written with average power 10 mW and DBE 4 µm, in order of decreasing diameter. Surface line of the sample is included to show depth.

cross-sections lie clearly at the same depth of approximately 145 µm. Since the eccentricity of the core seems to be changing with different parameters, some diameter measurements of 50 µm waveguides are shown in Figure 4.11. The corresponding waveguides were inscribed using various average writing powers and at 4 µm and 2 µm distances between the defect elements. The outer ellipse included in the images that is fitted to each waveguide cross-section, represents the writing diameter, and is the same for all waveguides. The inner ellipse is fitted to the core of each waveguide. Here, it is clear that the effective waveguide core, which is enclosed by the cladding, decreases with increasing writing power and decreasing DBE. The change observed is the largest at the vertical axis because the encoded defects increase in size (i.e., length) with increasing optical power, as studied in section 4.2. However, a slight change is also observable in the horizontal axis most likely originating from the overlapping of the elements. Therefore, it becomes more pronounced for smaller waveguides as the decreasing percentage relative to the waveguide diameter will be higher. All recorded waveguides with their cross-sections and their top views are shown in appendix A.

### 4.3.2   Numerical aperture, Δn and mode confinement

The setup described in section 3.2.2 allows viewing the waveguide cross-sections while a laser beam is coupled to them at low intensity. By implementing this setup, it is easy to determine if the structures guide light at all and thereby confirm that a negative refractive index change Δ n was realized in the material domains exposed to laser irradiation, as desired. It also provides an idea of the mode confinement in the waveguide, as shown in the IR transmission microscopy images of laser coupled into the waveguides in Figure 4.12, which display waveguide cross-sections with different diameters. They correspond to all waveguides fabricated with an optical power of 10 mW and have a 4 µm DBE. The conclusion drawn from these images is that the waveguides with the largest diameters of 40, 50, and 60 µm show multi-mode confinement. However, determining the modality of waveguides with diameters of 20 and 30 µm is more difficult because these pictures are the only evidence supporting their single-mode confinement. Since single-mode waveguides are advantageous for mitigating thermal lensing[61], it was deemed necessary to further study the modal properties of the waveguides with these two diameters.

However, estimation of the NA for the waveguides with the smaller diameter of 20 µm using the setup described in section 3.2.3 proved difficult because, as shown in Figure 4.13, all the intensity profile images acquired exhibited extensive diffraction rings around the beam output.

This suggests that a part of the beam launched into the waveguide leaks from it. Another possible reason would be that the intensity profile is distorted due to the diffraction and scattering of uncoupled light propagating through the medium. The formation of the same type of rings at the waveguide output was observed by Streltsov
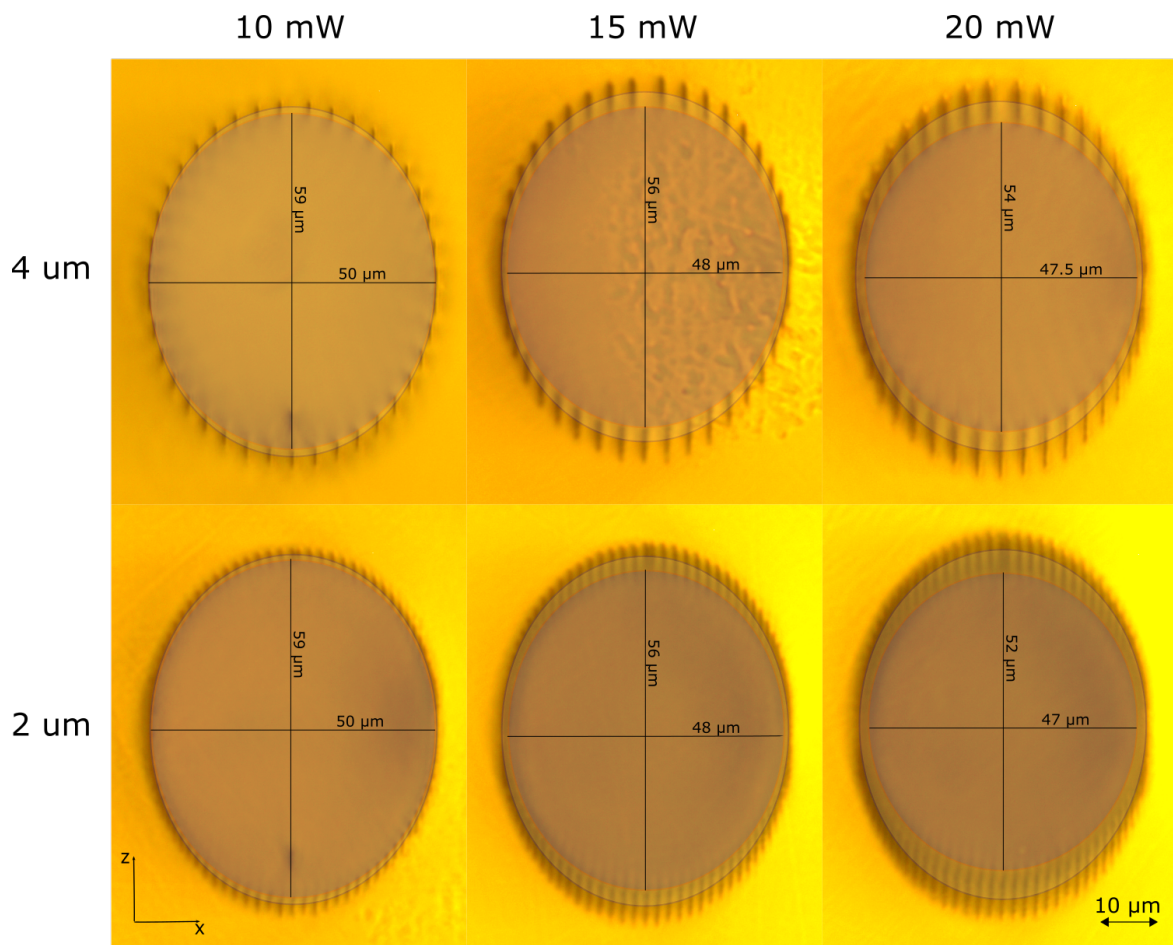
Figure 4.11: Change of core radius in both axis dependant on average writing power and DBE. The figure shows 50 µm waveguides as powers 10, 15, 20 mW with 2 and 4 µm DBE.
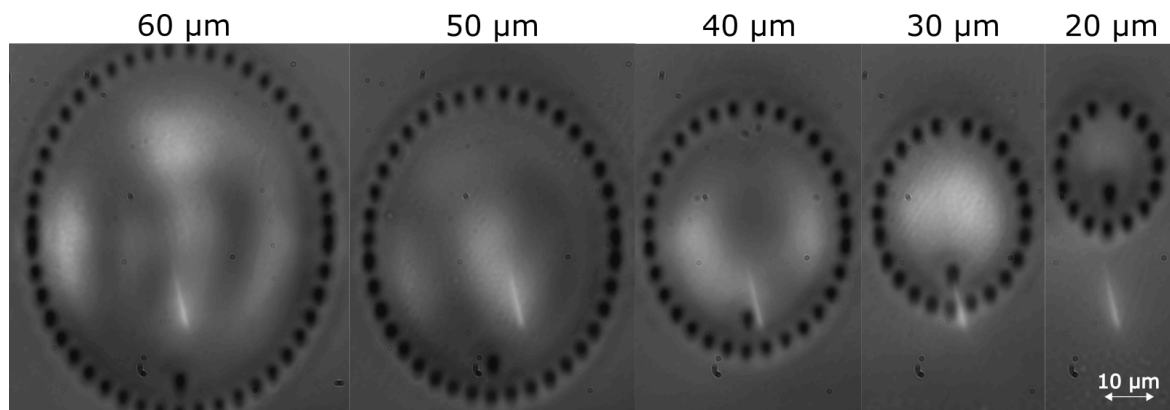

Figure 4.12: IR transmission microscopy of laser coupled into the waveguides made with average power 10 mW with 4 µm DBE. Focusing objective is of magnification 100x.

(a) Intensity profile.
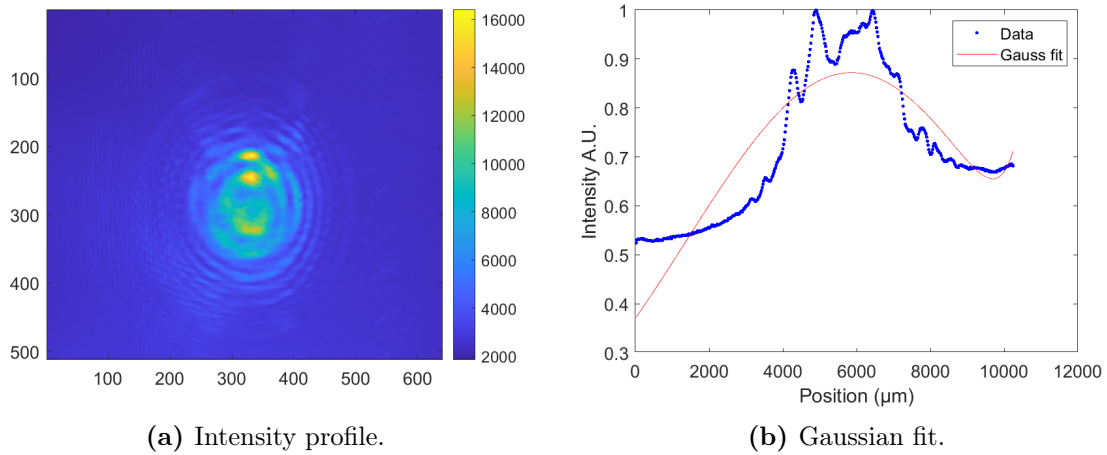
(b) Gaussian fit.
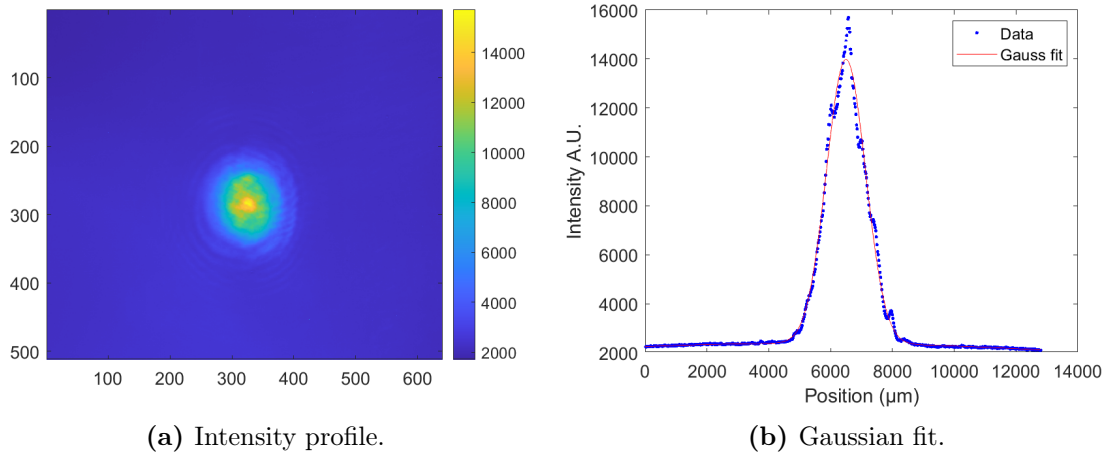
Figure 4.13: Intensity profile of output beam from waveguide of 20 µm diameter. a) shows the intensity profile, while b) shows the attempted Gaussian fit.

[56] in their studies of waveguides with a 25 µm core inscribed in CaF_2. However, the 30 µm wide waveguides had a different behavior since the laser light was coupled and guided through the structure without any leakage. Therefore, a proper intensity profile of the beam is obtainable. The intensity profiles from a waveguide with a 30 µm diameter, recorded at two different distances from the waveguide, are shown in Figure 4.14 and 4.15, together with the corresponding Gaussian fits. The waveguide was inscribed with an average optical power of 15 mW and had a DBE of 4 µm.

(a) Intensity profile.
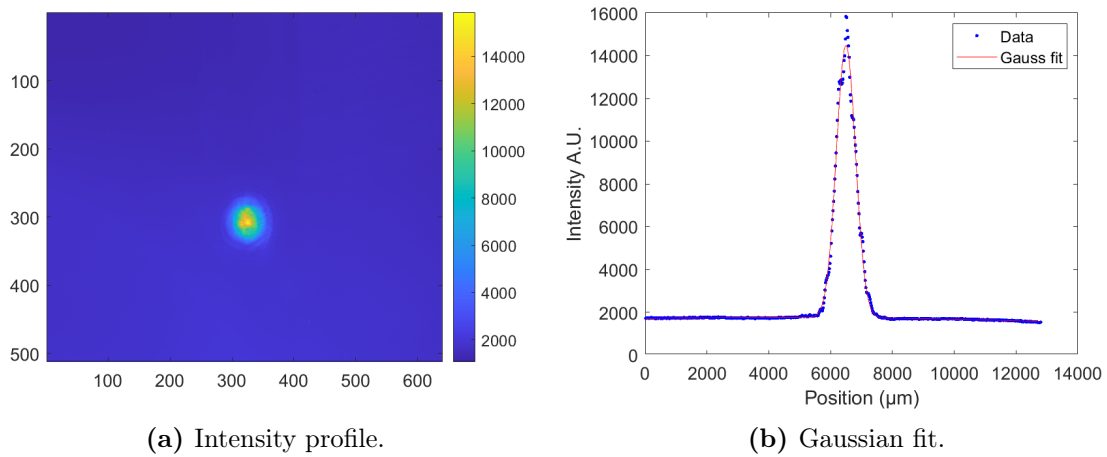
(b) Gaussian fit.

Figure 4.14: Horizontal intensity profile of output beam from waveguide of 30 µm diameter. a) shows the intensity profile, while b) shows the corresponding Gaussian fit. This is the first measurement closest to the waveguide.

Figure 4.15 shows the same type of measurement as in Figure 4.14, only after five steps. Hence, the intensity profile displayed was recorded at a distance of 20 cm from

(a) Intensity profile.

(b) Gaussian fit.

Figure 4.15: Horizontal intensity profile of output beam from waveguide of 30 µm diameter. a) shows the intensity profile, while b) shows the corresponding Gaussian fit. This is the last measurement 20 cm from the waveguide.

the waveguide, indicating a definite increase in the beam size compared to Figure 4.14. To estimate the expanded beam size, all the five steps and their corresponding beam size estimation from the Gaussian fit are plotted in Figure 4.16. As the measuring sensor is placed slightly inside the camera, it was assumed that all the measurements were performed in the far-field far enough from the beam waist and that the distances listed are relative to the measurements. Therefore, the beam is assumed to be linearly diverging.

From the slope of the expanding beam in Figure 4.16, a horizontal numerical aperture for the waveguide of 0.035 was estimated from eq. 7. If the refractive index of ZnS is assumed to be n=2.27[64], by using eq. 8 the refractive index in the defect region in the horizontal antipodal points can be calculated to be $n_{\mathrm{clad}} = 2.2697$. yielding a refractive index change of $\Delta n = 2.7 \cdot 10^{-4}$. The NA values estimated for all 30 µm waveguides formed with average powers of 15 and 20 mW are listed in table 3. The corresponding Δn estimations are plotted in Figure 4.17. Since the waveguide structures seem to have an asymmetric cross-section, both the horizontal and the vertical estimations are included.

59
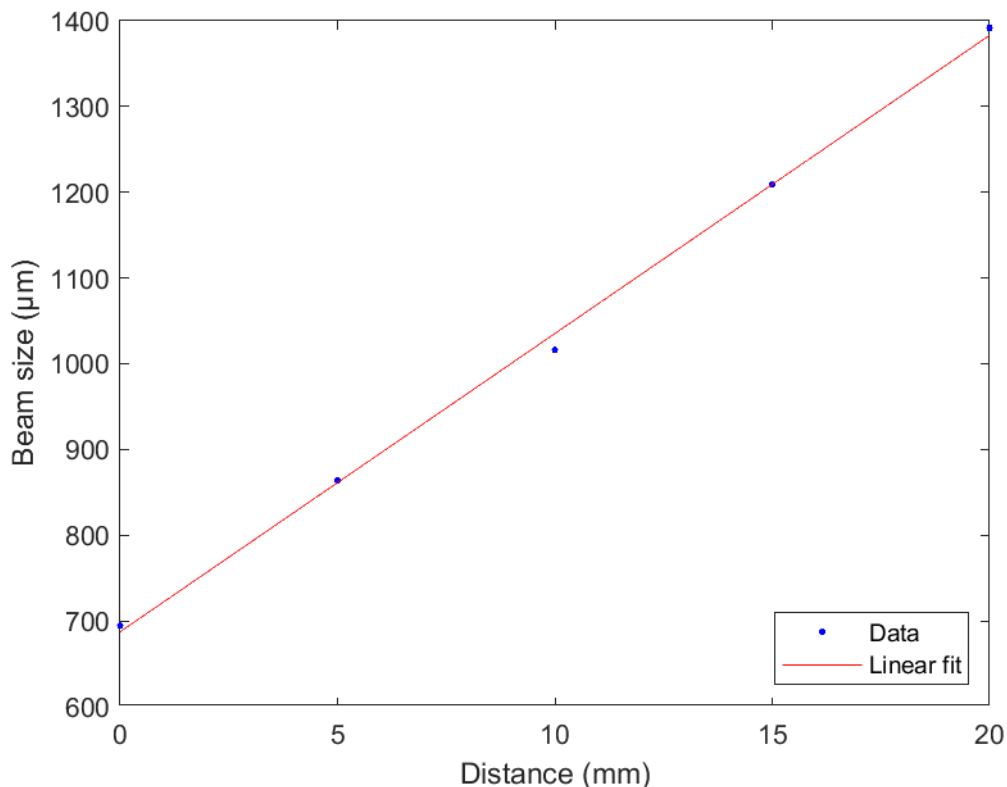
Figure 4.16: Increasing beam size, in the horizontal direction, as it exits the 30 µm waveguide that was written with 15 mW average power with DBE of 4 µm.

Table 3: Estimated numerical aperture for all 30 µm waveguides written with average power 15 and 20 mW with corresponding DBE. Table shows both vertical and horizontal NA due to asymmetry in the cross-section.

	Vertical NA				Horizontal NA			
	4 µm	3 µm	2 µm	1 µm	4 µm	3 µm	2 µm	1 µm
15 mW	0.032	0.029	0.032	0.037	0.035	0.035	0.038	0.028
20 mW	0.031	0.032	0.034	0.037	0.036	0.033	0.036	0.041

Almost every waveguide measured has a larger NA in the horizontal direction compared to the vertical, and thus a higher change in the refractive index. Based on the information obtained during these measurements, it is plausible to assume that this difference is due to the overlapping line defects in the horizontal antipodal points. From table 3, one can realize that the vertical NA increases slightly with decreasing DBE. As shown in Figure 4.11 the vertical diameter decreases slightly with decreasing DBE, but since NA initially is independent of core radius, this is most likely not

60

(a) Δn vertical.   **(b)** Δn horizontal.
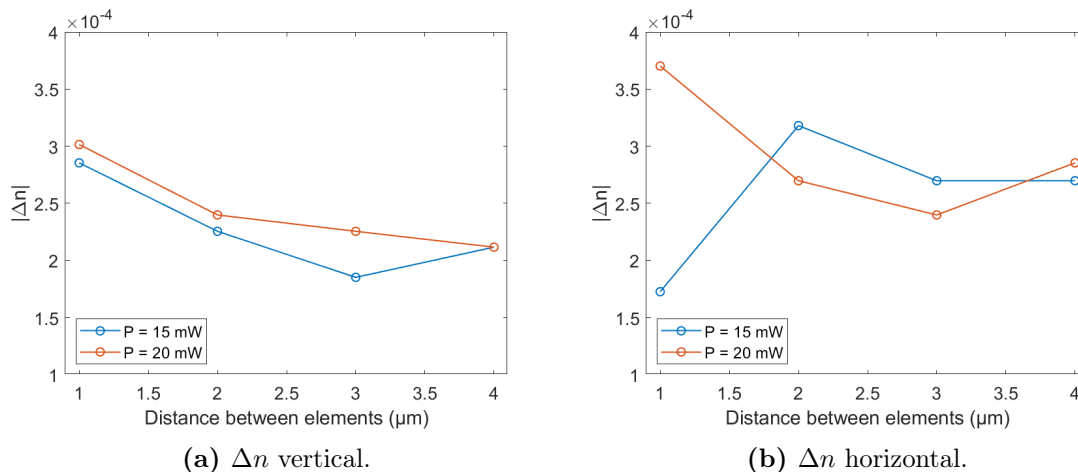
Figure 4.17: Δn estimations for all 30 µm waveguides written with 15 and 20 mW average power, both in vertical (a) and horizontal (b) direction.

the reason. Due to the smaller DBE this might increase the effective refractive index change in the cladding volume even though each defect should have an unchanged index regardless of the DBE. This dependency is seen more clearly in the refractive index changes in Figure 4.17. It is also seen that this dependency is more uniform in the vertical direction than in the horizontal direction, which might also be a result of the overlapping defects. Drawing conclusions from this would require studying structures in a broader range of DBE and optical powers.

From eq. 19 and the NA values in table 3, all the corresponding $V numbers$ are estimated and presented in table 4

Table 4: Estimated $V number$ for all 30 µm waveguides written with average power 15 and 20 mW with corresponding DBE. Table shows both vertical and horizontal $V numbers$ due to asymmetry in the cross-section.

	Vertical V				Horizontal V			
	4 µm	3 µm	2 µm	1 µm	4 µm	3 µm	2 µm	1 µm
15 mW	1.95	1.76	1.95	2.25	2.13	2.13	2.31	1.70
20 mW	1.88	1.95	2.07	2.25	2.19	2.01	2.19	2.49

Thus, if we assume step-index waveguide structure almost all 30 µm waveguides measured exhibits single-mode confinement with $V number$ below 2.405[65]. By using eq. 20, we get that all the waveguides' mode radius are between approximately 16.1 µm and 22.5 µm. These values are acceptable as they do not extend too far outside the core radius of 15 µm. Too large a mode radius will make it difficult to create bent structures as the mode gets more and more non-Gaussian with increasing mode radius[56].

This will also make coupling to waveguides that support quasi-Gaussian mode more difficult.

4.3.3   Loss measurements

Propagation losses were measured in all the 30 µm diameter waveguides depicted in Figure 4.9, using the setup described in section 3.2.4. To satisfactorily evaluate the propagation loss level, the coupling losses were estimated using eq. 21. The angle offset was, in this case, measured to be $\Delta\theta \sim 0.7°$, and the mode radius of the fiber laser used in the setup was ~ 5.2 µm, resulting in a coupling efficiency of $\eta = 0.918$. After calculating the Fresnel transmission to be $T_{FR} \sim 0.738$ from eq. 15, the losses in decibels per cm were subsequently estimated from eq. 13 for a waveguide with a length $L = 0.6$ cm. Figure 4.18 shows plots of the calculated loss values in decibels per centimeter as a function of writing power and DBE.

(a) Loss dependency on writing power.

(b) Loss dependency on DBE.
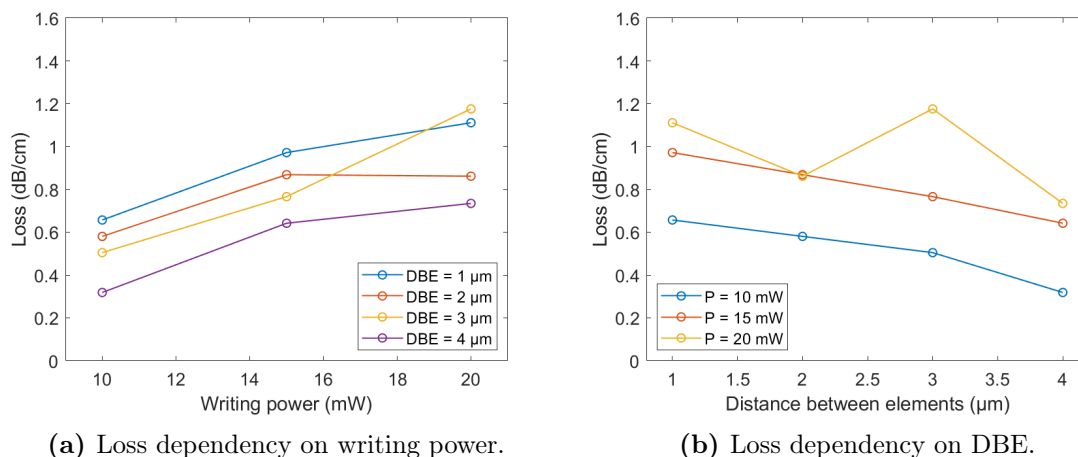
Figure 4.18: Loss measurements and the dependency on the writing power (a) and distance between each defect element (b).

In these plots, it becomes clear that the waveguide loss is indeed dependent on both the writing power and the DBE. Thus, the losses increase with increasing writing power and decreasing DBE, with the highest value measured to be approximately 1.18 dB/cm for 20 mW writing power and 3 µm DBE. The lowest loss value derived was 0.32 dB/cm and, as expected, corresponded to the waveguide written with a 10 mW optical power and a DBE of 4 µm.

Since the equation used for estimating the coupling losses refers to calculating losses between spliced fibers at the coupling area, it does not provide an accurate loss value but can only yield a rough qualitative estimate. These results suggest that a lower distance between elements introduces higher scattering loss in the core-periphery. This last observation may also be relevant to waveguides written with higher optical powers

since their core structures seem to become smaller and more asymmetric and unpredictable in shape.

4.4   Results in Cr:ZnS

The doped sample studied in this thesis was originally the first femtosecond processed single-mode depressed cladding waveguide laser reported in monocrystalline Cr:ZnS in 2019[8]. This sample incorporated five laser-written waveguides with different core diameters. In all five waveguides, the DBE was set to 3 µm, and their core diameters had been adjusted by changing the number of inscribed elements. The waveguide with the smallest core had been defined by 42 trakcs, and is is shown in Figure 2.10. The other four were defined by 44, 46, 48 and 50 tracks and their corresponding diameters were 54, 57, 60 and 63 µm, respectively. The 50 µm waveguide then yielded a slope efficiency of 11% with an average power of 150 mW at 2272 nm wavelength. Three of these waveguides were now processed with ARM on the facets as shown in Figure 4.19.
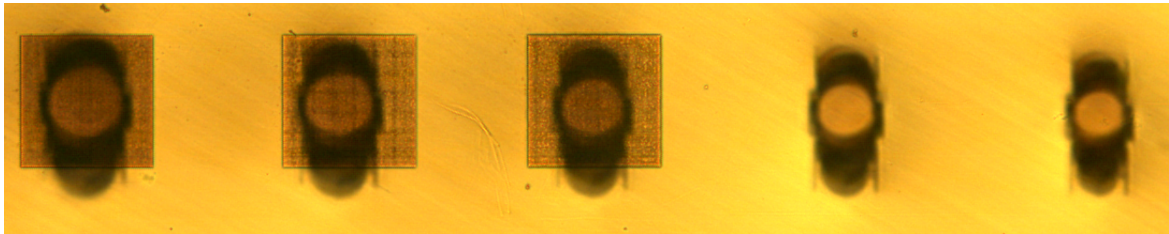

Figure 4.19: All five waveguides originally studied[8]. Three of them have been covered with ARMs on the facets, to investigate the possibility of mitigating reflection[d].

As can be seen, these waveguides have different shapes from the ones in the undoped ZnS samples, which were written with a laser emitting at 2.1 µm. This difference is noticeable in Figure 4.20A, which displays an image of a Cr:ZnS waveguide cross-section obtained with higher lens magnification. Although defects in this structure exhibit more elongated cross-sections than their counterparts in ZnS, they are still uniform in the horizontal direction. This uniformity was not evident in the elongated cross-sections observed in Figure 4.66, where once the defects became elongated, they turned nonuniform and unpredictable in shape. It is worth noting that the structures in Figure 4.6, were inscribed with higher optical powers or lower writing speeds. From table 2, it can be seen that the longest defect measured in sample 2 was 37 µm. It was formed using the highest optical power and lowest writing speed setting of those listed and had a severely distorted shape. To compare defects in sample 2, displayed in Figure 4.20A), with defects around the Cr:ZnS waveguide core, shown in Figure 4.20A, the lengths of defects in the active waveguide were measured. Defects on top,

---

[d]These waveguides will be addressed by number 1-5 in the order presented in this figure starting from the left.

at the sides, and below the waveguide core were approximately 30 µm 45 µm and 60 µm, respectively. The largest size of these defects was 23 µm longer than the severely distorted ones in sample 2. Richter et al. [42] reported that the length of such structures depends on the wavelength of the laser used for the inscription such that longer wavelengths result in more confined and uniform defects. This observation is consistent with the one made for the shape of the structures in this thesis. However, it is still unconfirmed whether this effect can be attributed exclusively to the inscription wavelength used.
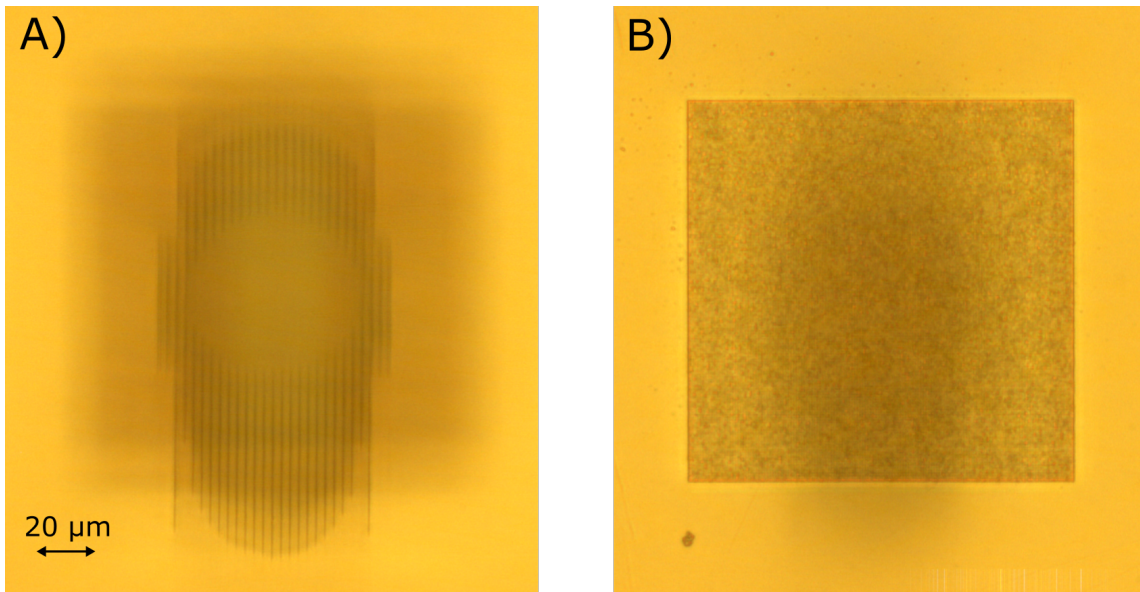

Figure 4.20: Waveguide number 3 in Cr:ZnS. A) show the waveguide facet a few microns beneath the surface of the sample. B) Show the ARM on the surface in front of the waveguide.

The waveguides in the doped sample were written using completely different parameters (i.e., energy, repetition rate, writing speed, and pulse duration) compared to waveguides in the other samples studied.

The intensity profile was estimated in waveguide 5, and is shown in Figure 4.21 along with the associated Gaussian fit, where some disturbances are noticeable in the form of scattering and fluorescence in the material. They might be due to the small space (i.e., on the order of a few micrometers) between the start of the waveguide and the surface of the crystal end facet. This is also apparent in Figure 4.20, where it can be seen that the waveguide does not start until a few microns into the material. This was the case for all waveguides regardless of the presence of ARM. The reason for the background noise might also be due to low coupling efficiency and, thus, absorption of uncoupled light. In the Gaussian fit in Figure 4.21, it is appropriate to assume that the scattering does not dominate the profile, and the waveguide NA can be roughly estimated. The slope of the exiting beam is presented in Figure 4.22.

(a) Intensity profile.
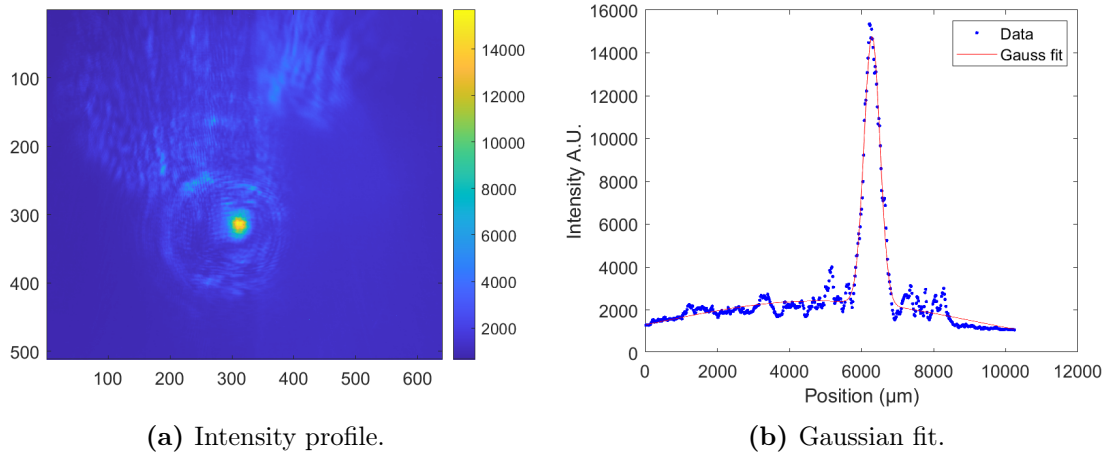
(b) Gaussian fit.

Figure 4.21: Intensity profile of output beam from waveguide 5 with diameter ~ 51 µm. a) shows the intensity profile, while b) shows the associated vertical Gaussian fit.
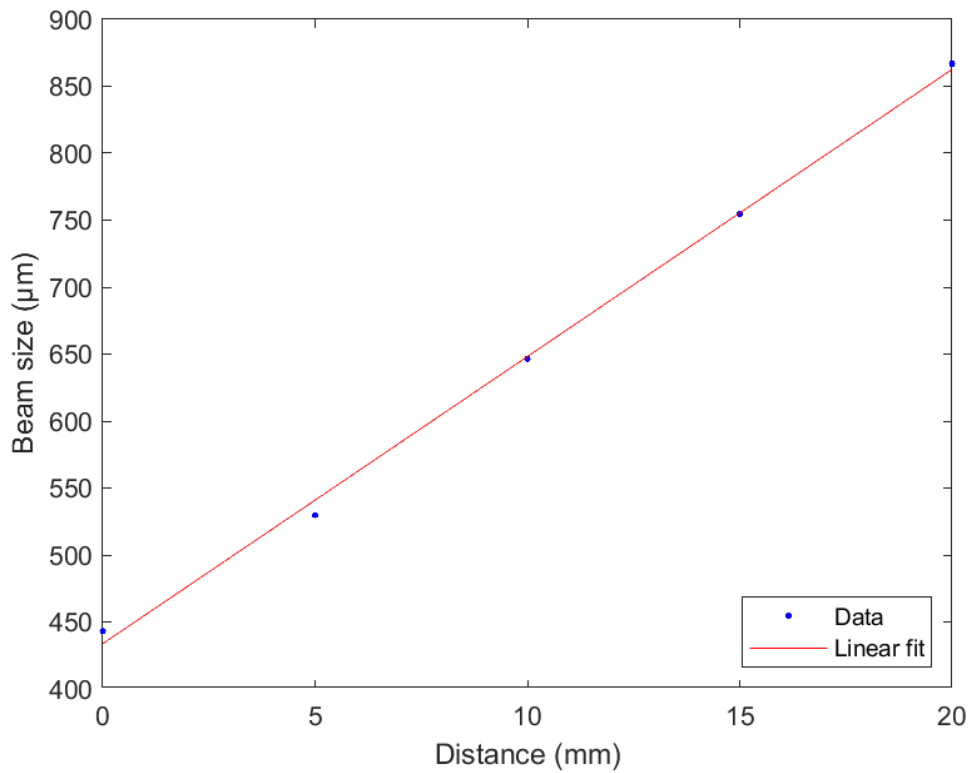
Figure 4.22: Increasing beam size in the vertical direction as it exits waveguide 5.

From the exiting beam and eq. 7, an NA of approximately 0.021 is obtained. By introducing this value in eg. 8, a refractive index change $\Delta n = 9.71 \cdot 10^{-5}$, can be

65
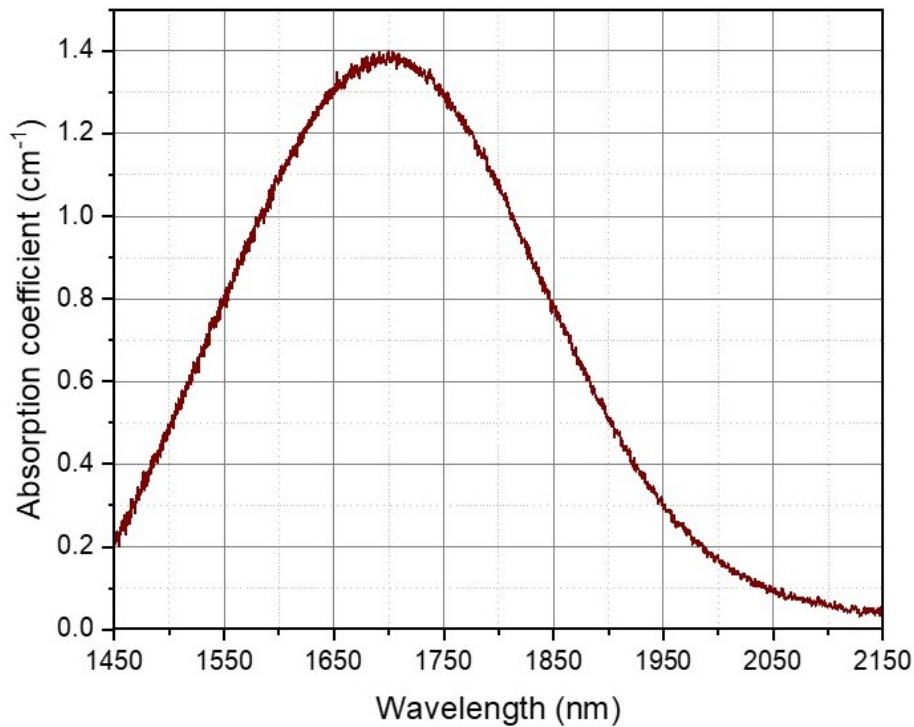
Figure 4.23: Absorption spectrum of the Cr:ZnS sample investigated.

derived. This value is significantly lower than the Δn obtained in the undoped sample. Okhrimchuk and Duarte [51] demonstrated that the Δn in YAG crystals was dependent on the doping concentration in the crystal. Thus, a higher $|\Delta n|$ value was derived in the doped than in the undoped YAG crystal, which was attributed to crystal lattice defects introduced. In this thesis, however, this observation could not be confirmed for the Cr: ZnS and ZnS crystals because the adopted parameters for writing structures in the doped and undoped samples were vastly different. Sorokina et al. [60] stated that Δn increased significantly with pulse duration, which is consistent with the observed difference in Δn between the two samples made with 800 fs and 4-6 ps pulse duration. Even with this small Δn, the $V number$ derived from eg. 19, is estimated to be 2.13. With the core of 51 µm, this Cr:ZnS waveguide exhibits single-mode confinement due to the low refractive index change, as stated in Tolstik et al. [8].

To get an estimation of the losses in the doped waveguides, the absorption spectrum was obtained using a Cary 5G spectrophotometer, and are presented in Figure 4.23. The spectrum exhibits significant absorption in the measuring wavelength of 1.55 µm.

From Figure 4.23, an absorption coefficient of 0.8 cm^{-1} for the wavelength of 1.55 µm is shown. When measuring a doped sample, this absorption becomes of obvious significance and has to be implemented in the loss estimations, by adding the term to eq. 22. From the well known Beer-Lambert law, the transmission coefficient can be

described as $\exp(-\mu \cdot L)$, where μ is the absorption coefficient(i.e., 0.8) and L is the length of the waveguide(i.e., 0.7 cm). This gives a transmission coefficient of ~ 0.57. Propagation losses in the Cr:ZnS waveguides 2, 3, 4, and 5 were estimated from eq. 13, and are presented in table 5. Due to the vast amount of noise in the observed images, as seen in Figure 4.21a, the background were subtracted in the estimations of the propagation loss.

Table 5: Estimated propagation loss for waveguides in the Cr:ZnS sample.[a]

	Loss (dB/cm)
Waveguide 2[b]	5.38
Waveguide 3[b]	5.40
Waveguide 4	5.25
Waveguide 5	5.15
ZnS WG[c]	0.20

[a] Waveguide 1 was left out of the calculations due to the appearance of a small crack that seemed close enough to disrupt the measurements.
[b] ARM at both facets.
[c] Waveguide written in ZnS with 10 mW average power, 3 μm DBE and 50 μm diameter.

It is clear that these estimated losses are significantly high, and are highly affected by poor coupling efficiency. The assumption of an offset angle of 1° and, thus, by including the estimated coupling efficiency $\eta = 0.84$, is a very rough estimate. In reality, the launching of the beam into the waveguide may have an efficiency as low as 0.4. Then the estimations show values between 0.55 and 0.78 dB/cm , which is acceptable values, but this coupling efficiency was not obtained during these experiments. This suggests that the loss estimations performed in the doped Cr:ZnS sample are an upper limit and not the effective propagation loss. To compare with the estimations done in the undoped sample, a 50 μm waveguide were measured and included in table 5. This waveguide had the same DBE of 3 μm and were induced by an average power of 10 mW. The coupling efficiency can be assumed to be significantly higher, as this waveguide exhibited a similar intensity profile as shown in Figure 4.14a, and absorption can be neglected. To measure the exact coupling efficiency is a very complex task and was not performed during this thesis. Due to the unavailability of lasers with appropriate wavelength and the sensitivity region of the available CCD camera, the experimental options were limited. Once available, an optimal loss measurement setup with a laser wavelength of 2.4 μm should be implemented to obtain losses at the laser wavelength.

4.4.1   Active waveguides with ARM in Cr:ZnS

If one assumes a refractive index of Cr:ZnS equal to n = 2.27[32], by (11), the reflectance at an incident angle $\theta = 0$ can be calculated, yielding a value of 15 %. It becomes

evident that this has to be improved to achieve enhanced laser performance.   As
described in section 3, anti-reflection microstructures were fabricated on some of the
waveguides facets of the Cr: ZnS sample. Figure 4.20B) shows a microscopic image of
an ARM, which, if compared with Figure 4.20A), confirms that the ARM is directly
in front of the waveguide

The ARM morphology and periodicity were inspected by scanning electron microscopy.
Figure 4.24 shows an SEM image of an ARM, captured with a magnification of 25000x.
The characteristic periodic structure of the coating observed in the SEM image is
attributed to the single-pulse laser ablation process.
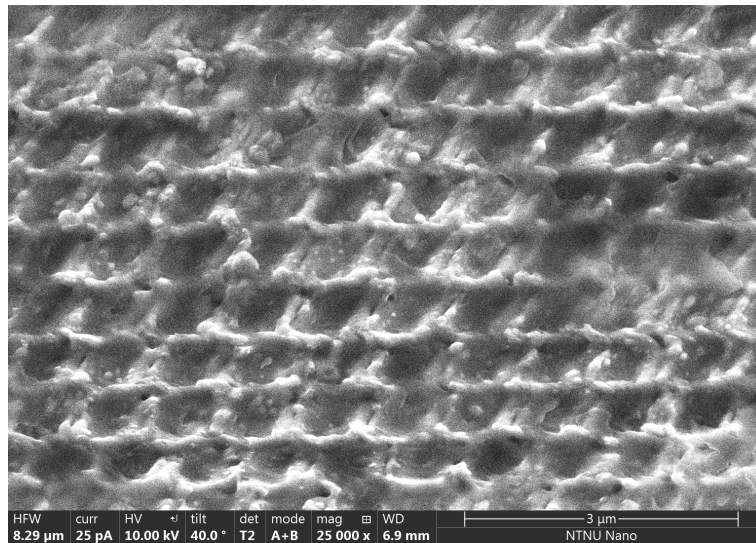
Figure 4.24: SEM image of the anti-reflection microstructure at 40°, with a magnification
of 25000x.

Since the setup used comprises an input and output coupler that is reflective in the
wavelength range between 2.1 and 2.5 µm, a diffraction wavelength λ_{diff} of 2.1 µm
is chosen. From eg. (16), and assuming a refractive index n = 2.277, the period can
be estimated. Although this value should be less than 0.93 µm, as shown in Figure
4.24, the periodicity seems to be below this value. This corresponds to the writing
parameters and confirms that the structure was fabricated with a period of 0.8 µm.

An image of the zone targeted for acquiring the Raman spectrum is shown in Figure
4.25. The measurement was performed at the central region in the figure, correspond-
ing approximately to the center of one of the ARMs.

The Raman spectrum in Figure 4.26 shows the same characteristic peaks with no
additional lines when comparing the processed ARM and the unprocessed reference
area of the Cr:ZnS. Only an enhanced intensity of the LO phonon line at 350 cm^{-1}
was significantly different[37]. Since the relative intensity of this line strongly depends
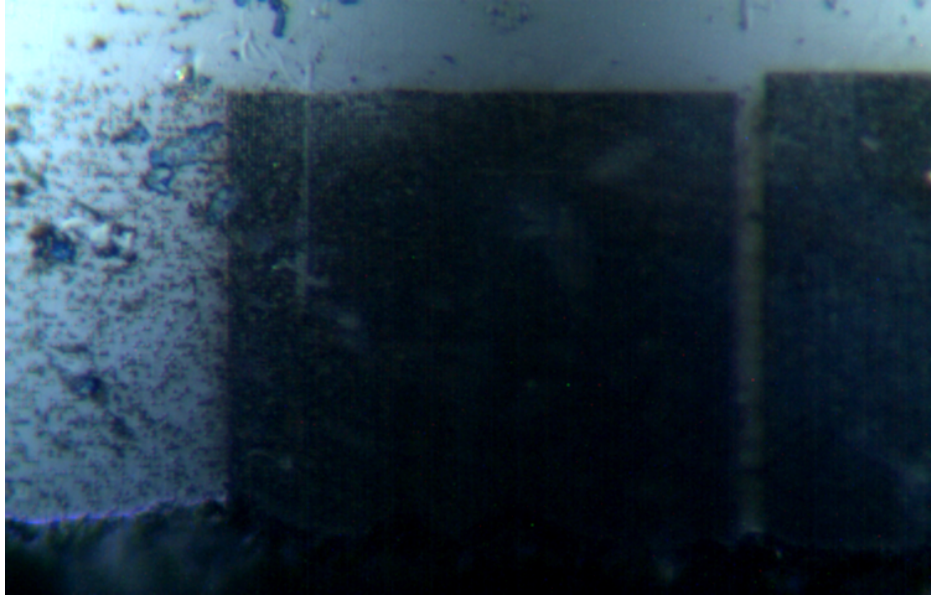
Figure 4.25: Optical microscopy image of targeted zone for the Raman spectrum measurement in Figure 4.26. The ARMs shown were made at a different part of the sample specifically for acquiring the Raman spectrum as well as SEM imaging without compromising the waveguides.
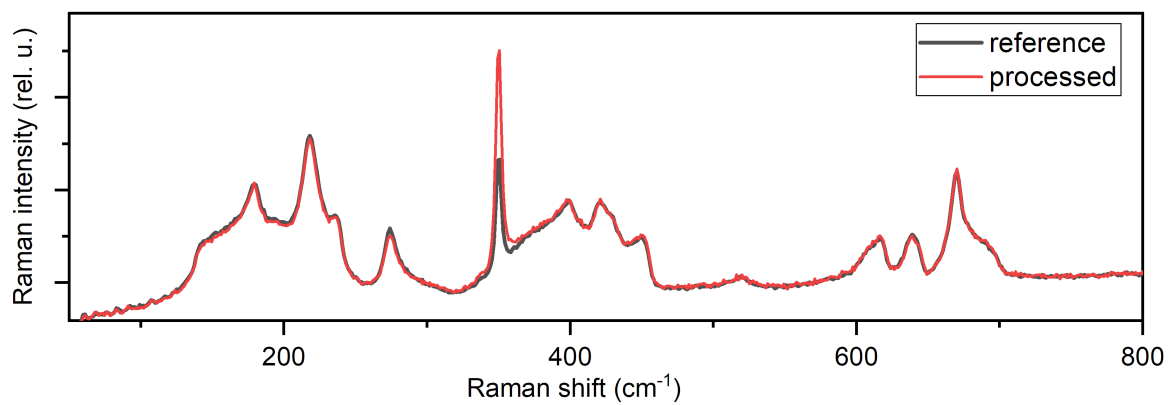
Figure 4.26: Micro-Raman spectrum of the processed ARM compared to unprocessed reference area.

69

on scattering geometry[66], this enhancement probably reflects the addition of more scattering orientations in the processed region, e.g. from the curved surfaces.
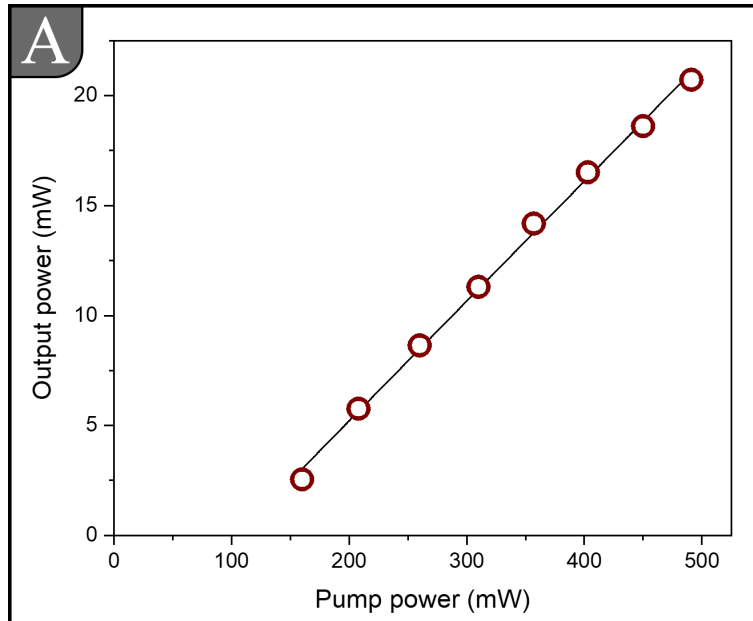
Figure 4.27: The output power of the waveguide laser with ARM structures[37].

The laser measurement yielded an average output power of 20 mW for 500 mW absorbed pump power and a threshold of approximately 136 mW. By using eq. The slope efficiency was estimated from eg. 5 to be about 5.5 %, with the corresponding curve shown in Figure 4.27. The ARM also yielded less transmittance than earlier demonstrated for similar materials[27], and half the slope efficiency obtained from the waveguide without the ARM on its facets[8]. This can be due to the shallow depth of the structures, as can be seen in Figure 4.24, and thus an insufficient aspect ratio. Another possible reason is the incurring of Fabry-Pérot effects since the coupling mirrors were mechanically attached to the waveguide end facets. Therefore, air gaps between the mirrors and the end facets may have existed, which could have affected the reflectance properties of the mirrors.

Finally, another cause could be the imperfect alignment of the ARMs with the waveguides on the output side of the sample, as shown in Figure 4.28. These imperfections could have contributed to scattering effects at the edge of the ARM that could have led to additional losses.
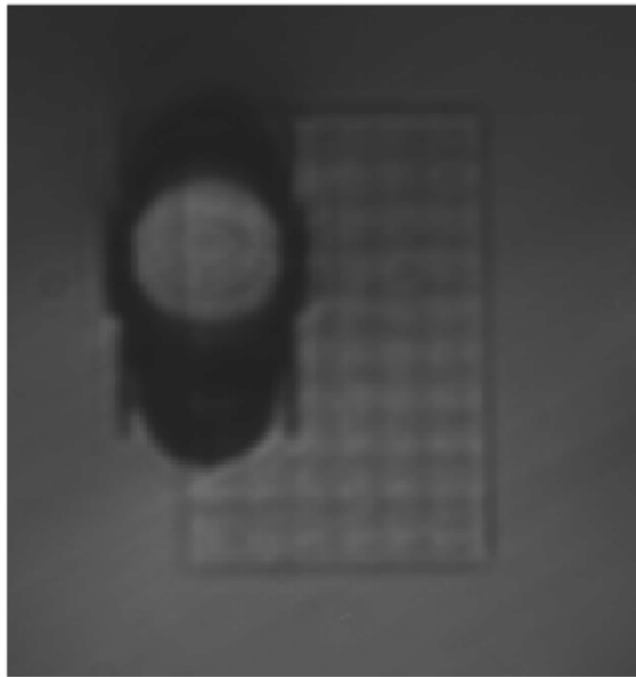
Figure 4.28: Microscopic image of the ARM on the output side of the Cr:ZnS sample.
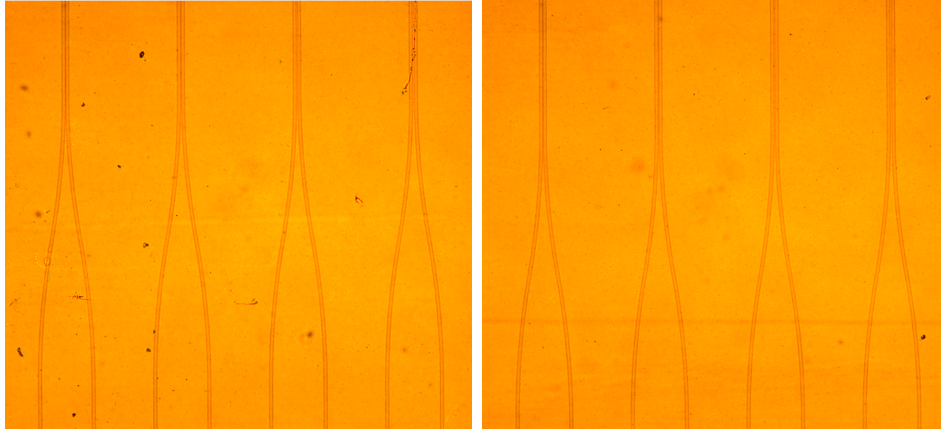
4.5   In-bulk couplers

As mentioned in section 3.1, there were a total of five undoped samples investigated during this thesis. The last two were an attempt to write in-bulk curved waveguides as well as couplers and are shown in Figures 4.29 and 4.30, respectively.

(a) Waveguides curved 25°.   (b) Waveguides curved 45°.
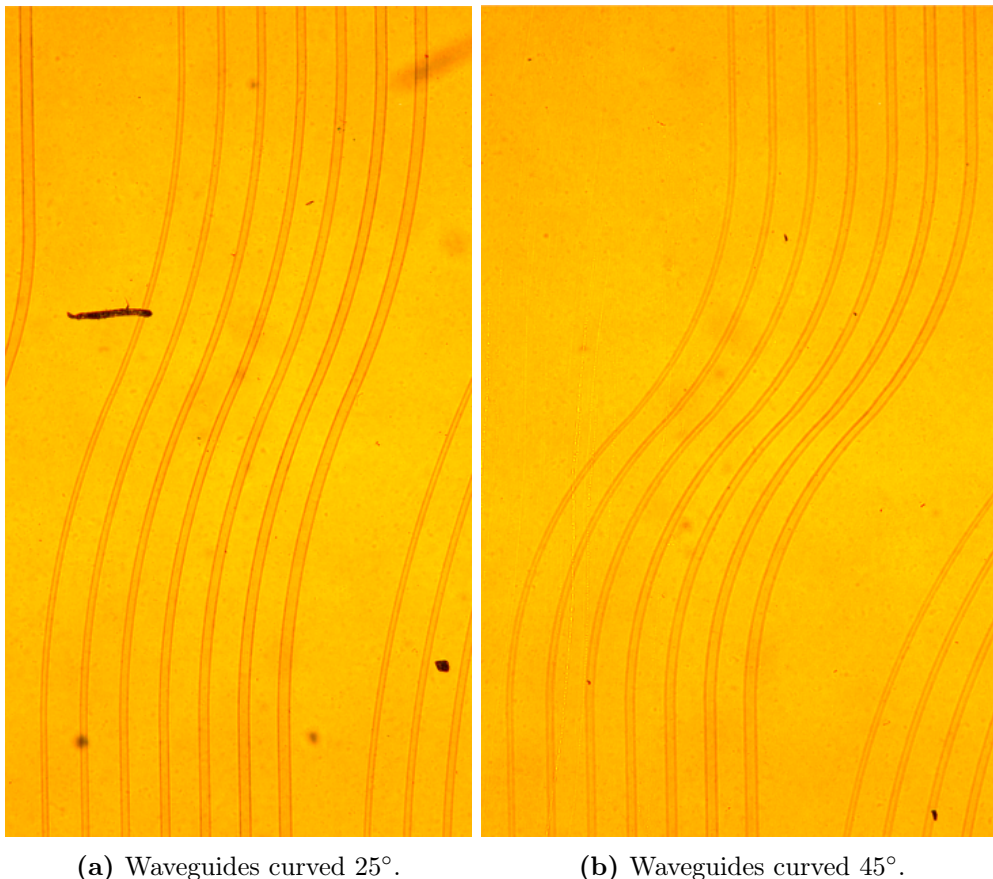
Figure 4.29: Sample 4 with waveguides curved 25° (a) and 45° (b), written with 20 kHz repetition rate and power 11 and 11.3 mW, respectively. Both set of waveguides contains the diameters 15, 17.5, 20, 22.5, 25, 27.5 and 30 µm.

The curved waveguides in sample 4 did not exhibit any guiding, at least not for the 1.55 µm light from the fiber laser used in the setup. As the DBE for all the curved waveguides was set to 4 µm and the writing power to 11 mW, these waveguides of 30 µm diameter should have a horizontal NA of around 0.035 if one considers the evolution presented in table 3. NA can initially be assumed independent of the core size, and, therefore, the curved waveguides of around 20 µm in diameter will exhibit a smaller $V number$, and thus, a mode radius approximately twice the size of the core radius. This might be the reason for the waveguides with smaller diameters not supporting waveguiding since the high mode radius introduces very high bending losses[56]. Since the couplers formed in sample 5 had this specific diameter, the same applies. The

reason for the curved waveguides with a diameter of 30 µm in sample 4 not supporting guiding is uncertain and may relate to the poor mechanical aligning of the incoming beam during the measurements. It can also be that even a mode radius a few microns larger than the core was sufficient for the bending losses to dominate in this case.

(a) In-bulk couplers 1-4.   (b) In-bulk couplers 23-26.

Figure 4.30: Sample 5 with couplers written at repetition rate 20 kHz and 11.1 mW average power, with a turn angle of 10°. The distance between each waveguide the couplers are made out of are set to 0, 2, 4 and 6 µm in both sets shown. (b) Shows a longer part where the waveguides are close together than (a), both with waveguides of diameter 20 µm.

5   Conclusion

5.1   Summary

During this thesis, laser-induced surface and subsurface structures have been investigated in ZnS and Cr: ZnS. Techniques such as optical microscopy, IR transmission microscopy, micro-Raman spectroscopy, and scanning electron microscopy have been implemented for their investigation.

To the best of my knowledge, the subsurface modifications investigated here are the first reported in-bulk structures in ZnS induced by a 2.1 µm ultrashort laser. The work also dealt with the investigation of subsurface single-line defects to determine optimal parameters for writing waveguides. Waveguides were subsequently inscribed into the bulk of ZnS crystalline samples, and their characteristics were studied. The work demonstrated the feasibility of developing highly symmetric waveguides using laser irradiation in this specific mid-IR spectral domain. Waveguides with nearly circular cores and claddings have been inscribed, an achievement reported only by An et al. [59]. However, in contrast to the waveguides by An et al. [59], which supported single-mode confinement only in the MIR region for wavelengths of 4 µm and had very high losses, the waveguides developed in this thesis demonstrated single-mode guiding at 1.55 µm.

Parameters such as numerical aperture, refractive index change, and parameter dependencies on size and shape were investigated. All waveguides inscribed with an average power of 10 mW or higher, at a 20 kHz repetition rate, and with a writing speed of 16 mm/s exhibited guiding of light. The waveguides with a diameter of 30 µm exhibited single-mode confinement and had a $V\,number$ in the optical fiber region, around ~ 2.0. They also had acceptable mode radii, which did not extend too far outside the waveguide core. The dependence of waveguide loss on laser power used for writing and the distance between each defect element was also established. During this thesis, the possibility of developing a compact gain medium, encompassing laser-written depressed-cladding waveguides with laser-manufactured anti-reflection coatings on their facets was demonstrated.

5.2   Future work

The next steps should include testing extreme values of different writing parameter. This could be useful to find out how much each parameter affects the final structure. Richter et al. [42] reported that the height of the structures were dependent on laser wavelength. It is difficult to confirm experimentally how much this applies, based on a few samples where the writing wavelength as well as several other parameters are different. To be able to determine which parameter has greater impact a study where only a few parameters are varying should be carried out.

Due to high absorption in Cr:ZnS at a wavelength of 1.55 µm, loss measurements in this region is sub-optimal. Similar measurements with the laser emitting wavelength of 2.4 µm should be carried out to achieve more precise values.

Curved waveguides and thus also couplers did not give any valid results during this thesis. Although with more research and characterization of the impact of specific writing parameters this might give exciting results in the future.

The Δn dependency on doping concentration, as was stated in Okhrimchuk and Duarte [51] in 2010, is yet to be demonstrated in ZnS. This could not be validated during this work due to several other different processing parameters in the doped and undoped sample. A similar study should be performed in ZnS, whereas process parameters stay the same. This could ultimately result larger $|\Delta n|$ and thus the possibility of smaller core diameter while still obtaining single-mode confinement. An increased $|\Delta n|$ might also result in working curved waveguides as the critical angle inside the core will decrease.

Further characterization of such structures investigated in this thesis, will give even better control over modification properties. This can provide higher repeatability of surface and subsurface structures and will enhance performances in photovoltaics and laser technology.

References

[1] E. Einmo. "Characterization of laser-induced microstructures in Cr:ZnS". unpublished. n.d.

[2] T. Maiman. "Stimulated Optical Radiation in Ruby". In: *Nature* 187.4736 (1960), pp. 493–494.

[3] D. Strickland and G. Mourou. "Compression of amplified chirped optical pulses". In: *Optics Communications* 55.6 (1985), pp. 447–449. ISSN: 0030-4018. DOI: https://doi.org/10.1016/0030-4018(85)90151-8. URL: https://www.sciencedirect.com/science/article/pii/0030401885901518.

[4] J. V. Rudd, G. Korn, S. Kane, J. Squier, G. Mourou, and P. Bado. "Chirped-pulse amplification of 55-fs pulses at a 1-kHz repetition rate in a Ti:Al2O3 regenerative amplifier". In: *Opt. Lett.* 18.23 (Dec. 1993), pp. 2044–2046. DOI: 10.1364/OL.18.002044. URL: http://opg.optica.org/ol/abstract.cfm?URI=ol-18-23-2044.

[5] J. H. Zhao, X. B. Li, Q. D. Chen, Z. G. Chen, and H. B Sun. "Ultrafast laser-induced black silicon, from micro-nanostructuring, infrared absorption mechanism, to high performance detecting devices". In: *Materials Today Nano* 11 (2020), p. 100078.

[6] K. C. Vishnubhatla, G. Nava, R. Osellame, and R. Ramponi. "Femtosecond Laser Micro-machining for Energy Applications". In: *Renewable Energy and the Environment.* Optica Publishing Group, 2013, EW2A.3. DOI: 10.1364/E2.2013.EW2A.3. URL: http://opg.optica.org/abstract.cfm?URI=E2-2013-EW2A.3.

[7] K. M. Davis, K. Miura, N. Sugimoto, and K. Hirao. "Writing waveguides in glass with a femtosecond laser". In: *Opt. Lett.* 21.21 (Nov. 1996), pp. 1729–1731.

[8] N. Tolstik, A. G. Okhrimchuk, M. P. Smayev, V. V. Likhov, E. Sorokin, and I. T. Sorokina. "Single-mode depressed cladding buried waveguide laser based on single-crystal Cr:ZnS". In: *Conference on Lasers and Electro-Optics.* Optical Society of America, 2019, STh1E.6.

[9] Orazio Svelto. *Principles of Lasers.* 5th Edition. Heidelberg: Springer Science+Business Media, 2010. ISBN: 978-1-4419-1301-2.

[10] L. D. DeLoach, R. H. Page, G. D. Wilke, S. A. Payne, and W. F. Krupke. "Transition metal-doped zinc chalcogenides: spectroscopy and laser demonstration of a new class of gain media". In: *IEEE Journal of Quantum Electronics* 32.6 (1996), pp. 885–895. DOI: 10.1109/3.502365.

[11] I. T. Sorokina, V. V. Dvoyrin, N. Tolstik, and E. Sorokin. "Mid-IR Ultrashort Pulsed Fiber-Based Lasers". In: *IEEE Journal of Selected Topics in Quantum Electronics* 20.5 (2014), pp. 99–110.

[12]   I. T. Sorokina and K. L. Vodopyanov. "Solid-State Mid-Infrared Laser Sources". In: *Topics in Applied Physics 89*. Eds. Berlin, Germany: Springer Verlag, 2003, p. 558.

[13]   Dr. Rüdiger Paschotta. *Titanium–sapphire Lasers*. URL: `https://www.rp-photonics.com/titanium_sapphire_lasers.html` (visited on 12/11/2021).

[14]   J. R. Macdonald, S. J. Beecher, P. A. Berry, G. Brown, K. L. Schepler, and A. K. Kar. "Efficient mid-infrared Cr:ZnSe channel waveguide laser operating at 2486 nm". In: *Opt. Lett.* 38.13 (July 2013), pp. 2194–2196.

[15]   I. T. Sorokina and E. Sorokin. "Femtosecond $Cr^{2+} - Based Lasers$". In: *IEEE Journal of Selected Topics in Quantum Electronics* 21.1 (2015), pp. 273–291.

[16]   Dr. Rüdiger Paschotta. *Slope Efficiency*. URL: `https://www.rp-photonics.com/slope_efficiency.html` (visited on 12/14/2021).

[17]   J. R. Macdonald, S. J. Beecher, A. Lancaster, P. A. Berry, K. L. Schepler, S. B. Mirov, and A. K. Kar. "Compact Cr:ZnS channel waveguide laser operating at 2333 nm". In: *Opt. Express* 22.6 (Mar. 2014), pp. 7052–7057.

[18]   Dr. Rüdiger Paschotta. *Fresnel reflections*. URL: `https://www.rp-photonics.com/fresnel_reflections.html` (visited on 12/15/2021).

[19]   Wikipedia contributors. *Anti-reflective coating — Wikipedia, The Free Encyclopedia*. 2021. URL: `https://en.wikipedia.org/w/index.php?title=Anti-reflective_coating&oldid=1056176424` (visited on 12/15/2021).

[20]   C. Grivas, D. P. Shepherd, T. C. May-Smith, R. W. Eason, M. Pollnau, A. Crunteanu, and M. Jelinek. "Performance of Ar-milled Ti: sapphire rib waveguides as single-mode broadband fluorescence sources". In: *IEEE Journal of Quantum Electron* 39.3 (2003).

[21]   X. Li, M. Li, H. Liu, and Y. Guo. "Fabrication of an Anti-Reflective Microstructure on ZnS by Femtosecond Laser Bessel Beams". In: *Molecules* 26.14 (2021).

[22]   J. R. Macdonald, S. J. Beecher, A. Lancaster, P. A. Berry, K. L. Schepler, and A. K. Kar. "Ultrabroad Mid-Infrared Tunable Cr:ZnSe Channel Waveguide Laser". In: *IEEE Journal of Selected Topics in Quantum Electronics* 21.1 (2015), pp. 375–379.

[23]   Y. Liao, Y. Cheng, C. Liu, J Song, F. He, Y. Shen, D. Chen, Z. Xu, Z. Fan, X. Wei, K. Sugioka, and K. Midorikawa. "Direct laser writing of sub-50 nm nanofluidic channels buried in glass for three-dimensional micro-nanofluidic integration". In: *Lab Chip* 13 (8 2013), pp. 1626–1631. DOI: `10.1039/C3LC41171K`. URL: `http://dx.doi.org/10.1039/C3LC41171K`.

[24]   B. C. Stuart, M. D. Feit, A. M. Rubenchik, B. W. Shore, and M. D. Perry. "Laser-Induced Damage in Dielectrics with Nanosecond to Subpicosecond Pulses". In: *Phys. Rev. Lett.* 74 (12 Mar. 1995), pp. 2248–2251. DOI: `10.1103/PhysRevLett.74.2248`. URL: `https://link.aps.org/doi/10.1103/PhysRevLett.74.2248`.

[25] S. Augst, D. Strickland, D. D. Meyerhofer, S. L. Chin, and J. H. Eberly. "Tunneling ionization of noble gases in a high-intensity laser field". In: *Phys. Rev. Lett.* 63 (20 Nov. 1989), pp. 2212–2215. DOI: 10.1103/PhysRevLett.63.2212. URL: https://link.aps.org/doi/10.1103/PhysRevLett.63.2212.

[26] R. L. Harzic, H. Schuck, D. Sauer, T. Anhut, I. Riemann, and K. König. "Sub-100 nm nanostructuring of silicon by ultrashort laser pulses". In: *Opt. Express* 13.17 (Aug. 2005), pp. 6651–6656. DOI: 10.1364/OPEX.13.006651. URL: http://opg.optica.org/oe/abstract.cfm?URI=oe-13-17-6651.

[27] A. A. Bushunov, M. K. Tarabrin, and V. A. Lazarev. "Review of Surface Modification Technologies for Mid-Infrared Antireflection Microstructures Fabrication". In: *Laser Photonics Review* 15.5 (Mar. 2019).

[28] B. Franta, E. Mazur, and S. K. Sundaram. "Ultrafast laser processing of silicon for photovoltaics". In: *International Materials Reviews* 63.4 (2018), pp. 227–240. DOI: 10.1080/09506608.2017.1389547. eprint: https://doi.org/10.1080/09506608.2017.1389547. URL: https://doi.org/10.1080/09506608.2017.1389547.

[29] A. A. Bushunov, M. K. Tarabrin, V. A. Lazarev, V. E. Karasik, Y. V. Korostelin, M. P. Frolov, Y. K. Skasyrsky, and V. I. Kozlovsky. "Fabrication of anti-reflective microstructures on chalcogenide crystals by femtosecond laser ablation". In: *Opt. Mater. Express* 9.4 (Apr. 2019), pp. 1689–1697.

[30] K. Sugioka and Y. Cheng. "Ultrafast lasers—reliable tools for advanced materials processing". In: *Light: Science & Applications* 3.4 (Apr. 2014), e149–e149. DOI: 10.1038/lsa.2014.30.

[31] Y. Bellouard, A. Champion, B. L. K. Lenssen, M. Matteucci, A. M. Schaap, M. Beresna, C. Corbari, M. Gecevicius, P. Kazansky, O. Chappuis, M. Kral, R. Clavel, F. Barrot, J. M. Breguet, Y. Mabillard, S. Bottinelli, M. Hopper, C. Hoenninger, E. Mottay, and J. Lopez. "The Femtoprint project". English. In: *Journal of Laser Micro Nanoengineering* 7.1 (2012), pp. 1–10. ISSN: 1880-0688. DOI: 10.2961/jlmn.2012.01.0001.

[32] Y. Peng, X. Zou, Z. Bai, Y. Leng, B. Jiang, X. Jiang, and L. Zhang. "Mid-infrared laser emission from Cr:ZnS channel waveguide fabricated by femtosecond laser helical writing". In: *Scientific Reports* 5.18365 (Dec. 2015).

[33] O. Tokel, A. Turnalı, G. Makey, P. Elahi, T. Çolakoğlu, E. Ergeçen, Ö. Yavuz, R. Hübner, M. Z. Borra, I. Pavlov, et al. "In-chip microstructures and photonic devices fabricated by nonlinear laser lithography deep inside silicon". In: *Nature photonics* 11.10 (2017), pp. 639–645.

[34] M. P. Smayev, V. V. Dorofeev, A. N. Moiseev, and A. G. Okhrimchuk. "Femtosecond laser writing of a depressed cladding single mode channel waveguide in high-purity tellurite glass". In: *Journal of Non-Crystalline Solids* 480 (2018). ISNOG 2016 Proceeding of the 20th International Symposium on Non-Oxide and New Optical Glasses, Nizhny Novgorod, Russia, August 21-26, 2016, pp. 100–106.

[35] W. Watanabe, T. Asano, K. Yamada, K. Itoh, and J. Nishii. "Wavelength division with three-dimensional couplers fabricated by filamentation of femtosecond laser pulses". In: *Opt. Lett.* 28.24 (Dec. 2003), pp. 2491–2493. DOI: `10.1364/OL.28.002491`. URL: `http://opg.optica.org/ol/abstract.cfm?URI=ol-28-24-2491`.

[36] A. Okhrimchuk, V. Mezentsev, A. Shestakov, and I. Bennion. "Low loss depressed cladding waveguide inscribed in YAG:Nd single crystal by femtosecond laser pulses". In: *Opt. Express* 20.4 (Feb. 2012), pp. 3832–3843.

[37] E. Sorokin, A. A. Bushunov, N. Tolstik, A. A. Teslenko, E. Einmo, M. K. Tarabrin, V. A. Lazarev, and I. T. Sorokina. "All-laser-microprocessed waveguide Cr: ZnS laser". In: *Optical Materials Express* 12.2 (2022), pp. 414–420.

[38] Dr. Rüdiger Paschotta. *Chirped-pulse Amplification.* URL: `https://www.rp-photonics.com/chirped_pulse_amplification.html`.

[39] C. Momma, B. N. Chichkov, S. Nolte, F. von Alvensleben, A. Tünnermann, H. Welling, and B. Wellegehausen. "Short-pulse laser ablation of solid targets". In: *Optics Communications* 129.1 (1996), pp. 134–142. ISSN: 0030-4018. DOI: `https://doi.org/10.1016/0030-4018(96)00250-7`. URL: `https://www.sciencedirect.com/science/article/pii/0030401896002507`.

[40] K. C. Phillips, H. H. Gandhi, E. Mazur, and S. K. Sundaram. "Ultrafast laser processing of materials: a review". In: *Adv. Opt. Photon.* 7.4 (Dec. 2015), pp. 684–712. DOI: `10.1364/AOP.7.000684`. URL: `http://opg.optica.org/aop/abstract.cfm?URI=aop-7-4-684`.

[41] D. M. Simanovskii, H. A. Schwettman, H. Lee, and A. J. Welch. "Midinfrared Optical Breakdown in Transparent Dielectrics". In: *Phys. Rev. Lett.* 91 (10 Sept. 2003), p. 107601. DOI: `10.1103/PhysRevLett.91.107601`. URL: `https://link.aps.org/doi/10.1103/PhysRevLett.91.107601`.

[42] R. A. Richter, N. Tolstik, S. Rigaud, P. D. Valle, A. Erbe, P. Ebbinghaus, I. Astrauskas, V. Kalashnikov, E. Sorokin, and I. T. Sorokina. "Sub-surface modifications in silicon with ultra-short pulsed lasers above 2µm". In: *J. Opt. Soc. Am. B* 37.9 (Sept. 2020), pp. 2543–2556. DOI: `10.1364/JOSAB.396074`. URL: `http://opg.optica.org/josab/abstract.cfm?URI=josab-37-9-2543`.

[43] W. Kaiser and C. G. B. Garrett. "Two-Photon Excitation in CaF_2: Eu^{2+}". In: *Phys. Rev. Lett.* 7 (6 Sept. 1961), pp. 229–231. DOI: `10.1103/PhysRevLett.7.229`. URL: `https://link.aps.org/doi/10.1103/PhysRevLett.7.229`.

[44] M. H. Niemz. "Threshold dependence of laser-induced optical breakdown on pulse duration". In: *Applied physics letters* 66.10 (1995), pp. 1181–1183.

[45] Guang S. He, Loon-Seng Tan, Qingdong Zheng, and Paras N. Prasad. "Multi-photon Absorbing Materials: Molecular Designs, Characterizations, and Applications". In: *Chemical Reviews* 108.4 (2008). PMID: 18361528, pp. 1245–1330. DOI: 10.1021/cr050054x. eprint: https://doi.org/10.1021/cr050054x. URL: https://doi.org/10.1021/cr050054x.

[46] L. V. Keldysh. "Ionization in the field of a strong electromagnetic wave". In: *Sov. Phys. JETP* 20.5 (1965), pp. 1307–1314.

[47] M. Lenzner, J. Krüger, S. Sartania, Z. Cheng, C. Spielmann, G. Mourou, W. Kautek, and F. Krausz. "Femtosecond optical breakdown in dielectrics". In: *Physical review letters* 80.18 (1998), p. 4076.

[48] Dr. Rüdiger Paschotta. *Kerr Effect*. URL: https://www.rp-photonics.com/kerr_effect.html.

[49] G. W. Pearson, C. Radzewicz, and J. S. Krasinski. "Use of ZnS as a self-focusing element in a self-starting Kerr lens modelocked Ti: sapphire laser". In: *Generation, Amplification, and Measurement of Ultrashort Laser Pulses*. Vol. 2116. SPIE. 1994, pp. 76–87.

[50] N. Sudani. "Thin wafer dicing using a high repetition rate femtosecond laser". In: *Ryerson University, Masters Thesis* (2009), pp. 1–123.

[51] A. Okhrimchuk and F. J. Duarte. *Femtosecond fabrication of waveguides in ion-doped laser crystals*. INTECH Open Access Publisher, 2010.

[52] M. Will, S. Nolte, B. N. Chichkov, and A. Tünnermann. "Optical properties of waveguides fabricated in fused silica by femtosecond laser pulses". In: *Applied Optics* 41.21 (2002), pp. 4360–4364.

[53] L. Gui, B. Xu, and T. C. Chong. "Microstructure in lithium niobate by use of focused femtosecond laser pulses". In: *IEEE Photonics Technology Letters* 16.5 (2004), pp. 1337–1339.

[54] D. Wortmann, M. Ramme, and J. Gottmann. "Refractive index modification using fs-laser double pulses". In: *Optics Express* 15.16 (2007), pp. 10149–10153.

[55] V. R. Bhardwaj, E. Simova, P. B. Corkum, D. M. Rayner, C. Hnatovsky, R. S. Taylor, B. Schreder, M. Kluge, and J. Zimmer. "Femtosecond laser-induced refractive index modification in multicomponent glasses". In: *Journal of applied physics* 97.8 (2005), p. 083102.

[56] A. M. Streltsov. "Femtosecond-laser writing of tracks with depressed refractive index in crystals". In: *Laser Micromachining for Optoelectronic Device Fabrication*. Vol. 4941. SPIE. 2003, pp. 51–57.

[57]   R. R. Gattass and E. Mazur. "Femtosecond laser micromachining in transparent materials". In: *Nature photonics* 2.4 (2008), pp. 219–225.

[58]   d. Marcuse. "Loss analysis of single-mode fiber splices". In: *Bell system technical journal* 56.5 (1977), pp. 703–718.

[59]   Q. An, Y. Ren, Y. Jia, J. R. V. Aldana, and F. Chen. "Mid-infrared waveguides in zinc sulfide crystal". In: *Opt. Mater. Express* 3.4 (Apr. 2013), pp. 466–471. DOI: 10.1364/OME.3.000466. URL: http://opg.optica.org/ome/abstract.cfm?URI=ome-3-4-466.

[60]   I. T. Sorokina, A. Okhrimchuk, M. Smayev, V. Likhov, E. Sorokin, and N. Tolstik. "Femtosecond laser writing of the depressed cladding buried channel waveguides in ZnS crystal". In: *Mid-Infrared Coherent Sources*. Optica Publishing Group. 2018, pp. MM3C–7.

[61]   Dr. Rüdiger Paschotta. *Waveguide Lasers*. URL: https://www.rp-photonics.com/waveguide_lasers.html.

[62]   S. Brülisauer, D. Fluck, C. Solcia, T. Pliska, and P. Günter. "Nondestructive waveguide loss-measurement method using self-pumped phase conjugation for optimum end-fire coupling". In: *Optics letters* 20.17 (1995), pp. 1773–1775.

[63]   Dr. Rüdiger Paschotta. *Fiber Joints*. URL: https://www.rp-photonics.com/fiber_joints.html.

[64]   H. H. Li. "Refractive index of ZnS, ZnSe, and ZnTe and its wavelength and temperature derivatives". In: *Journal of physical and chemical reference data* 13.1 (1984), pp. 103–150.

[65]   Dr. Rüdiger Paschotta. *V Number*. URL: https://www.rp-photonics.com/v_number.html.

[66]   W. G. Nilsen. "Raman Spectrum of Cubic ZnS". In: *Phys. Rev.* 182 (June 1969), pp. 838–850.
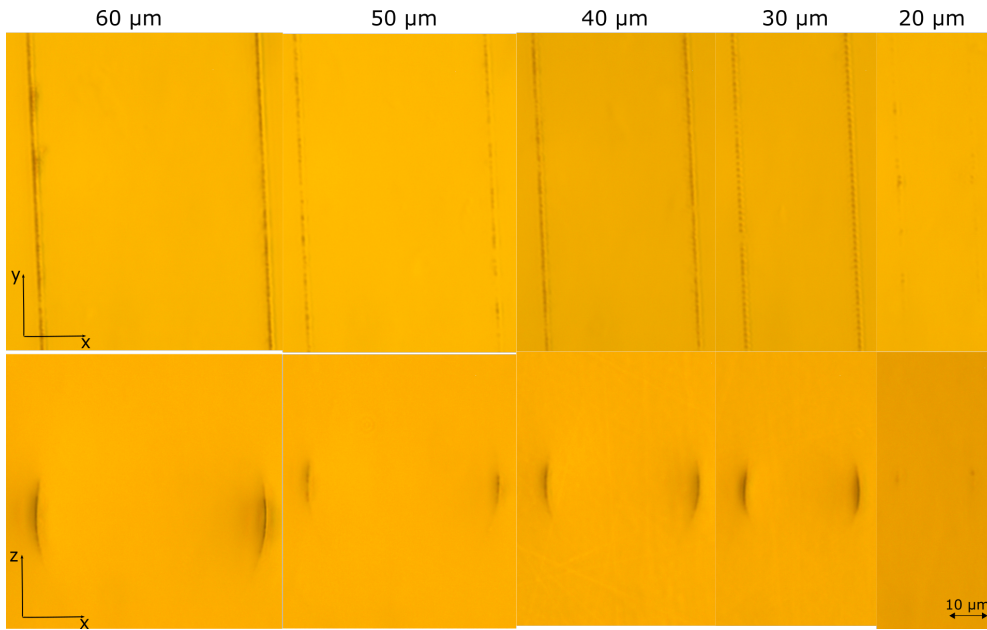
# A   Waveguides - supplementary images

All the detectable waveguides with their respective writing parameters are represented in the figures below.
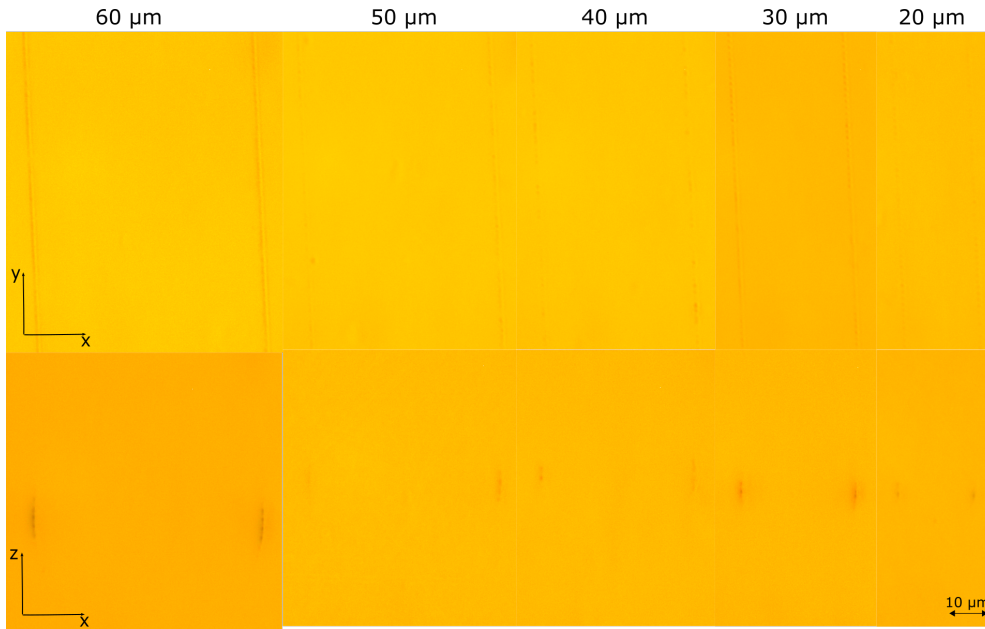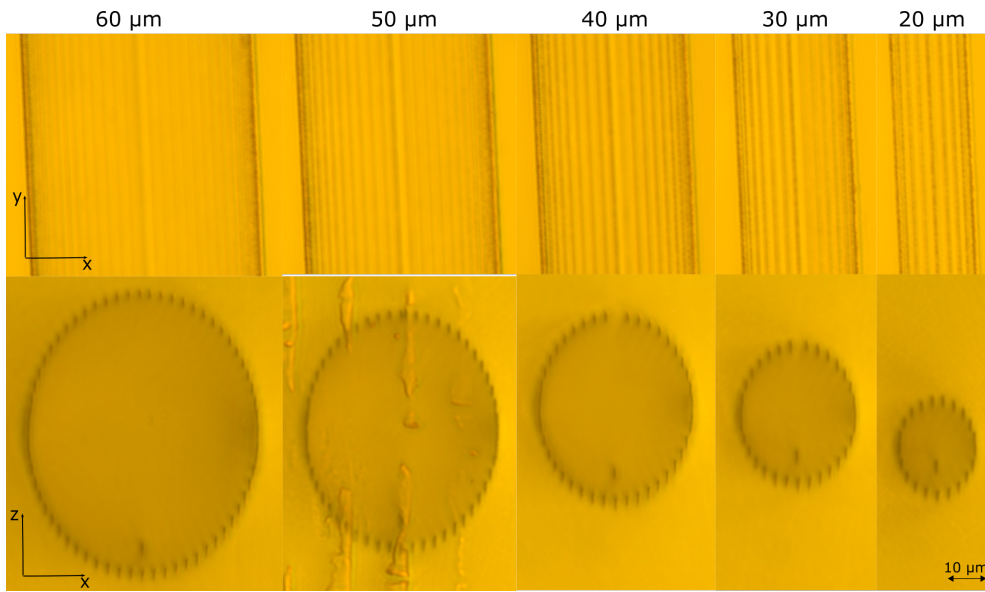

Figure A.1: Waveguides of diameter 60, 50, 40, 30 and 20 µm, written with 7 mW average power(below initial threshold) with DBE of 2 µm. Image from the top and cross-section.
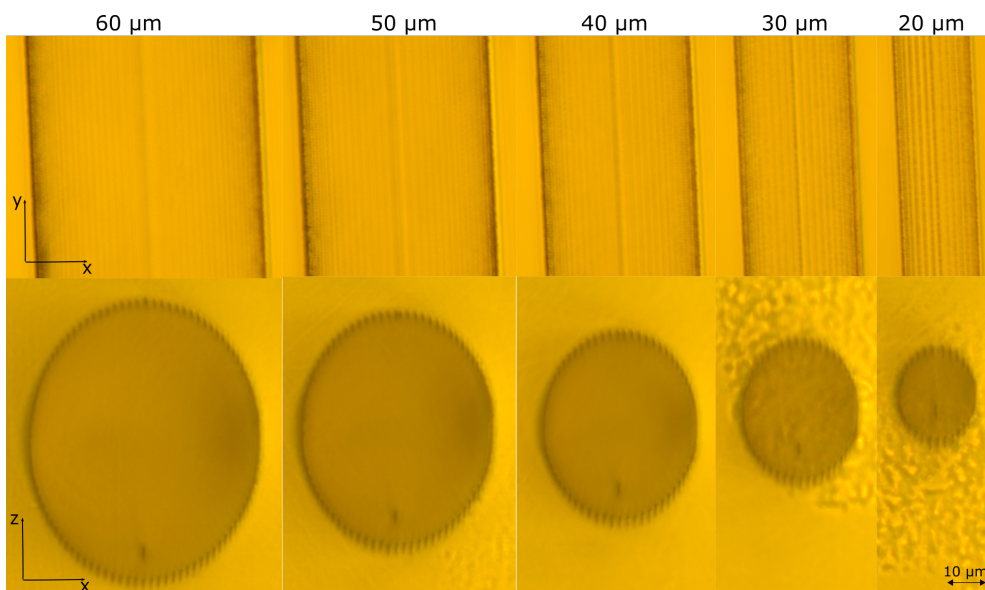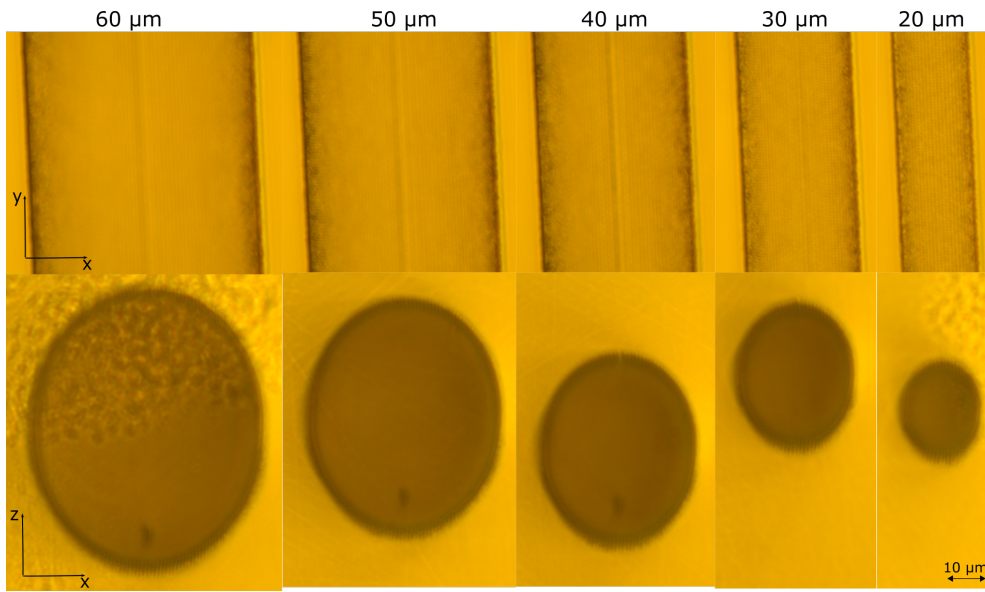
Figure A.2: Waveguides of diameter 60, 50, 40, 30 and 20 µm, written with 7 mW average power(below initial threshold) and DBE of 1 µm. Image from the top and cross-section.
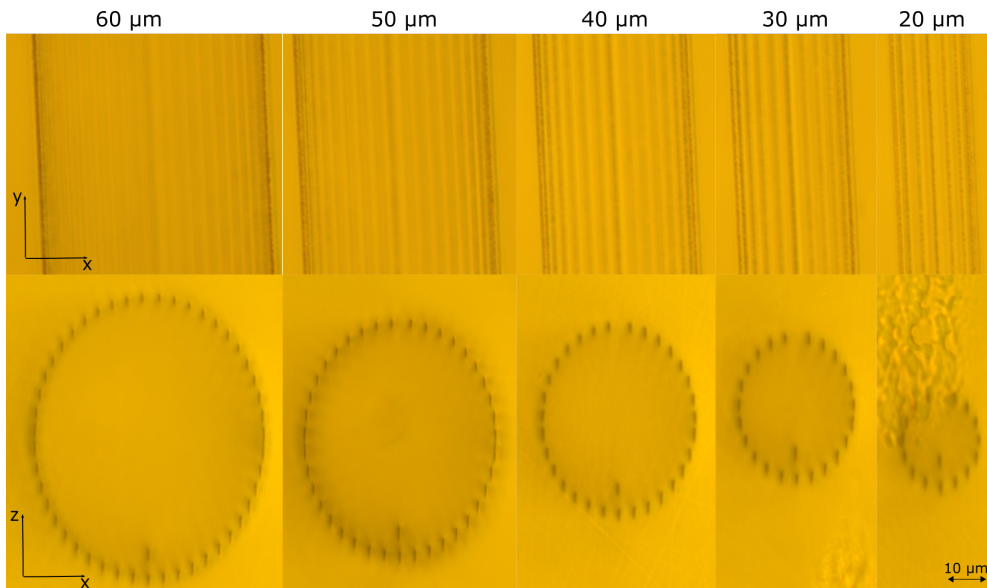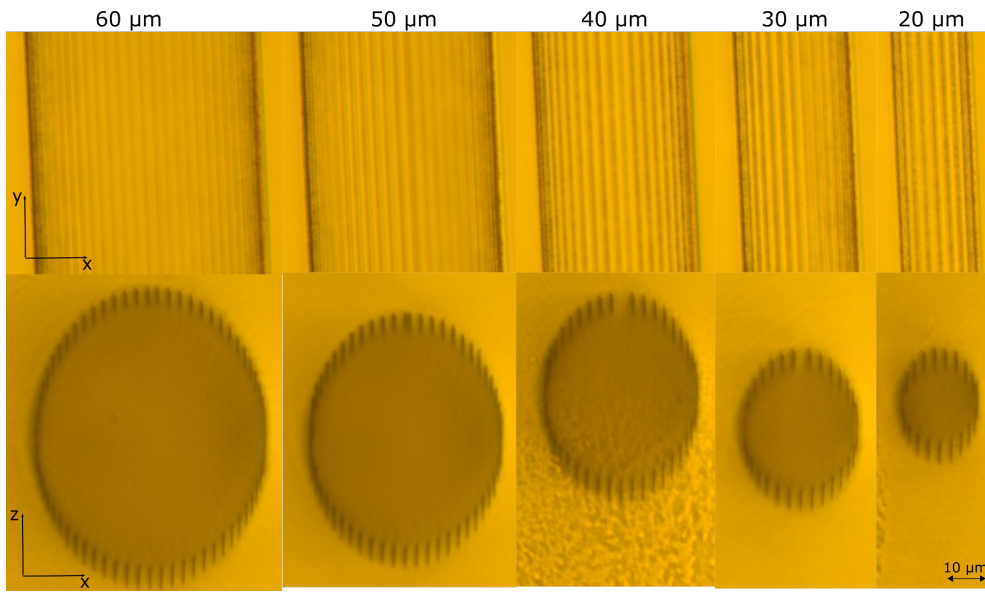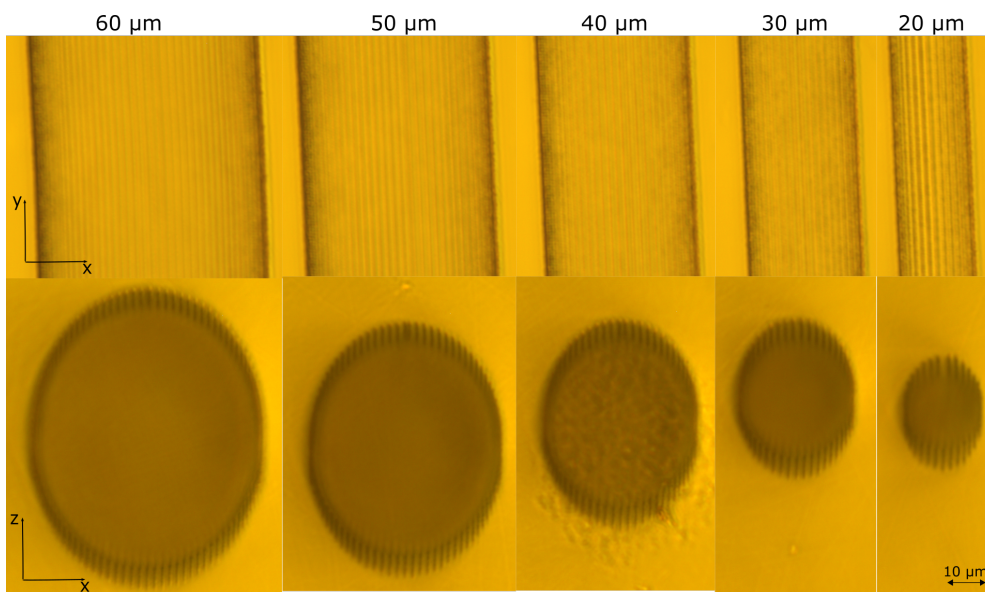

Figure A.3: Waveguides of diameter 60, 50, 40, 30 and 20 µm, written with 10 mW average power with DBE of 4 µm. Image from the top and cross-section.
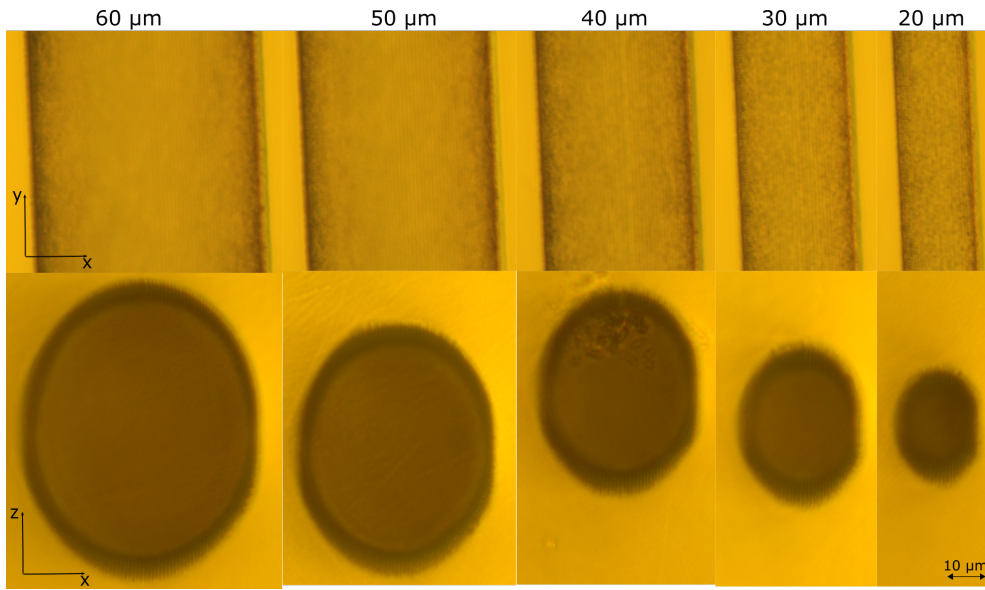
Figure A.4: Waveguides of diameter 60, 50, 40, 30 and 20 µm, written with 10 mW average power with DBE of 3 µm. Image from the top and cross-section.

Figure A.5: Waveguides of diameter 60, 50, 40, 30 and 20 µm, written with 10 mW average power with DBE of 2 µm. Image from the top and cross-section.

87

Figure A.6: Waveguides of diameter 60, 50, 40, 30 and 20 µm, written with 10 mW average power with DBE of 1 µm. Image from the top and cross-section.
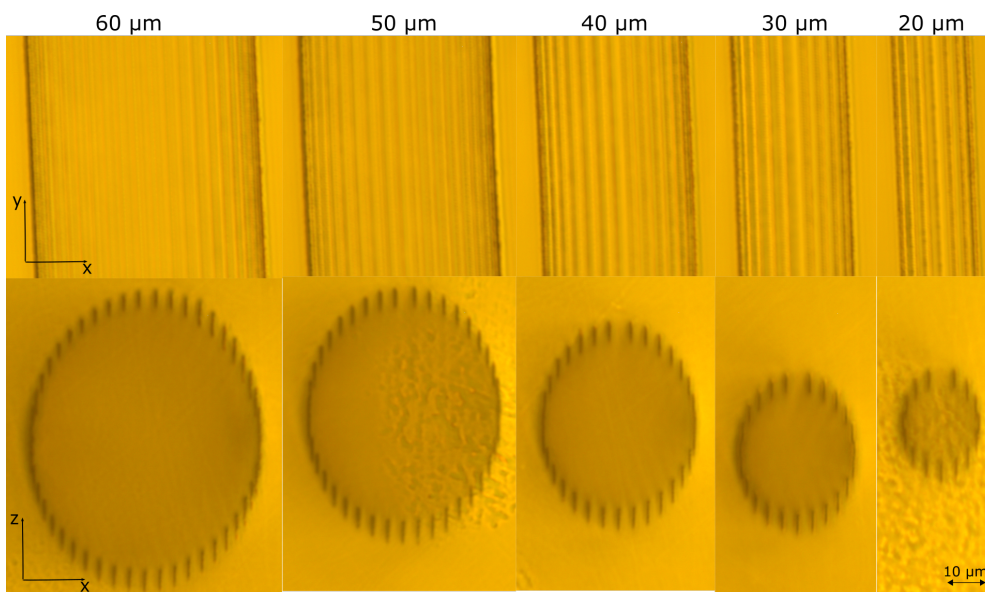
Figure A.7: Waveguides of diameter 60, 50, 40, 30 and 20 µm, written with 15 mW average power with DBE of 4 µm. Image from the top and cross-section.
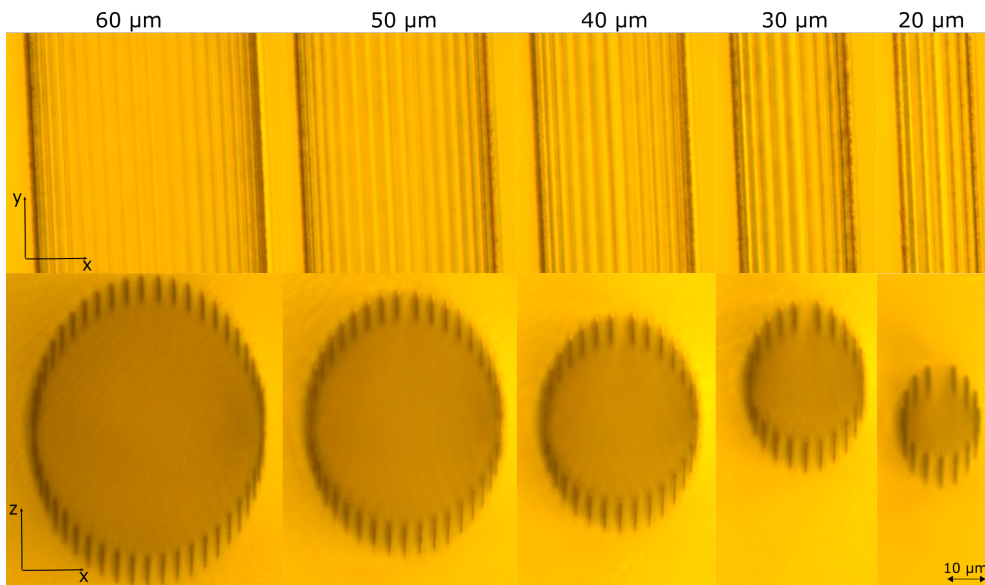
Figure A.8: Waveguides of diameter 60, 50, 40, 30 and 20 µm, written with 15 mW average power with DBE of 3 µm. Image from the top and cross-section.
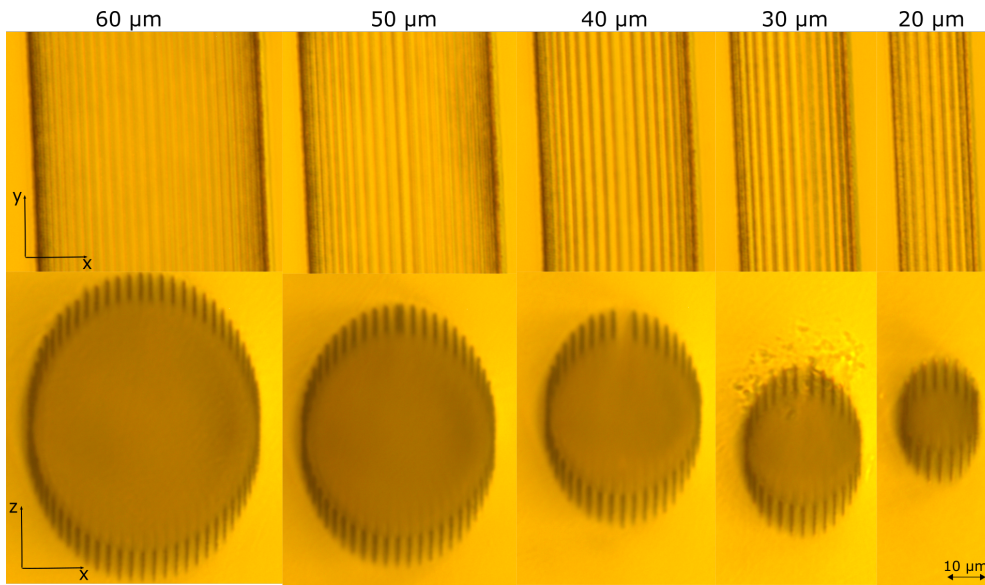

Figure A.9: Waveguides of diameter 60, 50, 40, 30 and 20 µm, written with 15 mW average power with DBE of 2 µm. Image from the top and cross-section.
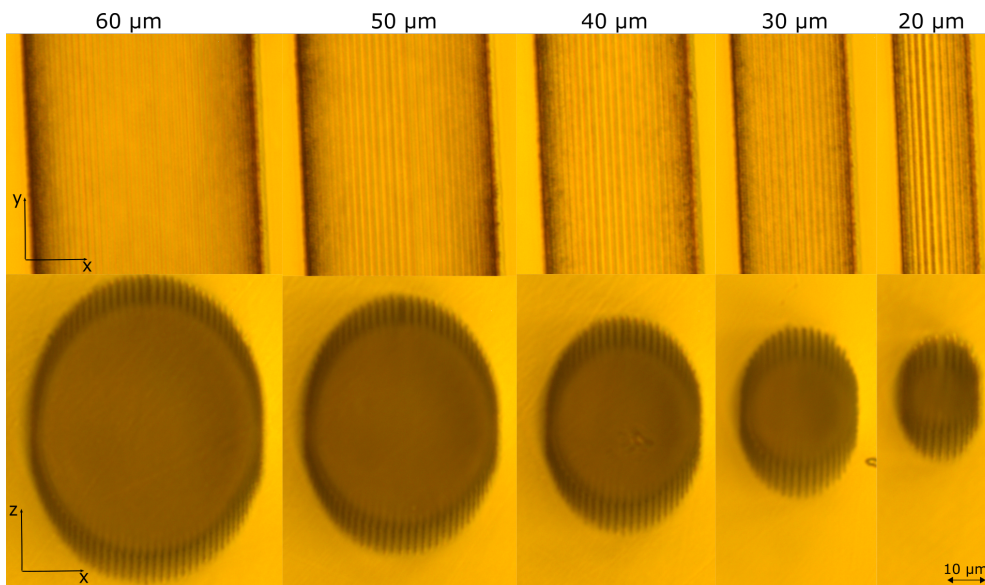
89

Figure A.10: Waveguides of diameter 60, 50, 40, 30 and 20 µm, written with 15 mW average power with DBE of 1 µm. Image from the top and cross-section.
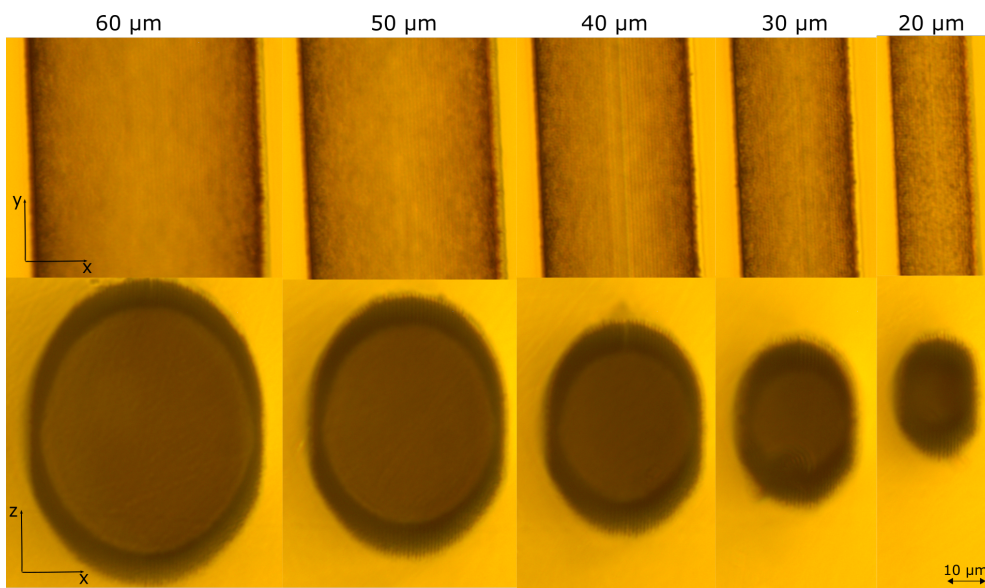

Figure A.11: Waveguides of diameter 60, 50, 40, 30 and 20 µm, written with 20 mW average power with DBE of 4 µm. Image from the top and cross-section.

Figure A.12: Waveguides of diameter 60, 50, 40, 30 and 20 µm, written with 20 mW average power with DBE of 3 µm. Image from the top and cross-section.

Figure A.13: Waveguides of diameter 60, 50, 40, 30 and 20 µm, written with 20 mW average power with DBE of 2 µm. Image from the top and cross-section.

Figure A.14: Waveguides of diameter 60, 50, 40, 30 and 20 µm, written with 20 mW average power with DBE of 1 µm. Image from the top and cross-section.

Eskil J. N. Einmo

Characterization of Laser-Induced Surface and Subsurface Modifications in ZnS

NTNU

Norwegian University of
Science and Technology